A Raman Laser System for Adiabatic Transfer of Polar Molecules

Diana Amaro

Department of Physics

University of Coimbra

A thesis submitted for the degree of

Master of Science

Coimbra, September 2013

UNIVERSIDADE DE COIMBRA

Abstract

This thesis reports on a Raman optical setup designed to implement a scheme, called stimulated Raman adiabatic passage, into an experiment with which ultracold NaK polar molecules in the rovibrational ground state are intended to be created and studied. The laser wavelengths used to perform this Raman transfer from the Feshbach to the ground state are 652.654nm and 486.995nm. For the Raman process to be efficient, high frequency stability is required. In order to achieve it, two external cavity diode lasers, one per wavelength, are independently locked to a reference cavity using the Pound-Drever-Hall technique. The cavity's spacer is made of an ultra-low expansion glass, which, if the cavity is kept at the zero-crossing temperature 9.4 ± 0.5°C, minimizes changes in the resonant mode frequencies when a variation of the external temperature occurs. Furthermore, this cavity is placed inside a temperature stabilized vacuum housing and has a spherical geometry, which makes its length insensitive to vibrations. The cavity was found to have a finesse of 189950 for $\lambda = 652$nm and 33740 for $\lambda = 487$nm. The $\lambda = 487$nm laser, when locked, has a line width of approximately 500Hz. Regarding the frequency stability, oscillations with an amplitude of 1kHz and a period of 1000s were observed on top of a drift of few Hz/s, which is still within the transfer requirements. To be able to tune the frequencies of the light in order to achieve the desired detunings, two other lasers were built running at the same two wavelengths. While part of the light of these lasers will be sent through optical fibers to the experiment, each laser beam with the remaining light is overlapped with the correspondent frequency stabilized laser beam. The resultant beat signals are used to lock them with a frequency offset up to 6GHz, which corresponds to two free-spectral ranges of the cavity. That offset can be defined through a computer, enabling high control over the frequencies that are used in the Raman scheme.

Contents

List of Figures **iii**

1 Introduction **1**
1.1 Outline 6

2 Theoretical Background **7**
2.1 Molecular physics 7
2.1.1 Born-Oppenheimer approximation 8
2.1.2 Rotation and Vibration 9
2.1.3 Hund's cases 11
2.1.4 Selection rules 14
2.1.5 Franck-Condon Principle 15
2.2 Feshbach molecules 17
2.3 Stimulated Raman adiabatic passage 19
2.3.1 Three-level hamiltonian 21
2.3.2 Adiabacity conditions 22
2.3.3 Pulse Delay 23
2.3.4 One and two-photon detuning line width 24
2.3.5 Effect of a decaying intermediate state 25
2.3.6 Effect of several intermediate levels on the transfer efficiency 26
2.3.7 Effect of noise on the transfer efficiency 29
2.3.8 States for realization of STIRAP 31
2.3.9 Adiabacity conditions in our setup 33

3 Laser System **35**
3.1 External cavity diode lasers 36
3.2 Reference cavity and vacuum chamber 38
3.3 Feedback systems 43
3.4 Pound-Drever-Hall frequency lock 45

3.5 Optical Setup 51

4 Experimental Results **59**
4.1 Characterization of the lasers 59
4.2 Electronic circuits of the Pound-Drever-Hall lock 62
4.3 Finesse of the cavity 66
4.4 Laser line width 69
4.5 Stabilization of the cavity 70
4.6 Noise 75

5 Conclusion and outlook **77**

Bibliography **79**

Electro-optic modulator **87**

List of Figures

1.1 Dipolar interaction between molecules 2
1.2 Range of density and temperatures achieved by molecules produced by several methods 4
1.3 Overall scheme of the experiment 5

2.1 Diatomic molecule 7
2.2 Born-Oppenheimer potential 9
2.3 Symmetric top 11
2.4 Hund's case a 12
2.5 Hund's case c 13
2.6 Franck-Condon principle 16
2.7 Scheme of a Feshbach resonance 18
2.8 Scattering length and energy as a function of magnetic field near a Feshbach resonance 19
2.9 STIRAP scheme 20
2.10 Three-level system scheme 21
2.11 Transfer efficiency for one and two-photon detuning 25
2.12 STIRAP with multiple intermediate states 27
2.13 Transfer efficiency as a function of one photon detuning for the STIRAP scheme with two intermediate levels 28
2.14 Transfer efficiency as a function of one photon detuning for the STIRAP scheme with five intermediate levels 29
2.15 Transfer efficiency as a function of the pulse area for two different phase diffusion coefficients 30
2.16 NaK molecular potentials 31
2.17 Square of the transition dipole moment of the $Na^{40}K$ molecule . . 32

3.1 Simplified scheme of the setup 36
3.2 Littrow configuration for an external cavity diode laser 37

3.3 Transmittance as a function of the wavelength 39
3.4 Scheme of the half-symmetric resonator 40
3.5 Frequency of the transverse electromagnetic modes (TEM) within the free-spectral range around TEM_{00} 42
3.6 Vacuum chamber, thermal shield and cavity photographs 43
3.7 Scheme of a feedback loop with open-loop gain $G(\omega)$ 44
3.8 Reflection intensity and phase at a resonance of the optical resonator 46
3.9 Scheme of the Pound-Drever-Hall lock 47
3.10 Error signal as a function of laser frequency 48
3.11 Transfer function of the PDH lock 50
3.12 Photograph of an external cavity diode laser 52
3.13 Overview of the Pound-Drever-Hall lock 54
3.14 Transmission as a function of time when the PZT voltage is swept. 56
3.15 Overview of the beat between *master* and *slave* lasers setup 57
3.16 Electronic setup used to lock and control the slave laser 58

4.1 Output power of the lasers as a function of the current's intensity. 59
4.2 Output power of the red laser as a function of the wavelength. . . 60
4.3 DC modulation and protection circuit used for the ECDLasers. . . 60
4.4 Transfer function of the ECDLasers 62
4.5 Lock box circuit 63
4.6 PZT box circuit 64
4.7 Transfer function of the lock boxes 65
4.8 Slope of the error signal 65
4.9 Gain of the feedback loop 66
4.10 Cavity ring-down measurement 67
4.11 Line shape of the blue laser 69
4.12 Thermalization time of the cavity 70
4.13 Determination of the zero-crossing temperature 71
4.14 Frequency of the beat signal recorded during four days 71
4.15 Drift rate of the laser frequency as a function of temperature . . . 72
4.16 Recordings of the beat signal frequency, temperature and humidity for an incident power of $50\mu W$ 73
4.17 Beat signal frequency as function of room temperature 74
4.18 Power spectrum of the laser calculated through the noise in the error signal 76

1 Scheme of an EOM similar to the ones used in the experiment . . . 88

1 Introduction

The desire of the mankind to "see through matter" and to be able to understand all intriguing phenomena is not recent. In solid state physics the study of matter is hampered by numerous parameters that are not tunable and others that interrupt the periodic order of the system like surface effects and lattice defects. In high energy physics the study of the constituents of matter and their interactions is done "*post-mortem*", which comprehends the destruction of the particles. Without quantum optics, we would lack the possibility to observe "*in-vivo*" the particles while tuning their interactions.

After the first proposal in the 1970s on using radiation pressure of a laser beam to slow sodium atoms down [1], the development of laser cooling and trapping in 1980s (for an overview see [2]) allowed not only to observe the particles but also to trap them for long periods of time and control both the internal degrees of freedom (electronic, fine and hyperfine states) and the external ones (motion of the atoms in the lab). In 1995 [3, 4], by using dilute atomic vapors it was possible to realize experimentally a theory proposed by Einstein [5] based in Bose's previous paper [6], a Bose-Einstein condensate was for the first time observed. This phenomenon corresponds to a macroscopic occupation of the ground state when the phase-space density is larger than a certain value, which demands both low temperatures and high particle densities. This experimental realization was a turning point in quantum optics, since several quantum many-body effects were observed and accomplished afterwards: interference between two overlapping Bose condensates [7], atom laser [8], quantum degenerate gas of fermions [9], long-range phase coherence [10], superfluidity in BEC [11], BEC of molecules formed by fermonic atoms [12, 13, 14], BEC-BCS crossover by tuning the scattering length near a Feshbach resonance [15], Fermi superfluidity [16], among others.

Another breakthrough in the study of ultracold atoms was the application of optical lattices. These can be understood as crystalline structures, formed by retro-reflected laser beams, similar to solid state systems which are addition-

ally highly controllable, with diminished lattice defects and without unwanted relaxation mechanisms like phonons. The atoms in the optical lattice can be regarded as electrons in the solids. However, the former ones have the advantage of the possibility to change their interaction by tuning the scattering length in the vicinity of a so-called Feshbach resonance. In 1963, Hubbard proposed a theory [17] to explain the dynamics of electrons in a periodic potential, which was later adapted to bosons [18]. Following a theoretical proposal based on the bose-hubbard hamiltonian [19], it was possible to observe the superfluid to Mott-insulator transition [20], by loading ultracold atomic bosons into an optical lattice and by controlling the depth of the lattice. The frequency standards' field has also benefited from the development of optical lattices with the realization of atomic clocks [21].

In contrast to atoms, with which all the work previously mentioned was done, cold molecules have additional degrees of freedom, such as rotation and vibration. This makes them richer and more complex systems to be studied since new intriguing problems can be addressed such as new quantum phases. Moreover, in the case of heteronuclear polar molecules in the ground state, there are extra interaction capabilities and tunably parameters due to the existence of a large tunable electric dipole moment under the influence of an external electric field. For that reason, these molecules interact with each other via dipole-dipole interaction (see figure 1.1). The effective potential for a polarized sample is the following:

$$V_{eff}(\mathbf{r}) = \frac{d^2}{r^3}(1 - 3\cos^2\theta) - \frac{C_6}{r^6} \tag{1.1}$$

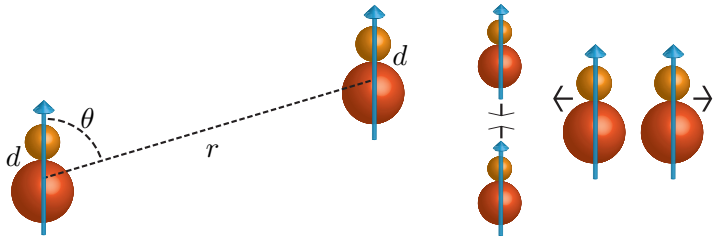

Figure 1.1: Dipolar interaction between two molecules that have a permanent electric dipole d, are polarized and which have their center of mass separated by r. Their dipoles make an angle θ with the line that unites their center of mass. This interaction is repulsive in the case the dipoles are positioned side-by-side and attractive if head-to-tail.

Without any external electric field the average net dipole moment is zero

and the molecules interact via Van der Waals interaction $-C_6/r^6$, due to induced fluctuating dipole moments. However, when an electric field is applied, a permanent dipole moment is induced and the molecules interact via dipole-dipole interaction. This interaction is very strong, which allows the possibility to observe its long-range character (falls off with $1/r^3$, which is long range in 3 dimensions) [22], as opposed to the contact interaction characteristic between atoms. In addition, the potential is anisotropic, which means that it can be either repulsive or attractive depending on the orientation of the dipoles with respect to the internuclear axis - repulsive if the dipoles are located side-by-side and attractive if they are head-to-tail. The degree of the polarization and the intensity of the dipole moment depend on the magnitude of the electric field. For NaK molecules, the molecular species that is intended to be created in this experiment, the field strength needed for the complete polarization of the molecules is approximately 8kV/cm.

With all these possibilities, cold molecules are of great interest and are at the moment very explored by theorists. Hence, when experimentally reached, many interesting concepts and phenomena may be developed and observed: quantum computation [23], observation of superfluid, supersolid, Mott-insulator, checkerboard and collapse phases [24], lattice-spin models [25], self-assembled crystals [26], observation of the extended Hubbard model phonon-mediated long-range interaction if extra particles (atoms or molecules) are added to the self-assembled polar molecules crystal [27], observation of Mott-insulators with fractional fillings - devil's staircase [28], not to mention many other theories. Some proposals require that the molecules are loaded into an optical lattice.

However, the increased complexity of the internal structure of molecules, at the same time that it makes them interesting, is a disadvantage with respect to their cooling and trapping. So far, it was only possible to laser cool two molecular species: SrF [29] and YO [30]; since in most molecules it is not possible to have a closed transition cycle. Hence, the cooling of molecules has been done through other ways, like direct cooling methods such as collisions with a buffer gas [31] or Stark deceleration [32]. So far, only temperatures on the order of tens to hundreds of mK and densities of $(10^6 - 10^8)$ cm^{-3} could be achieved. More recently, also an opto-electrical cooling scheme was implemented which made possible to achieve temperatures around 1mK [33]. These schemes, despite of the obvious advantage of allowing to cool several kinds of molecules and not exclusively the alkaline-based ones, only attain phase space densities that are too far away from quantum degeneracy (see figure 1.2).

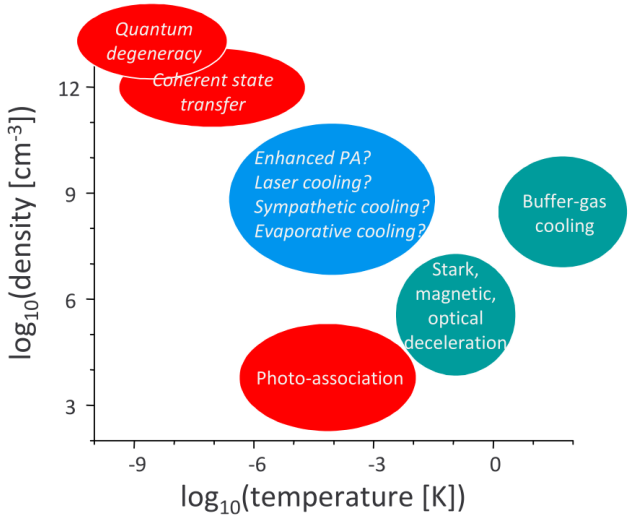

Figure 1.2: Several techniques used to produce cold molecules and the range of density and temperatures that each can achieve. [34]

There are also other approaches to cool molecules that lead to higher densities and lower temperatures: the indirect cooling methods. These explore the large knowledge and expertise of laser cooling of atoms, creating molecules by associating the atoms after cooling them separately. One of these alternatives is to photoassociate the atoms using one or two photon transitions[35, 36, 37], which leads to phase space densities still far away from quantum degeneracy (as it is possible to observe in 1.2) and temperatures on the order of hundreds of μK. Furthermore, as it relies on spontaneous decay, several levels get populated in the end. There is another indirect method, in which the atoms are associated by sweeping a magnetic field across a Feshbach resonance [38, 39, 40]. This results in a phase space density as large as the atoms' one since the process is adiabatic and reversible. However, despite the molecules being translationally cold, this technique leaves them in a weakly bound highly excited state for which the dipole moment is much lower than the one in the ground state. Therefore, if the molecules are left in that excited state, the choice of polar molecules for the desired purpose would be in vain. Additionally, the inelastic collisions between molecules in this excited state will lead to the quenching of the internal state into a low-energetic one by rovibrational relaxation. If the energy released in the process is larger than the trap depth there will be major losses, if not, it will result in an undesirable heating of the sample. To avoid this situation, the molecules must be transferred to the rovibrational ground-state, where they can no longer decay and can have a large dipole moment in the presence of a DC electric field. To achieve that, it is desirable a fully coherent process that leaves all

the molecules in only one internal state: the process is called stimulated Raman adiabatic passage (STIRAP) [41] and it is the main theme of this thesis. In this two-photon Raman transfer, the molecules are left in the ground state while no heating is produced. This has been achieved for heteronuclear molecules with $^{40}K^{87}Rb$ [42]. However, this molecules are reactive in the ground state, which leads to their decay into the lower energy level formed by K_2 and Rb_2.

It is easy to understand the need for a two-photon process: the Feshbach and the ground states have different electronic spin and the dipole transition selection rules suppress this kind of transitions. Furthermore, as the Feshbach molecules are so loosely bound, their inner turning point is much larger than the equilibrium internuclear distance in the ground state and therefore the Franck-Condon principle strongly suppresses the transition. With this is mind, there is a clear necessity to use an excited state that has large Franck-Condon factors for transitions to both states. However, the excited state is lossy as it can decay to lower states. For that not to happen the coupling between the states through the light field must assure that this excited state never gets populated: that is the main advantage of implementing the STIRAP scheme.

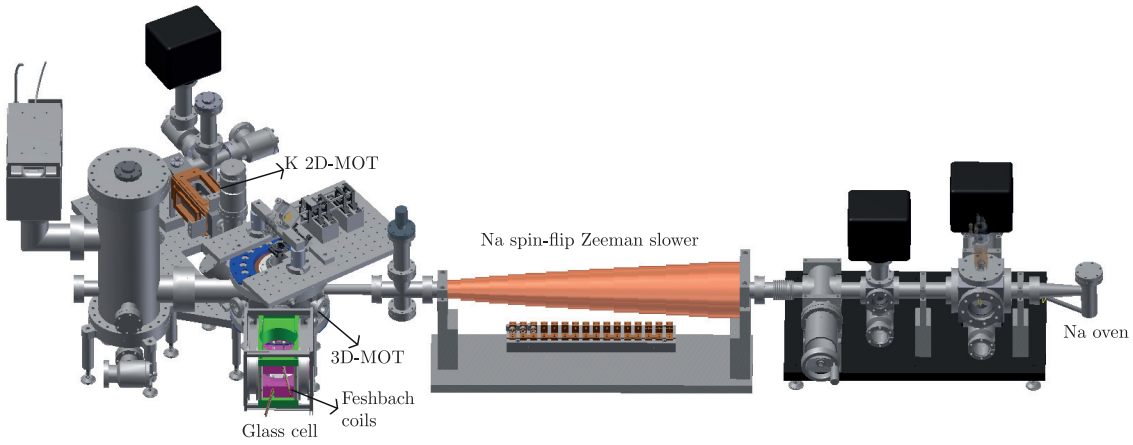

Figure 1.3: Overall scheme of the experiment.

In the experiment which this thesis is a part of, ^{23}Na and ^{40}K or ^{39}K were chosen, which means that it is possible to obtain either fermionic (^{40}K) or bosonic (^{39}K) molecules. These molecules in the ground state have a large permanent dipole moment of about 2.8Debye [43] which allows the study of molecules that interact via dipole-dipole interaction. Also, unlike KRb, in their ground states these molecules are nonreactive and chemically stable since it is not energetically favorable to exchange atoms nor to form of a trimer+atom [44]. This fact allows the existence of long-lived dipolar molecules.

Both the sodium atoms, after being slowed by the spin-flip Zeeman slower, and the potassium ones, after being cooled in the 2D magneto-optical trap (MOT), are cooled further in the dual species 3D MOT and loaded into a magnetic trap where they will be evaporatively cooled. Afterwards, both species are transported in an optical dipole trap into the glass cell where the Feshbach coils will associate the atoms into molecules. Only here will the STIRAP scheme transfer the molecules into the ground state. All the experiments on the molecules will be carried out inside this glass cell.

1.1 Outline

This thesis describes the development and characterization of the laser setup that will be used to implement a STIRAP scheme, which will transfer the molecules to their rovibrational ground state. This Raman process requires laser light with two different wavelengths: 652.654(8)nm and 486.995(5)nm, calculated numerically. As the uncertainty in the wavelengths is still too large for the desired purpose, there will be the necessity of sweeping the frequency. To achieve that, two lasers with the desired frequencies for the STIRAP scheme are locked to a reference cavity. A second pair of lasers, which provide the light for the experiment while beat locked to the frequency stabilized lasers, are swept in frequency in order to find the ones for which the transfer efficiency is maximum.

The theoretical knowledge needed for the understanding of the transfer scheme is presented in the second chapter, with an overview of molecular physics, particularities of the Feshbach molecules, a detailed explanation of the STIRAP scheme and the requirements which it has.

The setup that will provide light for the STIRAP scheme is explained in the third chapter where the optical setup will be thoroughly addressed, as well as the previously referenced cavity and the method used for locking the master laser to it.

The experimental results are shown in the fourth chapter where the characterization of the setup is presented and explained, such as the electronic circuits used, the line widths measured, the frequency drift of the cavity and its zero-expansion temperature.

In the last chapter a small synopsis of what was done is exposed, as well as what is still needed to be developed for the attainment of the goal of the experiment.

2 Theoretical Background

2.1 Molecular physics

The laser light frequencies used in the STIRAP scheme were chosen according to the selected electronically excited state, which has as a requisite large Franck-Condon factors to both the Feshbach and the ground states, allowing, through this intermediate level, the coupling between those states. In order to understand how that excited state was chosen, a brief overview of molecular physics phenomena interesting for this subject is here presented.

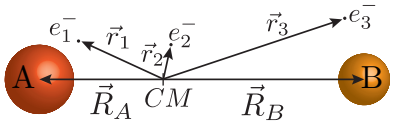

Figure 2.1: Diatomic molecule with respective coordinate system: CM is the position of the center of mass of the molecule, R_A and R_B are the position of the nuclei and r_i are the position of the n electrons with respect to the center of mass.

For a free diatomic molecule with internuclear distance $|\mathbf{R}| = |\mathbf{R_A}| + |\mathbf{R_B}|$, with n electrons, assuming no spin interactions the time-independent Schrödinger equation is the following:

$$\hat{H}\Psi = \left[\hat{T}_e + \hat{T}_N + \hat{V}(\mathbf{R}, \mathbf{r_1}, .., \mathbf{r_n})\right] \Psi(\mathbf{R}, \mathbf{r_1}, .., \mathbf{r_n}) = E\Psi(\mathbf{R}, \mathbf{r_1}, .., \mathbf{r_n}) \tag{2.1}$$

where $\hat{T}_e = -\frac{\hbar^2}{2m}\sum_i \nabla^2_{r_i}$ is the electronic kinetic energy operator, $\hat{T}_N = -\frac{\hbar^2}{2\mu}\nabla^2_R$ the nuclear one with μ being the nuclei reduced mass, and $V(\mathbf{R}, \mathbf{r_1}, .., \mathbf{r_n})$ is the potential interaction between nuclei, electrons and nuclei and electrons .

It is not possible to reach an exact solution for this hamiltonian and therefore approximations should be made. Some of which will be presented in this section.

2.1.1 Born-Oppenheimer approximation

The nuclei are much heavier than the electrons, which causes their time scales to be significantly different. The Born-Oppenheimer approximation [45] states that, as the electrons are extremely light in comparison with protons, they follow the nuclei adiabatically and have no relaxation time. This legitimates the ansatz where the electronic and nuclear part of the molecular wavefunction are separated:

$$\Psi(\mathbf{R}, \mathbf{r_1}, .., \mathbf{r_n}) = \sum_i \chi_i(\mathbf{R})\phi_i(\mathbf{R}, \mathbf{r_1}, .., \mathbf{r_n}) \tag{2.2}$$

where the coefficients χ_i represent the nuclear motion at the electronic state ϕ_i, which are the eigenfunctions of the electronic wave equation, assuming the nuclei position fixed:

$$\left(\hat{T}_e + V(\mathbf{R}, \mathbf{r_1}, .., \mathbf{r_n})\right) \phi_i(\mathbf{R}, \mathbf{r_1}, .., \mathbf{r_n}) = E_i(\mathbf{R}, \mathbf{r_1}, .., \mathbf{r_n})\phi_i(\mathbf{R}, \mathbf{r_1}, .., \mathbf{r_n}) \tag{2.3}$$

Since the wavefunctions ϕ_i obey the orthonormality property $\langle\phi_i|\phi_j\rangle = \delta_{ij}$, they form a complete basis.

If (2.2) is inserted into equation (2.1) and projected it onto the electronic functions, the following equation is reached:

$$\sum_i \langle\phi_j(\mathbf{R}, \mathbf{r_1}, .., \mathbf{r_n})|\hat{T}_e + \hat{T}_N + \hat{V}(\mathbf{R}, \mathbf{r_1}, .., \mathbf{r_n}) - \hat{H}|\chi_i(\mathbf{R})\phi_i(\mathbf{R}, \mathbf{r_1}, .., \mathbf{r_n})\rangle = 0 \tag{2.4}$$

$$j = 1, 2, ...$$

When the orthonormality property and equation (2.3) are used, this follows:

$$\sum_i \langle\phi_j(\mathbf{R}, \mathbf{r_1}, .., \mathbf{r_n})|\hat{T}_N|\chi_i(\mathbf{R})\phi_i(\mathbf{R}, \mathbf{r_1}, .., \mathbf{r_n})\rangle + (E_j(\mathbf{R}) - E)\chi_j(\mathbf{R}) = 0 \tag{2.5}$$

$$\begin{aligned} \text{where} \quad \hat{T}_N|\chi_i(\mathbf{R})\phi_i(\mathbf{R}, \mathbf{r_1}, .., \mathbf{r_n})\rangle = -\frac{\hbar^2}{2\mu}[&\chi_i(\mathbf{R})(\nabla_R^2\phi_i(\mathbf{R}, \mathbf{r_1}, .., \mathbf{r_n})) \\ &+ 2(\nabla_R\chi_i(\mathbf{R}).\nabla_R\phi_i(\mathbf{R}, \mathbf{r_1}, .., \mathbf{r_n})) \\ &+ \phi_i(\mathbf{R}, \mathbf{r_1}, .., \mathbf{r_n})(\nabla_R^2\chi_i(\mathbf{R}))] \end{aligned} \tag{2.6}$$

The nuclear part of the molecular wavefunction, as the nuclei is heavier than the electrons, is much more localized spatially than the electronic one, which allows the following approximation: $\nabla_R\phi_i(\mathbf{R}, \mathbf{r_1}, .., \mathbf{r_n}) \ll \nabla_R\chi_i(\mathbf{R})$, which, if

inserted in (2.5) gives rise to the nuclear wave equation:

$$\left[-\frac{\hbar^2}{2\mu}\nabla_R^2 + E_j(\mathbf{R}) - E\right]\chi_j(\mathbf{R}) = 0 \qquad j = 1, 2, ... \tag{2.7}$$

It is now clear that $E_j(\mathbf{R})$ correspond to the energy of the frozen electronic states and can be represented by the Born-Oppenheimer potentials (figure 2.2). As it is possible to observe, this potential goes to infinity for very small internuclear distances, which can be explained by the Coulomb repulsion between nuclei. Another characteristic of the potential is that, as the nuclei get further apart, the energy tends to an asymptote that is the sum of the energy of the independent atoms in the states that originate that electronic molecular state in particular. For electronic states where the Born-Oppenheimer potential has a minimum below the asymptote, there may exist molecular bound states.

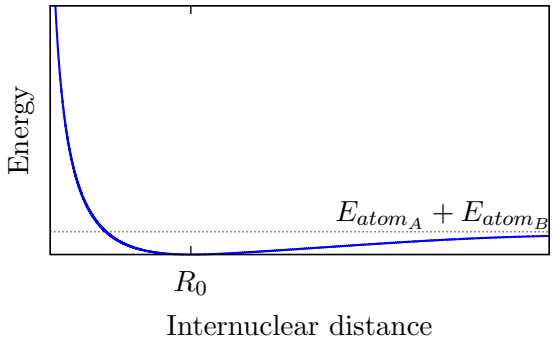

Figure 2.2: Born-Oppenheimer potential with a minimum in energy for an internuclear distance of R_0 and an energy's asymptotic value for large internuclear distances which corresponds to the sum of the individual atoms' energy

This approximation requires that the difference between electronic states has to be much larger than between vibrational and rotational states.

2.1.2 Rotation and Vibration

The nuclear function $\chi_i(\mathbf{R})$ for a particular electronic state i can in the rigid rotor approximation be decomposed in a radial part $\xi(R)$ and an angular one, which corresponds to the spherical harmonics $Y_{J,m_J}(\theta, \Phi)$:

$$\chi_i(\mathbf{R}) = \frac{\xi_{i,v,J}(R)Y_{J,m_J}(\theta, \Phi)}{R} \tag{2.8}$$

Therefore, it exists a rotational energy associated with the orbital angular

momentum **J**:

$$E_r = \frac{\mathbf{J}^2}{2I_0} = BJ(J+1), \qquad J = 0, 1, ... \tag{2.9}$$

where $B = \frac{\hbar^2}{2I_0}$ is the rotational constant and $I_0 = \mu R_0^2$ is the moment of inertia. It is possible to interpret this result by looking at the molecule as a rigid body that rotates around an axis that passes in its center of mass and is perpendicular to the internuclear axis, since the moment of inertia about the internuclear axis is assumed zero.

By inserting (2.8) in (2.9) a radial equation is reached:

$$\left[-\frac{\hbar^2}{2\mu} \left(\frac{d^2}{dR^2} - \frac{J(J+1)}{R^2} \right) + E_i(R) - E_{i,v,J} \right] \xi_{i,v,J}(R) = 0 \tag{2.10}$$

Assuming that the nuclear motion occurs mainly near the minimum R_0, it is possible to expand (2.10) in a Taylor series:

$$E_i(R) \approx E_i(R_0) + \frac{k}{2}(R - R_0)^2 \tag{2.11}$$

If (2.9), (2.10) and (2.11) are combined, it is noticeable that the total energy is the sum of the electronic, rotational and vibrational energies

$$E_{i,v,J} = E_i(R_0) + E_r + E_v \tag{2.12}$$

provided that the vibrational energy is the eigenvalue of the harmonic oscillator equation

$$\left[-\frac{\hbar^2}{2\mu} \frac{d^2}{dR^2} + \frac{k}{2}(R - R_0)^2 - E_v \right] \chi_v = 0 \tag{2.13}$$

Therefore the vibrational spectrum is given by $E_v = \hbar\omega_0(v + 1/2)$ with $\hbar\omega_0 = \hbar\sqrt{k/\mu}$ as the energy difference between consecutive levels. However, this is only valid for small internuclear distances, and therefore for low vibrational states. For higher ones in reality the distance between the levels decreases and consequently more realistic models should be developed and applied.

At this point, it is evident that for each electronic state of the molecule, there are several vibrational and rotational levels which have different energy scales. A transition between two rotational states maintaining the vibrational and elec-

tronic ones corresponds to the microwave or far infrared region of the spectrum. The transition between two different vibrational states has a frequency in the mid-infrared region and electronic transitions lie in the visible and the ultraviolet range.

Furthermore, it has to be noted that a heteronuclear diatomic molecule is not a simple rotator with a moment of inertia zero about its internuclear axis. As there are electrons around it, the moment of inertia is small (due to the small electrons' mass in comparison to the nuclei's one) but finite. Therefore these molecules should be regarded as symmetric tops, for which the principal moment of inertia about the internuclear axis is much smaller than the the other two that are about perpendiculars to it (and that are equal one to the other). However, the angular momentum associated to all of them can have the same order of magnitude, since the electrons rotation is quantized.

The angular momentum vectors that exist in a symmetric top are shown in the figure 2.3. In this picture **J** is the total angular momentum around which the system rotates. The projection of the later onto a plane perpendicular to the internuclear axis is **N**, which corresponds to the rotational angular momentum of the nuclei. And **Ω** is the projection of the total angular momentum of the electron onto the internuclear axis.

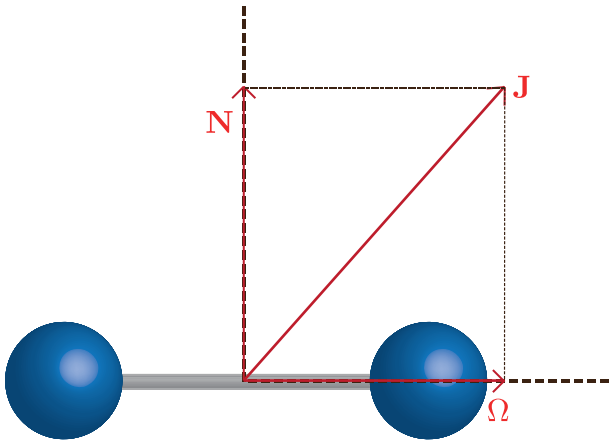

Figure 2.3: Vectorial scheme of a molecule that can be regarded as a symmetric top rotating around the total angular momentum **J**

2.1.3 Hund's cases

The molecules have a large number of angular momenta: electronic spin **S**, electronic orbital angular momentum **L**, rotational angular momentum **N** and total angular momentum of the molecule **J**. These angular momenta can couple

among themselves in several ways. To obtain an approximate description of the coupled system, a hierarchy of coupling strength can be determined. The several orders of the hierarchy are called Hund's cases. They are five, however only the case a) and c) are of interest for the understanding of this thesis and therefore, only those will be presented here.

Hund's case a

This case is usually the one related to heteronuclear diatomic molecules with a small internuclear distance.

In this case the electronic motion is strongly coupled to the internuclear axis: **L** is, by electrostatic interaction, coupled to this axis and, by spin-orbit coupling, **S** is coupled to **L**. This causes that the projection of **L** and **S** onto the internuclear axis (Λ and Σ, respectively) to be good quantum numbers, as well as their sum $\Omega = |\Lambda + \Sigma|$, which constitutes a vector ($\mathbf{\Omega}$) that lies on the internuclear axis. The sum of this vector with the rotational nuclear momentum **N** is the total angular momentum **J** which has a constant direction and magnitude. Both $\mathbf{\Omega}$ and **N** rotate around it - nutation. The precession of **L** and **S** around the internuclear axis is much faster than nutation. The good quantum numbers are Λ, Σ, Ω and J.

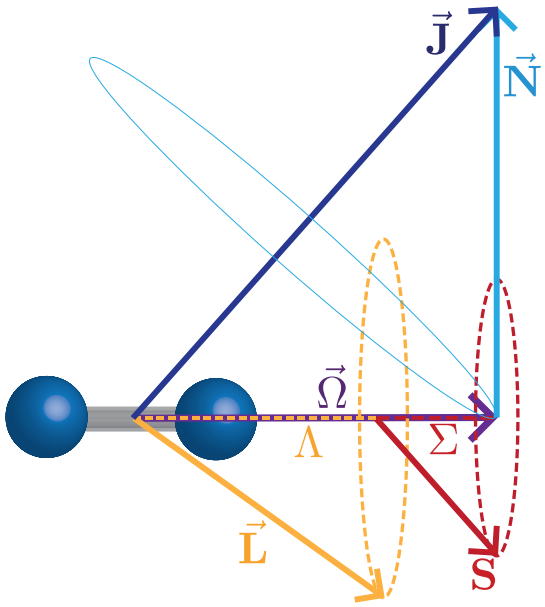

Figure 2.4: Vectorial scheme of a molecule that obeys the Hund's case a: the fast rotation of $\vec{L}$ and $\vec{S}$ around the internuclear axis are represented by the dashed ellipses and the solid ellipse represents the much slower nutation of $\vec{N}$ and $\vec{\Omega}$

A molecular electronic state with Λ, Σ, Ω and J is usually denoted in spec-

troscopic notation by $\alpha^{2\Sigma+1}\Lambda_{\Omega}^{+/-}$. Here $\Lambda = 0, 1, 2, ...$ corresponds to Σ, Π, Δ,... The superscript signal $+/-$ is associated to the reflection symmetry along any plane that contains the internuclear axis. And moreover, as this is not enough to completely define the states, there is an "energy counting label" α, which is X for the rovibrational ground state and then, in the order of their energy, the states are labeled by A,B,C,... in case they have the same multiplicity $(2\Sigma + 1)$ of X or a,b,c,... in case the multiplicity is different from the X's one. For the electronic excited states, this labeling is made with numbers.

Hund's case c

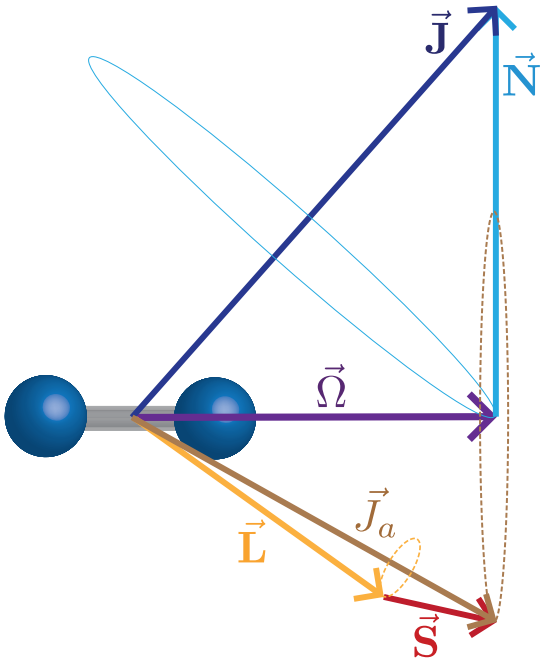

Figure 2.5: Vectorial scheme of a molecule that obeys the Hund's case c: the fast precession of $\vec{L}$ and $\vec{S}$ around $\vec{J}_a$ and of this around the internuclear axis are represented by the dashed ellipses and the solid ellipse represents the much slower nutation of $\vec{N}$ and $\vec{\Omega}$

In the case of near-threshold states, where the internuclear distance is large, **L** and **S** do not couple individually to the internuclear axis since the spin-orbit coupling is much stronger and leads to the couple of one to the other: $\mathbf{J}_a = \mathbf{L} + \mathbf{S}$. Being Ω the projection onto the internuclear axis of $\mathbf{J}_a$, and $\mathbf{\Omega}$ the correspondent vector along that axis: $\mathbf{J} = \mathbf{N} + \mathbf{\Omega}$. As in this case, Λ and Σ are not good quantum numbers, the notation has to change: numbering starting from the lowest lying energetic state followed by $(\Omega)^{+/-}$.

2.1.4 Selection rules

The selection rules (explained in detail in [46]) are probabilities of a transition to occur based on an evaluation of the elements that compose the electric dipole moment matrix $\langle \Psi_i | \hat{\mathbf{d}} | \Psi_j \rangle$. The explanation below comprehends exclusively the electric dipole radiation and only the selection rules that apply to the heteronuclear diatomic molecules.

If the molecules are considered symmetric tops and no electronic transitions are concerned, the rotational and vibrational selection rules are the following:

$$\Omega = 0 \longrightarrow \Delta J = \pm 1 \tag{2.14}$$

$$\Omega \neq 0 \longrightarrow \Delta J = 0, \pm 1 \tag{2.15}$$

$$\Delta v = 0, \pm 1 \tag{2.16}$$

where the harmonic oscillator approximation was used. The case $\Delta v = 0$ only occurs in the the presence of a permanent dipole, which is the case for heteronuclear diatomic molecules, corresponding to a purely rotational transition. As the molecular potential is not a perfect harmonic oscillator, $\Delta v > 1$ transitions can also happen, with the probability of the transition decreasing rapidly with the increase in the vibrational number difference.

In the case of electronic molecular transitions, the general selection rules comprise the following:

$$\Delta J = 0, \pm 1, \text{ except for } J = 0 \longrightarrow J' = 0 \tag{2.17}$$

$$\tag{2.18}$$

Additionally, there are rules that apply to different Hund's cases. The selection rules that apply only to Hund's case a are the undermentioned:

$$\Delta\Lambda = 0, \pm 1 \text{ and therefore } \Sigma \nleftrightarrow \Delta \tag{2.19}$$

$$\Sigma^+ \leftrightarrow \Sigma^+ \text{ and } \Sigma^- \leftrightarrow \Sigma^- \text{ are allowed but } \Sigma^- \nleftrightarrow \Sigma^+ \tag{2.20}$$

$$\Delta S = 0 \tag{2.21}$$

$$\Delta\Sigma = 0 \tag{2.22}$$

$$\Delta J \neq 0 \text{ for } \Lambda = 0 \longrightarrow \Lambda' = 0 \tag{2.23}$$

In the case the coupling case that applies is c), the following selections rules

exist:

$$\Delta\Omega = 0, \pm 1 \tag{2.24}$$

$$0^+ \leftrightarrow 0^+ \text{ and } 0^- \leftrightarrow 0^- \text{ are allowed but } 0^- \nleftrightarrow 0^+ \tag{2.25}$$

Whenever both coupling cases can be applied (one to each state), only the rules that exist for both cases are applicable.

2.1.5 Franck-Condon Principle

When an electronic transition happens, there are no vibrational selection rules. It will be shown that its strength depends on the Franck-Condon factors, which correspond to the overlap between both vibrational wavefunctions.

Quantum mechanically, and assuming the derivation is valid for every combination of rotation eigenvalues [46], this principle [47] can be explained based on the calculation of the square of the electric moment, which is proportional to the probability of transition from $|\chi_v^g \phi_{el}^g\rangle$ to $|\chi_v^e \phi_{el}^e\rangle$:

$\left|\langle \chi_v^g \phi_{el}^g | \mathbf{d} | \chi_v^e \phi_{el}^e \rangle\right|^2$

where the moment can be separated into a nuclear and an electronic part:

$\mathbf{d} = \mathbf{d}_e + \mathbf{d}_N$

$\left|\langle \chi_v^g \phi_e l^g | \mathbf{d}_e | \chi_v^e \phi_{el}^e \rangle + \langle \chi_v^g | \mathbf{d}_N | \chi_v^e \rangle \langle \phi_e l^g | \phi_{el}^e \rangle\right|^2$

in which it was assumed that the nuclear dipole moment doesn't depend on the electronic coordinates.

By the orthonormality property, $\langle \phi_{el}^g | \phi_{el}^e \rangle$ vanishes. Taking into account that the variation of $\langle \phi_{el}^g | \mathbf{d}_e | \phi_{el}^e \rangle$ (which corresponds to the probability of electronic transition) is slow with the internuclear distance variable, it is possible to consider this distance constant during a transition (Condon approximation), which results in:

$$\text{Probability of transition} \propto \left| \overline{\langle \phi_{el}^g | \mathbf{d}_e | \phi_{el}^e \rangle} \langle \chi_v^g | \chi_v^e \rangle \right|^2 = \overline{d_e}^2 f_{v-v'}^2 \tag{2.26}$$

where $f_{v-v'}$ is the Franck-Condon factor. For the vibrational levels $v = 0$ the wavefunction is larger at the equilibrium internuclear distance, whereas for the excited vibrational states it is near the classical turning points, where the velocity is zero, that there is a maximum in the magnitude of the wavefunction.

It is also possible to construct a semi-classical picture for this principle; as

it was presented previously, the nuclei move much more slowly than the electrons, and therefore, it is possible to say that the electronic transitions occur instantaneously when compared to the vibrations. After an electronic transition the nuclei is at practically the same position as before, and like that, these transitions are represented by vertical lines in the Born-Oppenheimer diagrams. This corresponds to the Franck-Condon principle, which requires that during the transition the change in position and momentum of the nuclei are small, for them to adjust quickly to the new electronic state.

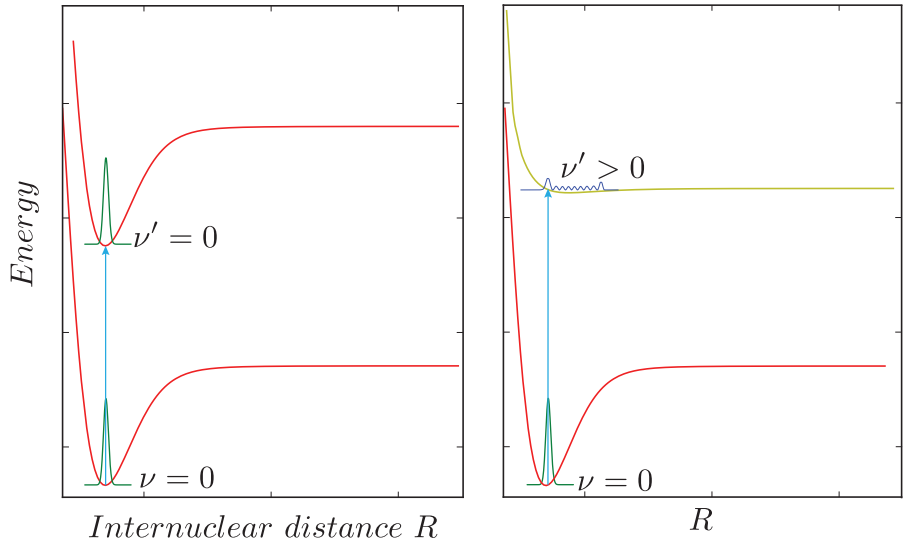

(a) (b)

Figure 2.6: Molecular potentials showing the most probable transitions from $\nu = 0$ to a) $\nu' = 0$ and b) $\nu' > 0$ according to the Franck-Condon principle with respective wavefunctions

Considering a molecule in a state $\nu = 0$ (see figure 2.6) with a Born-Oppenheimer potential minimum at an internuclear distance R_0, a transition to an excited electronic state will be more likely to occur in two cases:
a) the excited state is $\nu' = 0$ and its Born-Oppenheimer potential has the minimum at R_0;
b) the excited state is $\nu' > 0$ and its Born-Oppenheimer potential has a turning point at R_0.
This can easily be explained by the fact that this cases maximize the overlap of the wavefunction of the states involved in the transition, since $\nu = 0$ vibrational states have a maximum in the magnitude of their wavefunction at R_0 and for the excited vibrational states, that magnitude is larger at the turning points.

2.2 Feshbach molecules

By using the Feshbach association it is possible to coherently pass from atoms to molecules by changing the scattering length when a magnetic field is swept through a resonance (for a review see [48, 49, 50]).

As the Van der Waals length is much smaller than the separation between the atoms, the atoms almost don't interact with each other and the probability of the existence of three body collisions is small and thus can be neglected. As, when the atoms are separated by a large distance , they can be considered free, the ansatz for elastic scattering is valid, allowing the formulation of the scattering wavefunction as the sum of the incoming plane-wave and an outcoming spherical one:

$$\psi(\mathbf{r}) \approx e^{ikz} + f_k(\theta,\phi)\frac{e^{ikr}}{r}, r \longrightarrow \infty \tag{2.27}$$

By switching to a partial waves basis $\phi_{k,l,m} = \frac{u_{k,l}(r)}{r}Y_l^m(\theta,\phi)$ the time independent Schrödinger equation for the collision of two particles with reduced mass μ gets:

$$\left[-\frac{\hbar^2}{2\mu}\frac{d^2}{dr^2} + \frac{l(l+1)\hbar^2}{2\mu r^2} + V(r)\right] u_{k,l}(r) = E u_{k,l}(r) \tag{2.28}$$

where $V(r)$ is the effective potential of the scattering and the second term is a centrifugal barrier. In collisions with atoms near quantum degeneracy, the high angular momentum partial waves can't penetrate into this barrier which makes the s-waves (l=0) the only ones with significance in the process. The s-wave scattering properties are well described if the potential the atoms feel can be considered a contact potential ($\frac{4\pi\hbar^2}{m}\delta^{(3)}$) [51].

In the following explanation only two states are considered, which is a valid approximation in the vicinity of a resonance since the interaction is typically dominated by the coupling of only two states.

Hyperfine states that have an asymptotic energy larger than the scattering state energy are called closed channels, while if that asymptotic energy is smaller they are called open channels. There is a Feshbach resonance when the kinetic energy of the atoms that collide is equal to the bound state of the closed channel, as it is possible to observe in figure 2.7.

An external magnetic field allows to tune by the Zeeman effect the bound state energy of the closed channel and bring it in resonance with the open chan-

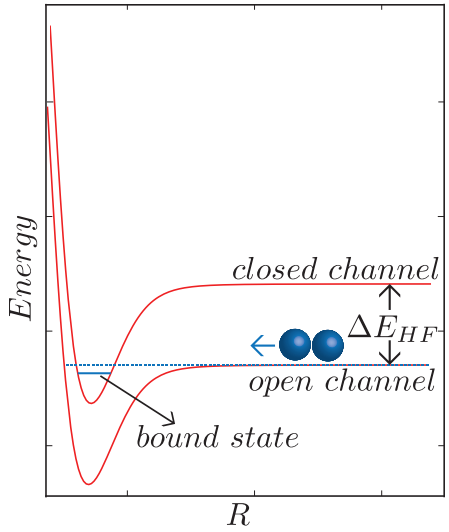

Figure 2.7: Scheme of a Feshbach resonance, that occurs when the bound state's energy of the closed channel coincides with the kinetic energy from the atoms that are involved in the collision.

nel, since the channels have different hyperfine states and hence magnetic moments.

In fact, open and closed channels are coupled by a spin-flip caused by the overwhelming at short distances of the exchange Coulomb interaction over the hyperfine interaction. When the superposition channel has a state passing by the dissociation threshold, a Feshbach resonance occurs.

The Feshbach resonance can be described by an expression for the scattering length as a function of the magnetic field applied:

$$a(b) = a_{bg}\left(1 - \frac{\Delta}{B - B_0}\right) \tag{2.29}$$

, where a_{bg} is the off-resonant scattering length, which is connected to the last bound state in the open channel. B_0 is the magnetic field for which the scattering length diverges and Δ is the width of the resonance.

The scattering length in this process diminishes always, as it is possible to see in figure 2.8, until it diverges with the appearance of the bound state, the scattering length becomes very large and the potential between the atoms repulsive, making the energetically lower bound state favorable to populate. Therefore, where initially existed a crossing in the energy between the molecule state and the individual atoms state, exists an avoided crossing with the sweeping of the magnetic field. However, if the sweeping is too fast the coupling between the hyperfine states isn't made and no molecules are formed.

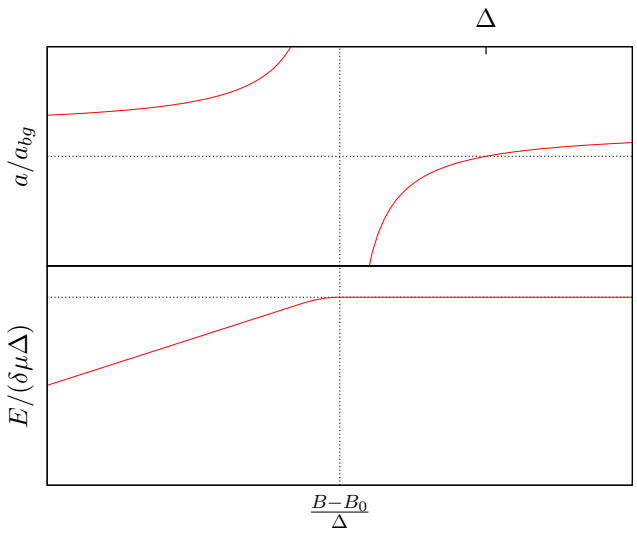

Figure 2.8: Variation of the scattering length and of the energy of the system in the vicinity of a Feshbach resonance with the magnetic field.

In bosons this Feshbach association has major losses caused by either two body processes, such as spin-exchange and magnetic dipole relaxation, or three-body processes like molecular recombination, which doesn't occur in fermions due to the Pauli blocking. The Bose-Fermi mixture is in an intermediate case since this blockade phenomenon only occurs if the collision of the molecule is with a fermion. So, whereas the conversion efficiency for fermions depends only on the ramp speed and it can be made very close to 1, for bosons the magnetic field must be swept at a rate that is slow enough to enable the adiabatic conversion of atoms into molecules but also fast enough to minimize inelastic collisions. The transfer efficiency is given by $1 - exp(-\beta/\dot{B})$ where $\dot{B}$ is the magnetic field sweep rate and $\beta = \alpha n \Delta a_{bg}$, with a_{bg} as off-resonant scattering length, n as the density of the atomic cloud, Δ as the width of the resonance and α as a fitting parameter. For the transfer to be adiabatic $\dot{B} \ll \beta$ [52].

To verify the presence of molecules the ramp can be reversed, because, as the process is coherent, the molecule is dissociated into atoms.

2.3 Stimulated Raman adiabatic passage

As it was already mentioned in the previous section, by Feshbach association, very weakly bound molecules are created. It is desirable to transfer the molecules to the ground state, where they can no longer decay and release enough energy to dissociate molecules and heat the gas. Therefore, one has to find a way of car-

rying that binding energy (around 150THz) out of the gas. The transfer, which ideally should be target selective and efficient, is the STIRAP - STImulated Raman Adiabatic Passage [41]. This scheme was first realized in 1988 [53] between vibrational molecular levels in molecular beams that pass sequentially through two spatially displaced laser beams. The transfer between a Feshbach state of an ultracold molecule and its rovibrational ground state was accomplished in 2008 [42]; this is the goal of the project of this thesis.

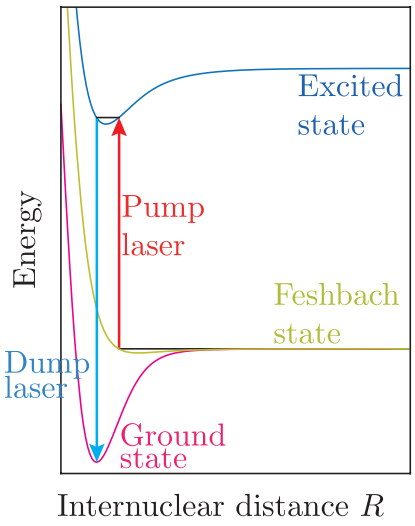

Figure 2.9: Scheme of the Born-Oppenheimer potentials of the states which participate in Stirap. The pump laser has an energy that corresponds to the difference of energy between the excited and the Feshbach states and the dump laser to the energy difference between the excited and the final ground state.

This scheme consists of a sequential interaction between the molecules and two laser beams (see figure 2.9): the pump laser couples the Feshbach state ($|1\rangle$) to the intermediate state ($|2\rangle$) and the dump laser couples the intermediate state ($|2\rangle$) to the rovibrational ground state ($|3\rangle$). The Feshbach state can be considered metastable since, as it is a high vibrational state, its Frank-Condon factors to lower lying states is very small and the radiative decay is slow due to the fact that the energy difference between levels is small. However, whereas the initial and final states are stable against decays (at least in the time scale during which the process occurs), the intermediate level is short-lived and lossy and, when populated, the molecule immediately decays into other lower energy states and get lost of the process. For that not to happen, in this scheme, a "counter-intuitive" pulse sequence will be implemented, in which a dark eigenstate of the system molecules+field, that doesn't populate the intermediate lossy state, is always adiabatically followed. Initially, when the molecules are in the Feshbach

state, the dark state is the only eigenstate populated if the dump laser is turned on and the pump off. At the end, when the molecules are in the ground state, the dark state is the populated eigenstate of the system if the dump laser is off and the pump one is on. This justifies the use of the STIRAP pulse sequence.

2.3.1 Three-level hamiltonian

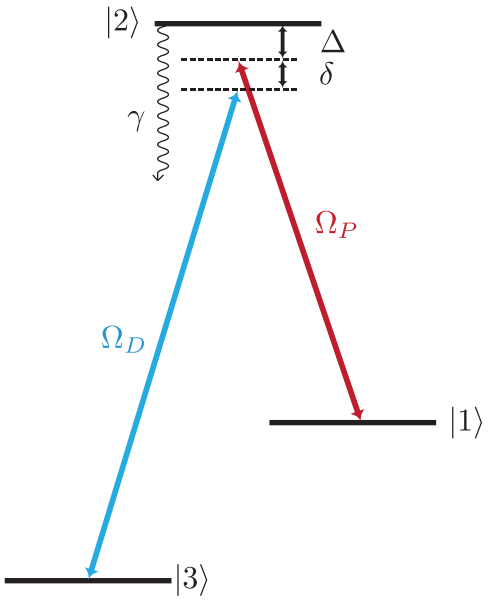

Figure 2.10: Three-level system scheme - the explanation of the notation used is in the text.

The hamiltonian of the 3-level system (for the derivations of the formulas in the two following sections see [41]) in the rotating wave approximation, for which the fast oscillation terms are neglected , is the following:

$$\hat{H}(t) = \frac{\hbar}{2}\begin{bmatrix} 0 & \Omega_P(t) & 0 \\ \Omega_P(t) & 2\Delta - i\gamma & \Omega_D(t) \\ 0 & \Omega_S(t) & 2\delta \end{bmatrix} \tag{2.30}$$

where $\Omega_P = \frac{d_{1-2}.|\mathbf{E_P}(t)|}{\hbar}$ and $\Omega_D = \frac{d_{2-3}.|\mathbf{E_D}(t)|}{\hbar}$ are the Rabi frequencies of the pump and dump lasers, respectively, where d_{i-j} is the transition dipole moment between the states i and j, $|\mathbf{E_P}(t)|$ and $|\mathbf{E_D}(t)|$ are the pump and dump lasers' electric field amplitudes. $\Delta = (E_2 - E_1)/\hbar - \omega_P$ is the one-photon detuning, $\delta = (E_1 - E_3)/\hbar - (\omega_D - \omega_P)$ the two-photon detuning and γ the decaying rate of the intermediate level.

The transfer is very sensitive to δ and for it to be efficient, δ should satisfy the

Raman resonant condition and therefore vanish. So, assuming this case ($\delta = 0$), by diagonalizing the hamiltonian (2.30), it is possible to realize that one of the eigenstates is a linear superposition between the initial $|1\rangle$ and final states $|3\rangle$ and hasn't any component of the leaky intermediate state, that is the reason for it to be called dark state:

$$|\Psi_{DS}\rangle = \cos\Theta|1\rangle - \sin\Theta|3\rangle \tag{2.31}$$

in which the mixing angle is $\Theta = \tan^{-1}\left(\frac{\Omega_P(t)}{\Omega_D(t)}\right)$. The correspondent eigenvalue is $\omega_{DS} = 0$.

As the mixing angle is related to a ratio between Rabi frequencies, it is possible to control the lasers intensities in order for the state vector to follow adiabatically the dark state, and, in this way, never populate the intermediate level (which will happen if the state vector gets a component of either one of the two other eigenstates).

As initially the state vector of the system is parallel to $|1\rangle$ and in the end it is desirable for it to be in the state $|3\rangle$, it is wanted an adiabatic evolution of the angle Θ from 0 to $\pi/2$. In this way, $|\Psi\rangle$ always accompanies $|\Psi_{DS}\rangle$, and therefore both are always perpendicular to the state $|2\rangle$. This adiabatic change of the mixing angle is done by initially having the dump laser turned on and the pump laser off. During the transfer, the intensity of the dump laser is reduced in a smooth way while the intensity of the pump laser is increased and in the end, when all the molecules are in the rovibrational ground state, the ratio between the pump and the dump lasers is infinite:

$$\lim_{t\to-\infty}\frac{\Omega_p(t)}{\Omega_S(t)} = 0 \Longrightarrow \Theta(-\infty) = 0 \tag{2.32}$$

$$\lim_{t\to+\infty}\frac{\Omega_p(t)}{\Omega_S(t)} = \infty \Longrightarrow \Theta(+\infty) = \frac{\pi}{2} \tag{2.33}$$

2.3.2 Adiabacity conditions

In the case the Rabi frequencies are not high enough, the coupling will be poor. This has the result that the state vector $|\Psi\rangle$ will not accompany the dark state adiabatically, it will get components of the other eigenstates - bright states ($|\Psi^+_{BS}\rangle$

and $|\Psi^-_{BS}\rangle$)- and populate the lossy level which will afterwards decay:

$$|\Psi\rangle^+_{BS} = \sin\phi \sin\Theta|1\rangle + \cos\phi|2\rangle + \sin\phi\cos\Theta|3\rangle \tag{2.34}$$

$$|\Psi\rangle^-_{BS} = \cos\phi \sin\Theta|1\rangle - \sin\phi|2\rangle + \cos\phi\cos\Theta|3\rangle \tag{2.35}$$

where $\tan(2\phi) = \frac{\sqrt{\Omega_P^2+\Omega_D^2}}{\Delta}$. These eigenstates have the eigenvalues:

$$\omega^+_{BS} = \Delta + \sqrt{\Delta^2 + \Omega_P^2 + \Omega_D^2} \tag{2.36}$$

$$\omega^-_{BS} = \Delta - \sqrt{\Delta^2 + \Omega_P^2 + \Omega_D^2} \tag{2.37}$$

The non adiabatic coupling can be considered small if the projection in the bright states of the temporal derivative of the dark state is much smaller than the difference in energy between these states:

$$\left|\langle\Psi^\pm_{BS}|\dot{\Psi}_{DS}\rangle\right| \ll \left|\omega^\pm_{BS} - \omega_{DS}\right| \Leftrightarrow \left|\dot{\Theta}\right| \ll \left|\omega^\pm_{BS} - \omega_{DS}\right| \tag{2.38}$$

which corresponds to the following constraint assuming no one-photon detuning:

$$\left|\frac{\dot{\Omega}_P\Omega_D - \Omega_P\dot{\Omega}_D}{\Omega^2_{eff}}\right| \ll \Omega_{eff} \text{ ,where } \Omega_{eff} = \sqrt{\Omega_P^2 + \Omega_D^2} \tag{2.39}$$

To maintain the adiabacity this condition has to be fulfilled at all times during the transfer. However, it is possible to have a more general criterion for pulses with smooth shapes, in which $\langle\dot{\Theta}_{average}\rangle \propto \tau^{-1}$, being τ the transfer time which corresponds to the time during which the pulses overlap. Numerical simulations show that the pulse area is restricted as following:

$$\Omega_{eff}\tau \gg 10 \tag{2.40}$$

The implementation of STIRAP can either be made by displacing the two laser beams and make the molecules pass by with a certain velocity, or, in case the molecules are stationary, have pulsed lasers with a certain delay in time. As our molecules are stationary inside the glass cell only the latter can be implemented in our setup.

2.3.3 Pulse Delay

Initially, for the projection of the dark state on the state vector $|\Psi\rangle$, which corresponds to $|1\rangle$, be close to one, a large time delay between the lasers is desired.

However, if this delay is too large the constraint (2.38) is not fulfilled and the bright states get populated. Therefore, the transfer efficiency is maximum if the mixing angle reaches $\pi/4$ when the the rms Rabi frequency Ω_{eff} reaches its maximum value. In the case of Gaussian shaped laser beams, the optimum pulse delay is equal to the pulse width [54].

2.3.4 One and two-photon detuning line width

As the dark state does not depend on the one-photon detuning in case of an adiabatic transfer, the transfer efficiency is not influenced by it. However, the pulse areas are finite, which means that the limit beyond the adiabaticity has to be considered. And in this case, the transfer is not complete since the intermediate level gets populated in the process. As it will be seen in section 2.3.5 there are cases when a one-photon detuning is favorable, which creates the necessity of having a compromise between the minimization of the population in the intermediate level by increasing the one-photon detuning Δ and the maximization of the adiabaticity by decreasing it. For the case of $\Delta \neq 0$, the adiabacity condition[55] is given by:

$$|\dot{\Theta}| \ll \Omega_{eff} \frac{\sin\phi}{\cos^2\phi}. \tag{2.41}$$

Assuming that the pump and dump lasers have the same strength α, which is proportional to the pulse area $\Omega.\tau$, and $\beta \propto \Delta.\tau$, it is easy to realize that for an α that is sufficiently large the condition (2.41) is fulfilled. It is convenient to define $\beta_{1/2}$ as the detuning for which half of the population is transferred into the $|3\rangle$ state. In the case of a large fixed α ($\alpha \gg 1$), if $\beta_{1/2} \sim \alpha$ the adiabaticity condition is immediately fulfilled. However, if $\beta \gg \alpha \gg 1$, the right side of condition (2.41) can be replaced by $\frac{\alpha^2}{\beta}$ and then in order for the transfer to have a large efficiency $\alpha^2 \gg \beta$ and $\beta_{1/2} = c\alpha^2$. In [55] it was shown that for gaussian shaped pulses the proportionality constant c depends only on the pulse delay (t/τ) with a distorted gaussian dependance $c(t/\tau) = \frac{exp(-2t^2/\tau^2)}{a(t/\tau)}$. In general c depends on the pulse shape and on the pulse delay.

In [56], the dependance of the transfer efficiency on the two-photon detuning δ in the $\Omega_{eff} > |\delta|$ case was determined. It was deduced that for the following shape of pulses: $\Omega_P = \Omega_{eff} \sin\frac{\pi(t+\tau/2)}{2\tau}$ and $\Omega_D = \Omega_{eff} \cos\frac{\pi(t+\tau/2)}{2\tau}$, $-\tau/2 <$

$t < \tau/2$ the efficiency of the transfer is given by the exponential:

$$exp\left(-\frac{\gamma\tau\delta^2}{8\Omega_{eff}^2}\right), \quad \gamma\tau \gg 1, \tag{2.42}$$

for which the two photon full width at half maximum is $\delta_{FWHM} = \frac{4\sqrt{2\ln 2}\Omega_{eff}}{\sqrt{\gamma\tau}}$. In the case $\gamma\tau < 1$ this line width approaches $1.3\Omega_{eff}$ determined by the Landau-Zener transitions [57].

It was also found in [56] that generally the non-adiabacity causes a shift of the maximum of the transfer efficiency with respect to the one-photon detuning, being that maximum proportional to Δ up to the lowest of the two laser Rabi frequencies. When both Rabi frequencies are increased, that shift becomes smaller as a result of the more fulfillment of the adiabacity conditions.

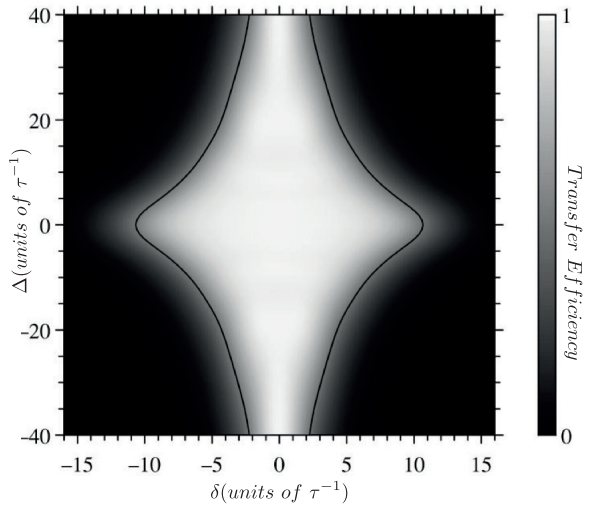

Figure 2.11: Numerical calculation of the transfer efficiency of STIRAP for gaussian shaped pulses with the one and two-photon detuning [58]

As it was seen, while the one-photon detuning transfer efficiency line width is proportional to the square of the Rabi frequency, the two-photon detuning has a transfer efficiency line width that grows linearly with it, which makes the transfer much more sensitive to the later one (see figure 2.11).

2.3.5 Effect of a decaying intermediate state

In [59] it was considered the decaying from the intermediate level to states other than $|1\rangle$ or $|3\rangle$ and vanishing two-photon detuning. For $\Delta = 0$, it was shown

that the transfer efficiency is given by:

$$\exp\left(-\frac{\pi^2\gamma}{2\Omega_{eff}^2\tau}\right) \text{ for } \Omega_{eff}^2\tau \gg \pi\gamma \tag{2.43}$$

. In this way the line width of the transfer efficiency scales with $\Omega_{eff}^2\tau$, like in the case of the one-photon detuning. It was also proven that for large enough $\Omega_{eff}\tau$ this value doesn't depend much on the one-photon detuning.

In the case the decaying rate or the one-photon detuning are too large, $\Omega_{eff}^2 \ll \sqrt{\Delta^2+\gamma^2}$, the transfer efficiency fades out with a lorentzian power law: $\frac{(\int \Omega_P\Omega_D dt)^2}{(\gamma^2+\Delta^2)\tau^2}$.

2.3.6 Effect of several intermediate levels on the transfer efficiency

As the hyperfine states are not known, also their energy spacing isn't but clearly several of this states take part in the transfer as intermediate levels. To assure the transfer efficiency is high enough, it is convenient to know how large the one-photon detuning should be, and where should be positioned: if resonant to one of the states, between them or above/below all of them.

In [60], this was thoroughly studied. The hamiltonian considered was (see figure 2.12):

$$\hat{H}(t) = \begin{bmatrix} 0 & \Omega_{P,1} & \cdots & \Omega_{P,N} & 0 \\ \Omega_{P,1} & \Delta_1 & \cdots & 0 & \Omega_{D,1} \\ \vdots & \vdots & \ddots & \vdots & \vdots \\ \Omega_{P,N} & 0 & \cdots & \Delta_N & \Omega_{D,N} \\ 0 & \Omega_{D,1} & \cdots & \Omega_{D,N} & 0 \end{bmatrix} \tag{2.44}$$

where Ψ_i and Ψ_f are on two-photon resonance and each intermediate state Ψ_k has a one-photon detuning Δ_k. The couplings between the intermediate states and the initial and final states, respectively, can be written as the following proportionality relations:

$$\Omega_{P,k}(t) = \alpha_k\Omega_P(t) \qquad \Omega_{D,k}(t) = \beta_k\Omega_D(t) \tag{2.45}$$

where α_k and β_k are the relative strengths of the coupling and are related to Clebsch-Gordan coefficients and Franck-Condon factors.

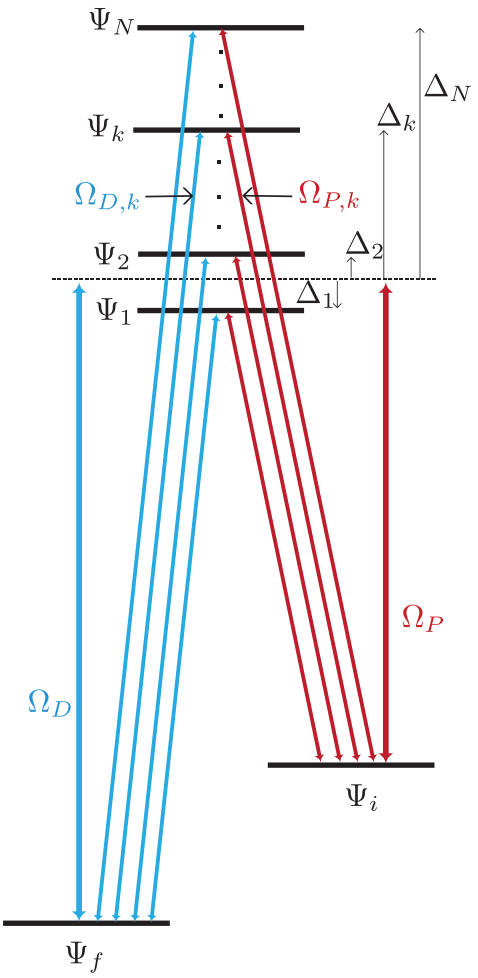

Figure 2.12: Scheme of the STIRAP with multiple intermediate states - the explanation of the notation used is in the text.

In the case there is an eigenvalue that is zero, a dark state exists only if the couplings are proportional: $\frac{\alpha_k}{\beta_k} = c$ for all k where c is a constant, independently of the one-photon resonance. In this situation the system behaves as the single Λ system in STIRAP. If this proportionality doesn't occur, there is no dark state. However, it may exist an adiabatic-transfer state (Ψ_{AT}) that couples the initial and final states. During the transfer Ψ_{AT} populates transiently the intermediate levels, which may decay and lead to a diminished transfer efficiency. If only one intermediate level is on resonance there is always a Ψ_{AT}; and if more than one state are on resonance, these have to fulfill the proportionality constraint for the state to exist. When the transfer is off-resonant the following condition must be obeyed for the existence of Ψ_{AT}:

$$S_{\alpha^2} S_{\beta^2} > 0 \quad \text{where} \quad S_{\alpha^2} = \sum_{k=1}^{N} \frac{\alpha_k^2}{\Delta_k} \quad \text{and} \quad S_{\beta^2} = \sum_{k=1}^{N} \frac{\beta_k^2}{\Delta_k}. \tag{2.46}$$

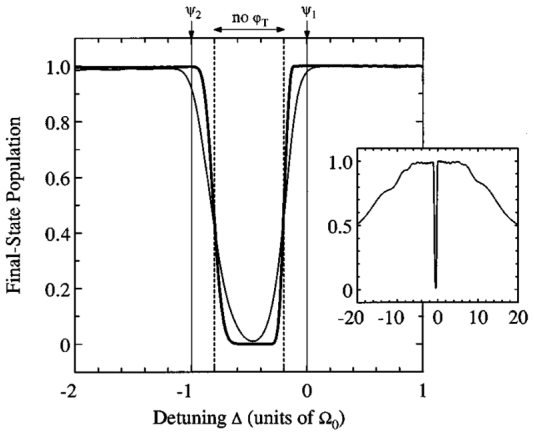

Figure 2.13: Population transferred to the final state as a function of the one-photon detuning when there are two intermediate levels represented by the vertical solid lines: Ψ_1 with $\Delta_1 = \Delta$ and Ψ_2 with $\Delta_2 = \Omega_0 + \Delta$. The region between the dashed lines is the one for which the condition (2.46) doesn't apply. The curve that is thiner has a pulse area of 20 whereas the thicker one has a 80 pulse area. The inset corresponds to the same variables but for a wider range of the detuning [60].

In figure 2.13 it is possible to observe that within the interval where condition (2.46) is not fulfilled, the population in the final state drops to zero, as it was expected. Therefore, the one-photon detuning should be large. However, if this is too large, as it is possible to observe in the inset, the efficiency decreases, as it was already shown in 2.3.4, since the adiabacity condition weakens.

The figure 2.14, in which five intermediate states were considered, illustrates that, when the pump and dump laser frequencies are swept across the intermediate states' energies, frequencies where $S_{\alpha 2} S_{\beta 2} = 0$ are crossed. The system passes from detunings for which the final population is maximum (that correspond to the frequencies of the intermediate states) to those for which is zero (frequencies between intermediate states). Like that, it is not known *a priori* if the transfer will be efficient or not. With this in mind, it is preferable to detune the laser frequencies just above or below all the intermediate states, as there Ψ_{AT} always exists. Also, it is possible to notice in both figures 2.13 and 2.14 that in this large Δ region the adiabaticity is easier to reach and that the scheme is more robust against laser intensity variations. Besides all that, in this paper [60] it was also shown that the population in the intermediate states scales with Δ_k^{-2} and therefore the larger the detuning, the lesser the population in this states and the drop in efficiency.

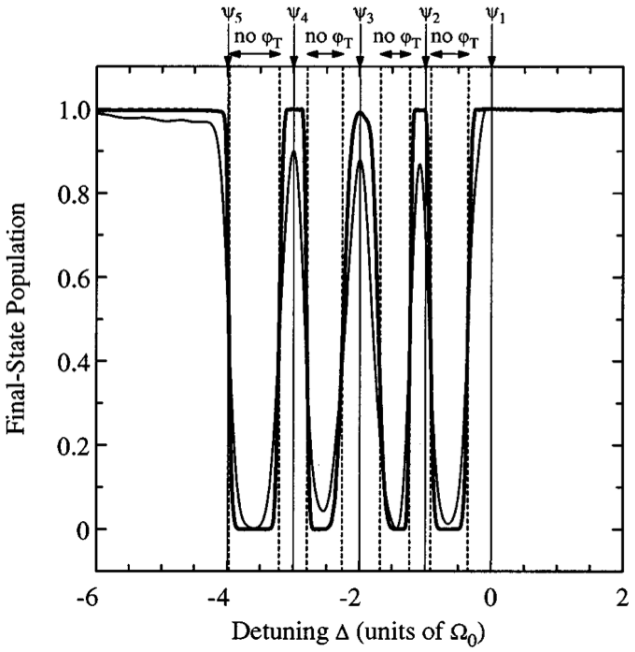

Figure 2.14: Population transferred to the final state as a function of the one-photon detuning when there are five intermediate levels: Ψ_k with $\Delta_k = (k-1)\Omega_0 + \Delta$, $k = 1,2,3,4,5$. The coupling strength α_k and β_k are random. The curve that is thiner has a pulse area of 20 whereas the thicker one has a 80 pulse area. The inset corresponds to the same variables but for a wider range of the detuning [60].

2.3.7 Effect of noise on the transfer efficiency

The STIRAP scheme is very sensitive to the frequency and if the fields have a phase that varies in time, there will occur variations in the frequency that affect the transfer efficiency.

In [61] it was studied how the phase noise influences the transfer. Although several kinds of correlations between the lasers were considered, only the uncorrelated fields is of interest for this experiment. Since, although both frequencies are locked to the same cavity, in the time scale of the transfer there is no correlation between them. Therefore, only noise due to the locking electronics have to be considered, and the laser beams can be regarded as independent on from the other. It was considered that the electric fields of the pump and dump laser pulses have phases with stochastic time-derivatives ($\dot{\phi}_j(t) = \xi(t)$, $j = D, P$) and therefore, correspond to noise sources. The correlation between the lasers is parametrized by T: $\xi_D(t) = \xi_P(t+T)$, and for the uncorrelated case this time delay T has to be large in comparison to the duration of the atom-field interaction and to the correlation time of the noise. The inverse of the auto-correlation

time is G and D is the phase diffusion coefficient. Considering white noise, $G \gg D$ and D corresponds to its amplitude. It is shown in figure 2.15 that, for uncorrelated fields, as D gets larger, the pulse area also has to increase for the same transfer efficiency to be achieved. This is what was expected, since adding more noise to both fields makes the two-photon detuning non-zero and as it was seen in 2.3.4 the efficiency is very sensitive with this detuning. The total efficiency is given by the product of the efficiency considering no noise with the efficiency considering only the noise. The former one was already studied in the previous subchapters, while the latter was demonstrated to have the following expression for cosine pulses:

$$P^{(\xi)} = \exp\left(-\frac{DG\tau(2G+\gamma)}{4G^2+2G\gamma+\Omega_0^2}\right) \tag{2.47}$$

which in the case of white noise ($G \longrightarrow \infty$) has the form:

$$P^{(\xi)} = exp\left(-\frac{D\tau}{2}\right) \tag{2.48}$$

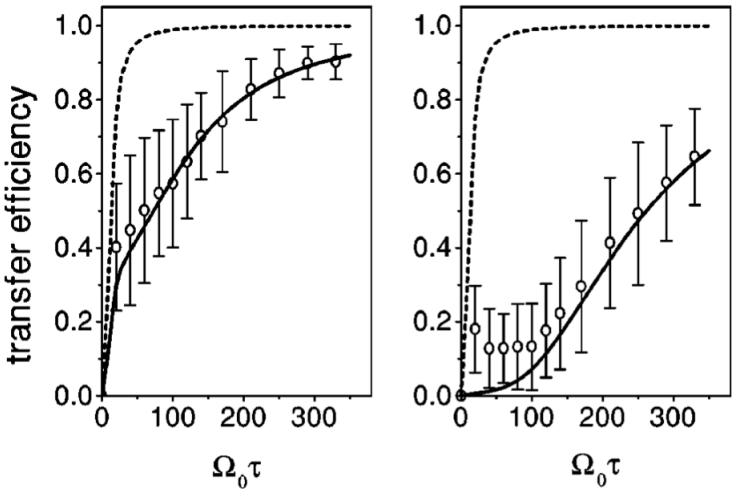

Figure 2.15: Population transferred to the final state as a function the pulse area with vanishing one and two photon detuning for independent fields. In the left $D\tau = 2$ and in the right $D\tau = 10$, while for both $G\tau = 50$. The circles represent Monte Carlo simulation, the solid line represents the theory and in the dashed one the noise is not considered[61].

Like this, in order for the population transfer be high, $D\tau \ll 1$, where D is equivalent to the laser's bandwidth, which has a large contribution given by the Shawlow-Townes noise. This is the fundamental limit of of the efficiency of the transfer which will always exist, which means it doesn't improve with an

increase in the pulse area (which is not true for a finite correlation time).

2.3.8 States for realization of STIRAP

The initial Feshbach molecular state accessible with reasonable magnetic fields lies in the $a^3\Sigma^+$ $v = 19$ manifold. In particular, a very broad resonance at 139.7G [62] between the states $|1,1\rangle_{Na}$ and $|9/2,-5/2\rangle_K$ exists. This weakly bound state corresponds to the initial state $|1\rangle$ of the STIRAP scheme.

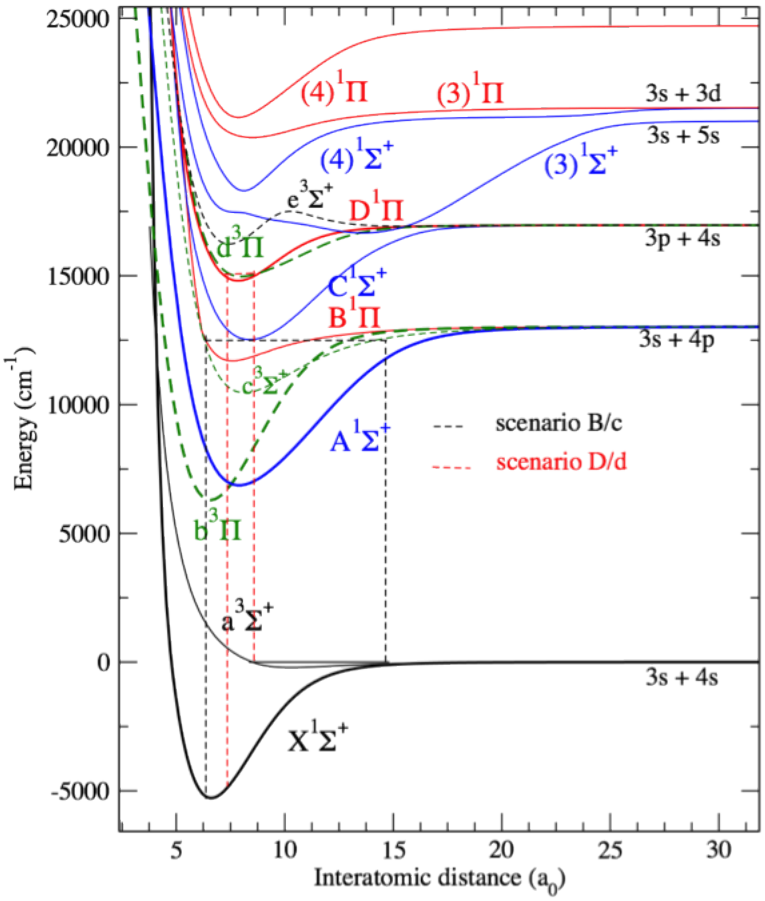

Figure 2.16: NaK molecular potentials [63, 64] where two scenarios where considered: one in which the intermediate level is the superposition of the state B with c and another where it is the superposition of the D state and d - the latter proposal is the chosen one.

The target state is the rovibrational ground state $X^1\Sigma^+$ $v = 0$ $J = 0$. Therefore, the intermediate level has to be chosen according to the transition dipole moments (TDM) with both initial and final states. Furthermore, the frequency difference with each of them should allow the usage of suitable laser frequencies which are easily achieved.

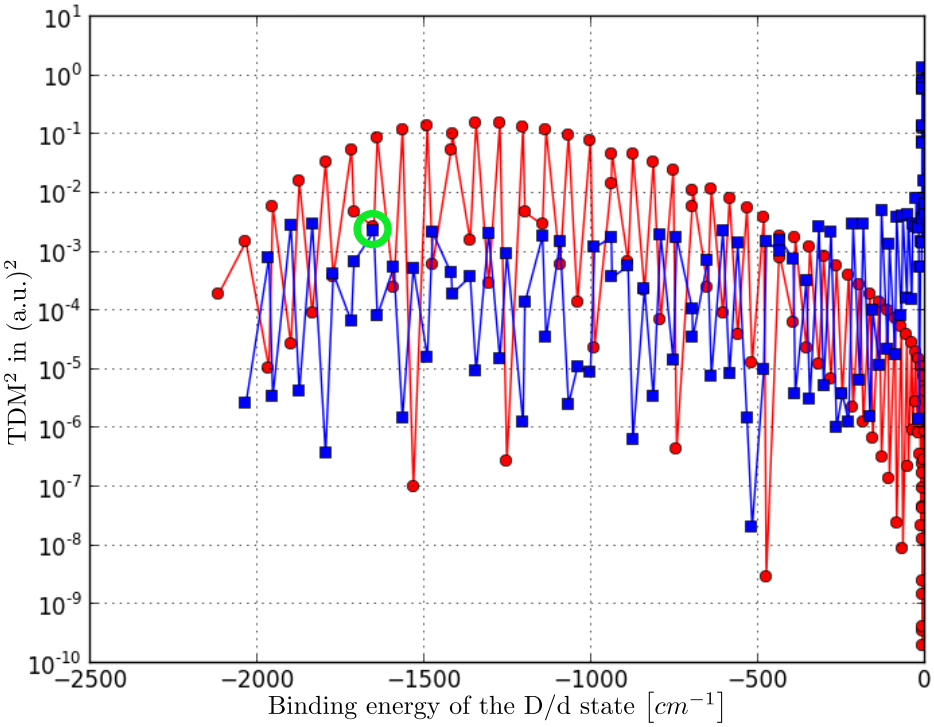

Figure 2.17: Square of the transition dipole moment of the $Na^{40}K$ from the initial state a($v = 19$) to the intermediate state D/d - red - and from D/d to the ground state X ($v = 0$)- blue. It is possible to see that for a binding energy of -1700cm^{-1} the TDM for the triple character of the $a \rightarrow D/d$ has the same order of magnitude of the TDM of the singlet character of the $D/d \rightarrow$ X, making the D/d a suitable state for being the intermediate level [N.Bouloufa, O. Dulieu et al, private communication].

Something one has to have in mind is that the initial state is a triplet ($\Sigma = 1$) and the final state is a singlet ($\Sigma = 0$) and, as it was discussed in the section 2.1.4, by the electric dipole selection rules $\Delta\Sigma = 1$ is forbidden. In the Born-Oppenheimer potentials the kinetic energy and the spin-orbit effect are not considered, however if the latter is calculated, the coupling of the singlet and triplet states is observed. In this case the Franck-Condon factors, depending on the binding energy of the intermediate state, show the singlet or the triplet character. Therefore, the intermediate level has to have a double character. Two scenarios were considered: one in which the intermediate level is D/d and another in which is B/c. In both the TDM is large enough for the transfer - on the order of 3×10^{-2}a.u. (for the D/d scenario see figure 2.17) - and is similar for the initial and the final states. This is convenient since otherwise, the Rabi frequency had to compensate this effect and, as it scales with the square of the intensity of the laser, one laser had to be much more powerful than the other. The D/d state was chosen as the intermediate level because the laser frequencies needed in this

case were more suitable than in the other case. The frequency for the pump laser was calculated to be 652.654(8)nm and for the dump laser 486.995(5)nm.

2.3.9 Adiabacity conditions in our setup

All the adiabacity conditions that were discussed in the previous sections have to be fulfilled in our setup. We have approximately 10mW of optical power available for each frequency which will be focused to an area of $\approx (100\mu m)^2$. With this intensity, it is possible to calculate a minimum transfer time to get high transfer efficiency.

The individual Rabi frequencies were calculated to be 11,1MHz which corresponds to a $\Omega_{eff} = 15.7MHz$, in which the transition dipole moments used were 0,03 a.u. (as it can be seen in figure 2.17).

The line width of the intermediate level was calculated to be 8,5MHz and its radiative lifetime 18ns. This is a rough estimate as only the triplet state (which has larger Franck-Condon factors and therefore is more likely to be populated) was considered and a geometrical factor is missing in this calculation.

As it was seen in section 2.3.2, the general rule (2.40) (in which only the Rabi frequency is taken into account) determines a minimal transfer time on the order of a few μs.

In section 2.3.5, it was referred that when there are many intermediate hyperfine levels, as in our case the ideal solution is to set the one-photon detuning to either above or below all states. In our case, it should be around 10 MHz detuned from the furthest level (since the line width is 8.5MHz). For this case, as discussed is section 2.3.4 the adiabacity condition (2.41) is immediately fulfilled, whereas if this Δ is increased the efficiency starts to drop.

In this way, if a transfer time of 1ms is chosen, the two-photon line width is 313kHz according to (2.42) and the transfer efficiency due to the decaying intermediate state is 0.9989 (2.43).

3 Laser System

In the STIRAP scheme, the adiabacity condition, which assures a complete transfer between states, demands that either the Rabi frequencies or the transfer time (or both) are very large. However, it is not always easy or affordable to get lasers with a high power for the desired wavelengths and also, a too high intensity may cause higher order effects and allow transitions to states forbidden by electric dipole selection rules. Therefore, it is desirable to increase the time of the transfer. As it was shown in the last chapter, the STIRAP scheme is very susceptible to the coherence in time between the two lasers frequencies, since during the transfer the two-photon resonant condition has to be maintained. But the noise caused by changes in the phase of the electric field can degrade the dark state and populate the lossy one. Therefore, long coherence times in the cross-correlation between the lasers are difficult to achieve and a compromise between the power of the laser beams and the time of the transfer has to be made. Furthermore, long-term stability is also desirable, to be able to reproduce the experiment without having to scan the Raman lasers constantly. The setup implemented will allow the required narrow line width for both laser beams and a high control over them, in a relatively simple and effective way.

Another aspect to take into account is the tunability of the lasers: as we only know the values for the wavelengths up to a few pm, we will need to be able to sweep our lasers (not necessarily continuously) about tens or hundreds of GHz to find the right intermediate state. Additionally, the lasers should have a large mode-hop-free tuning (of a few GHz) during which the line width is narrow and there is no necessity to re-lock the laser.

The setup, as shown in figure 3.1, consists of four lasers: two for each frequency. The scheme is equal for both frequencies, and therefore, the summary will only describe one.

One of the lasers is locked using the Pound-Drever-Hall technique to a reference cavity which is made of an ultra low expansion glass (ULE®) to minimize thermal drifts. This laser is called *master* laser and is locked at a frequency

that corresponds to a resonance of the cavity that is a Fabry-Pérot with a free-spectral range of 3GHz. The other laser, which we call *slave* laser, is made to have a beat signal with the stabilized *master* laser beam. This signal is afterwards mixed with another one coming from a signal generator. The output of the mixer is then sent into a servo that will regulate the slave laser's parameters injection current and piezo-transducer (PZT). In this way it is possible to control the laser frequency that will go to the experiment by controlling the signal generator. Both *master* lasers are locked to the same cavity, with mirrors coated for both frequencies. This allows the reduction of noise in the two-photon line width that comes from mechanical stability of the cavity, since if there is a length change ΔL of the cavity, the frequency of the lasers will change in a correlated way: $\frac{\Delta L}{L} = -\frac{\Delta f}{f} \Longrightarrow \Delta f_{red} = \frac{f_{red}}{f_{blue}} \Delta f_{blue}$, where L is the length of the cavity, f_{blue} and f_{red} are the frequencies of the blue and red lasers locked to the cavity with respective changes Δf_{blue} and Δf_{red}.

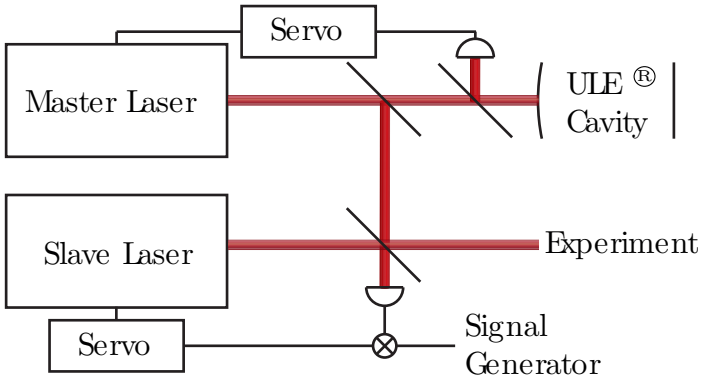

Figure 3.1: Simplified scheme of the setup used for the stabilization of one of the STIRAP laser frequencies and narrowing of the line width.

3.1 External cavity diode lasers

For the STIRAP setup, the laser diodes chosen have wavelengths of 652nm (SAL 1850-30, Sacher Lasertechnik) and 488nm (LD-0488-0150, Toptica). The frequencies that this kind of laser emit depend essentially on the material they are made of.

Typically this kind of diodes have a line width of several tens of MHz because the two facets of the diode are very close to each other and act as a Fabry-Pérot with very low Q [65], where the spontaneous emission amplified in the gain medium plays a big role for the line width. Therefore, it is desirable to reduce

the line width. That can be done if Q gets larger by extending the Fabry-Pérot externally - these are the external cavity diode lasers (ECDL) [66].

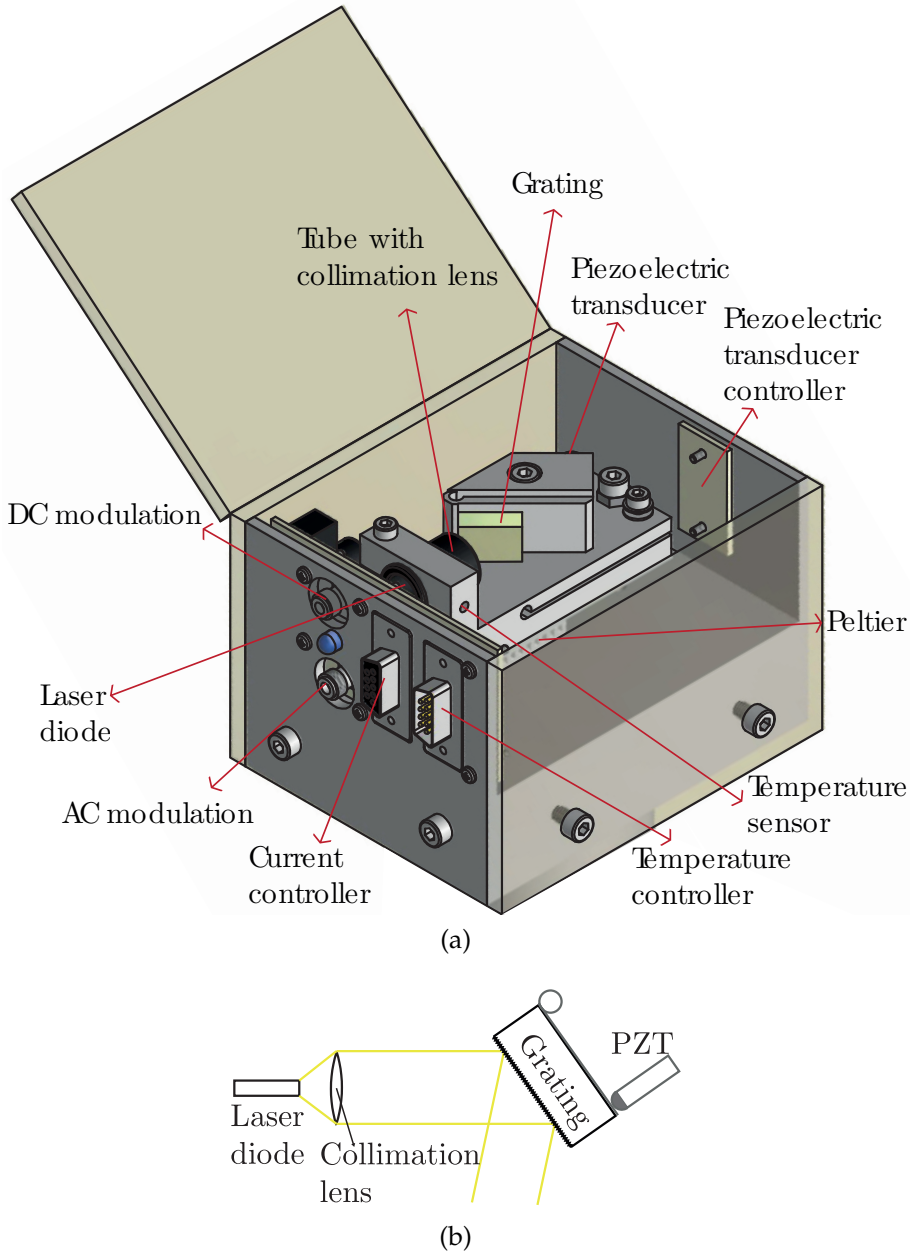

Figure 3.2: a) Rendering of a typical Littrow type diode lasers head as used in my setup and b) simplified scheme the Littrow configuration.

As typically the laser output facet is rectangular $(1\mu m \times (1-100)\mu m)$, elliptical beams are created [67], which demands the use of anamorphic prism pairs to make the shape of the beam the roundest possible, so the coupling with the fibers is maximal. The fact that usually the size of these diodes is very small and comparable to the wavelength of the emitted light causes strong diffraction

and large divergence of the beam, which requires the use of a collimation lens. This lens can also be used reversely (as its focal point is in the diode) to send optical feedback into the laser diode. If this feedback has a narrow line width, the lasing will occur only at that frequency. The Littrow configuration for an external cavity diode laser [68] consists of a grating that reflects back the first order of the diffracted beam, being this the necessary optical feedback for the lasing (figure 3.2). The wavelength can then be tuned by changing slightly the angle of the grating. This technique allows to narrow the line width in a single mode operation. The piezoelectric transducer (PZT), that regulates the angle of the grating, allows to tune the frequency in a large range, however, as the grating is bulky, this takes time to act and therefore the changes in frequency are slower than the noise of the setup. In this way, the PZT only maintains the peak at a certain frequency and doesn't diminish the line width of the laser. Thus, it is desirable to have a way of changing the laser frequency fast enough to reduce the noise, which can be done by varying the laser's current, enabling tuning over a smaller range than the PZT.

In the figure 3.2, the rendering of the laser head used in my setup can be seen. The laser diode is connected to a circuit board which permits its good protection (as an electrostatic discharge may destroy it) and alternating and direct current modulation. As the alternating current doesn't allow to modulate around 0V to have zero injection current, only the direct current modulation will be used in our scheme. This modulation will allow to achieve the desired one-photon detuning and the Raman resonant condition, as by varying the current, the frequency changes accordingly.

3.2 Reference cavity and vacuum chamber

The cavity (ATF-6301, *Advanced Thin Films*) with the gaussian modes to which the *master* lasers will be locked to, is made of an ultralow-expansion glass (ULE®, *Corning*) which is a titania-doped silicate glass that suppresses the linear coefficient of thermal expansion ($\alpha_{ULE} = \frac{1}{L}\frac{dL}{dT}$) at a particular temperature T_C (typically at around the room temperature). This fact validates the Taylor expansion around that temperature: $\alpha_{ULE} = \alpha(T - T_c) + \beta(T - T_c)^2$. The relative frequency change has therefore the following dependance with temperature:

$$\frac{\Delta f}{f} = -\frac{\Delta L}{L} \approx -\frac{\alpha}{2}(T - T_C)^2 - \frac{\beta}{3}(T - T_C)^3 \tag{3.1}$$

in which T is the temperature of the Fabry-Pérot cavity and L is its length. This allows a minimization of the drift due to temperature if the cavity is placed in a temperature controlled and stabilized environment at T_C, since the length of the ULE® spacer has a minimum for this temperature.

Due to the finite temperature of the materials there will always exist thermal motion and it was calculated that most (84%) of the thermal noise of the cavity associated to that motion had its origin in the mirrors substrates [69]. Furthermore, it was shown that, if the ULE® mirrors were replaced by fused silica ones optically contacted to the ULE® spacer, the thermal noise would be reduced by a factor of three[70]. The mirrors have, in this way, low thermal and mechanical noise at room temperature, but have large coefficient of thermal expansion (CTE). This mismatch of CTE causes the bending of the mirrors which results typically in a zero crossing temperature for the assembly below 0°C. This temperature is too low, since the further away from room temperature, the harder it gets to stabilize the cavity's temperature without creating temperature gradients in it. It was shown [71] that ULE® rings optically contacted to the back surface of the FS mirrors reduce the mirror bending without affecting the thermal noise and allow higher zero crossing temperatures, closer to the desired room temperature.

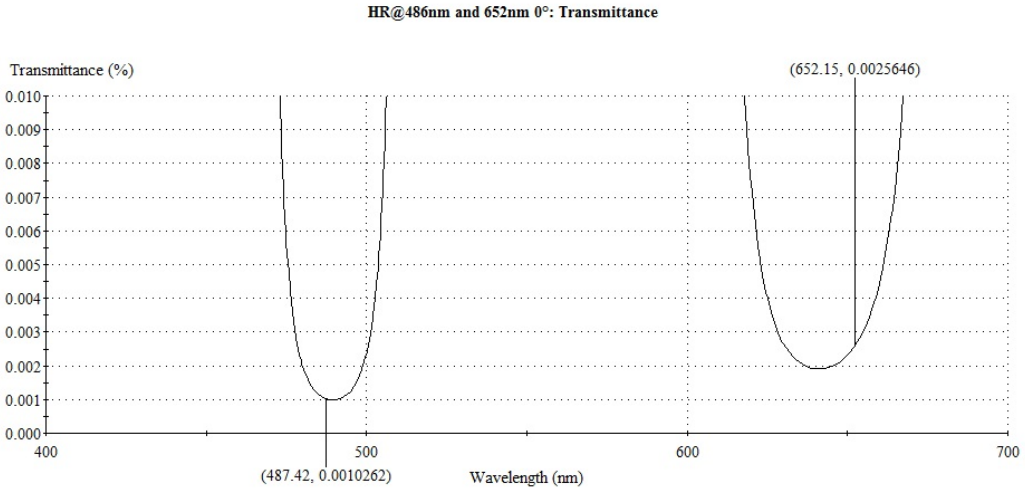

Figure 3.3: Numerical calculation for the transmittance of the inner substrate as a function of the wavelength for the coating for 487nm and for the one with 652nm (data calculated by the manufacturer Advanced Thin Films).

The specifications of the fused silica mirrors are: a diameter of 0.5" and a thickness of 0.165". Its inner surface substrate has a scratch-dig parameter of 10-5 with a transmission of 10-50 ppm with a finesse of $\mathcal{F} = \frac{FSR}{\delta_{cav}} > 30000$,

where δ_{cav} in the line width of the cavity resonance and FSR is the free-spectral range given by $\frac{c}{2L}$. The outer surface substrate has a scratch-dig of 20-10 and a reflectivity below 0.15%.

Furthermore, as mechanical vibrations are a serious problem for short-term length stability since they constitute the majority of the noise at low frequencies, it is desirable to have the cavity mounted in such a way that the coupling between the cavity length and the mount is minimized. With that in mind, a spherical geometry for the spacer [72] was developed, making the cavity insensitive to vibrations and orientation due to its high symmetry. The maximum relative variation of the cavity's length with acceleration for this geometry was reported to be $3 \times 10^{-10}/g$. Also, the angle (squeeze insensitive angle) at which the length of the optical axis is insensitive to squeezing forces was calculated (37.31° with respect to the normal of the optical axis), which corresponds to the angle of the fork-shaped support of the cavity. The yoke screws used to hold the cavity (and that were screwed by hand until the cavity didn't move anymore) are placed along the diameter of the cavity and assure a rigid mount of the it.

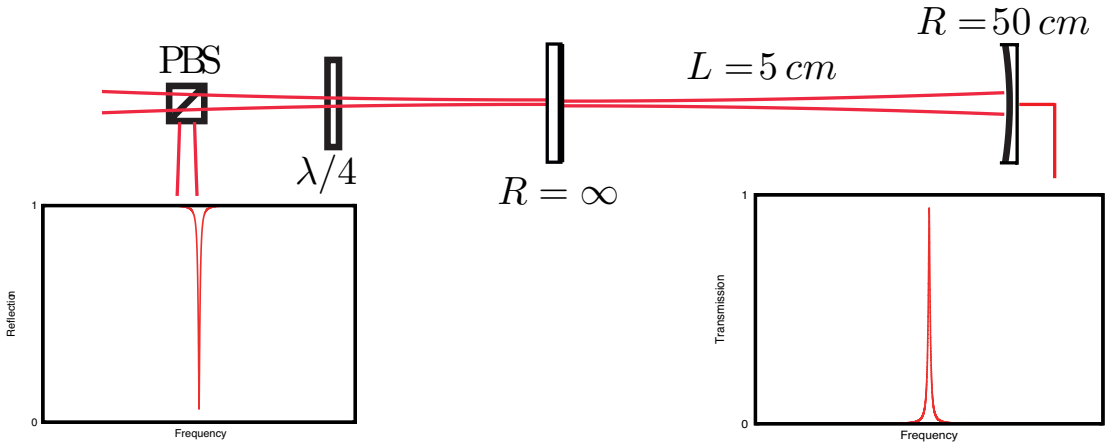

Figure 3.4: Scheme of the half-symmetric resonator when the laser light is on frequency with a TEM_{00} mode with respective transmission peak and reflection drop.

The *master* lasers are locked to the gaussian modes (TEM_{00}) of the cavity. The optical resonator (see figure 3.4) consists of two highly reflective mirrors separated by a spacer with length L. This kind of resonator is a Fabry-Pérot interferometer for which the transmission is ideally one (in case of no losses and of a gaussian beam) when the incident laser has a frequency equal to one of the evenly spaced resonances of the cavity (separated by a free-spectral range $FSR = c/2L$). A parameter called finesse measures the ratio between the sepa-

ration between these resonances and their line width ($\mathcal{F} = \frac{FSR}{\delta_{cav}}$). As the beam in never truly gaussian (TEM_{00}), there are also other cavity resonances: the transverse electromagnetic (TEM) modes. Also for these modes there are transmission peaks if they overlap with the driving field.

The spacer has a length of $L = 5$cm (free spectral range of $\frac{c}{2L} \approx 3$GHz), one of its mirrors is flat and the other has a radius of curvature of $R = 50$cm. This means that the cavity is a half symmetric resonator with a gaussian mode waist [73] of:

$$\omega_0^2 = \frac{\sqrt{L}\lambda}{\pi}\sqrt{R-L} \tag{3.2}$$

located at the flat mirror, which has the value of 0.15mm for the blue laser and 0.18mm for the red. It is necessary that the other modes have frequencies sufficiently far away from the chosen TEM_{00} mode, since otherwise, the lock frequency can get shifted. For the particular case of a half-symmetric resonator [73], these are:

$$f_{qnm} = \frac{c}{2L}\left[q + (n+m+1)\frac{\text{atan}\left(\frac{1}{\sqrt{L.(R-L)}}\right)}{\pi}\right] \tag{3.3}$$

where q corresponds to the order of the longitudinal modes and m and n to the order of the TEM ones. The separation in frequency of the longitudinal modes is 3GHz and for consecutive transversal modes is 1.36GHz.

It is possible to observe in figure 3.5 that there aren't transversal modes in the vicinity of the TEM_{00} that could interfere with the locking. For the calculation of the modes' frequency, only the modes which have $m, n \leq 3$ were considered, because the beam is close enough to a gaussian making the higher order TEM modes' field amplitude very small, as it is shown in section 4.3.

The cavity is placed inside a vacuum chamber (vacuum housing 6300, *Stable Laser Systems*) to avoid air pressure variations that cause changes in the refractive index leading to a time-varying shifted cavity mode resonance. The vacuum is also important for acoustic and temperature isolation. Furthermore, as at the temperature T_C water condensation already occurs, if the water molecules are not removed, the lock is unfeasible. This vacuum housing is made of stainless steel and it has one thermal shield which at the bottom has two thermistors and a peltier, these are used to temperature stabilize the cavity (see figure 3.6a).

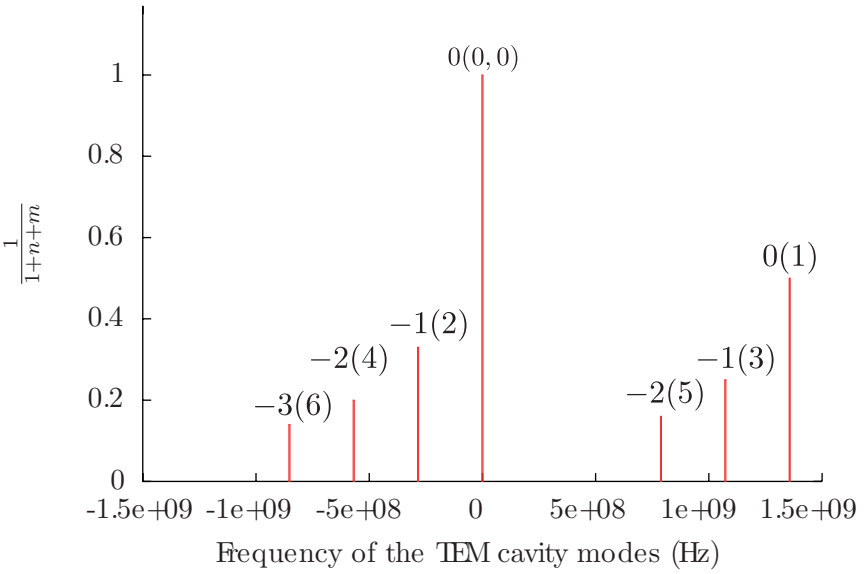

Figure 3.5: Frequency of the transverse electromagnetic modes (TEM) within the free-spectral range around TEM_{00}. The y-axis corresponds to $1/(n+m+1)$. It is possible to observe degeneracies that correspond to modes with the same $(n+m)$ which are represented by $q(n+m)$ on top of every mode frequency. This data was calculated assuming the specifications of the cavity used in this experiment: $R = 0.5$m and $L = 0.05$m.

However, as the cavity is only being supported in two points by the screws (see figure 3.6b), it will thermalize radiatively, which takes several hours. Under the cavity there is a metallic block that works as a heat sink. The electronic feedthrough for the thermistors and peltier is made by means of a 9-pin D-sub connector.

During the process of mounting the cavity inside the housing, it was taken care that the orientation of the radiative shield matches the one of the cavity in order to have a good optical access through the two windows (see figure 3.6c). These windows are slightly tilted with respect to the optical axis to avoid back reflections that may constitute additional unwanted interferometers. At the top of the chamber there is a CF 16 tee flange to which a corner valve and an ion pump are connected. Initially, through the valve, a turbo-molecular pump was attached, which kept the pressure below 5×10^{-10}mBar after a bake-out at 80°C during several days to take the water vapor out. After that time, the valve was closed, the turbo-molecular pump was removed and the 2l/s ion pump took over, maintaining a pressure $< 10^{-8}$mBar (it is not possible to measure it as no pressure gauge was installed). Without the ion pump, the pressure would increase due to outgassing and small leakages.

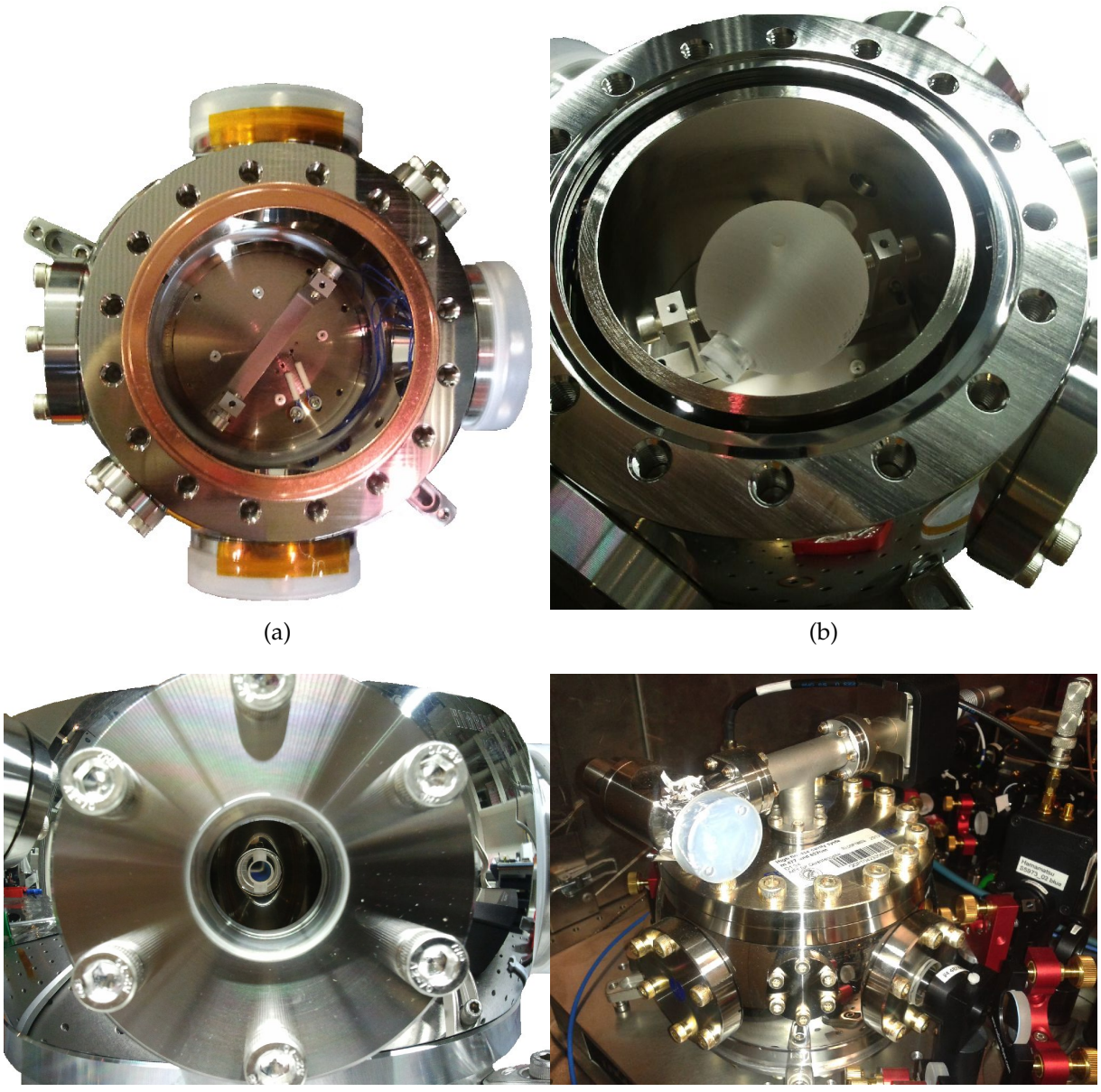

(a) (b)

(c) (d)

Figure 3.6: In (a) the thermistors at the base of the thermal shield and the fork-shaped support for the cavity can be seen. In (b) the spherical cavity is already assembled supported by two silver soft screws. In (c) it is possible to see the good optical access of the cavity through the windows. In (d) the cavity is already in vacuum with the tee flange connected to a corner valve and to the 2l ion pump.

3.3 Feedback systems

As the peak frequency of the lasers must be very stable for the STIRAP to occur with high efficiency, they have to be locked to a reference, in this case, to the

TEM_{00} modes of the optical resonator. The locking also allows to reduce the line width of the lasers. For the lock, a feedback loop with a servo system must be implemented, which requires some knowledge on feedback systems (for a brief review see [74]).

The servo has the function of maintaining the laser frequency at the same value of the reference. The loop (see figure 3.7) consists of detecting the laser light and comparing the frequency of the laser with a frequency reference. This frequency difference has to be converted into a voltage so the electronics that constitute the servo can amplify this signal and feed it back to the laser, adjusting its frequency through the injection current and the PZT angle, and in this way closing the loop. The PZT is used mainly to avoid slow frequency drifts, while the main responsible for the line width reduction is the current adjustment.

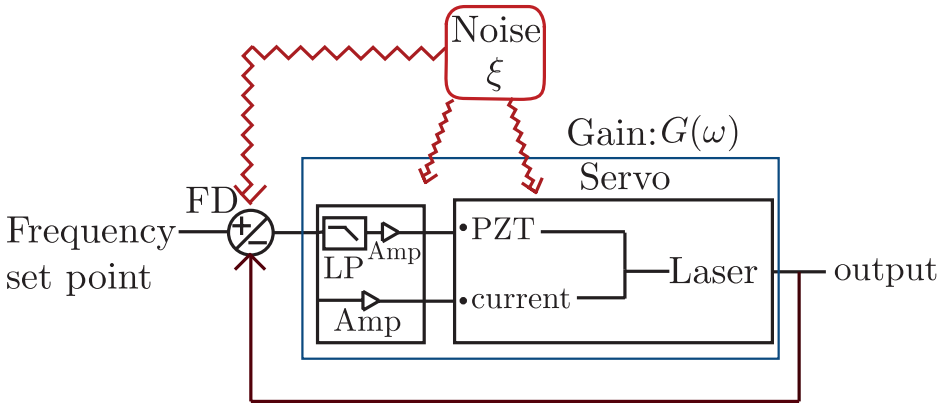

Figure 3.7: Scheme of a feedback loop with open-loop gain in the Fourier domain $G(\omega)$: the laser output is compared with a frequency set point in the frequency discriminator (FD) which also sums up all the noise ($\xi(\omega)$) that can be introduced in any part of the loop - from vibrations to electronic technical noise. This frequency discriminator in the diagram is also interpreted as a converter of the difference between the laser and set point frequencies into a voltage that is amplified by the servo and feed to the laser to alter its frequency accordingly.

It is easy to calculate that the closed-loop gain is given by $\frac{output(\omega)}{input(\omega)} = \frac{G(\omega)}{1+G(\omega)}$, which is the gain that keeps the laser locked to the set point even if this frequency changes during time. Noise is introduced in every component of the feedback loop and the frequency discriminator acts as a summation junction of all that noise ξ. At the output of the laser the noise is ξ', corresponding to a noise suppression given by $\frac{\xi'}{\xi} = \frac{1}{1+G(\omega))}$. Both to keep the laser at the same frequency of the frequency set point and to suppress the noise is desirable a large gain. By only taking into account these arguments, to have a narrow line width the gain should be infinite

However, it is needed to emphasize that this gain is complex and therefore, as every component adds a phase shift in the signal, at a frequency sufficiently high, due to delays the phase is shifted by 180°. In this way, the feedback will be positive, enhancing every deviation from the reference frequency, making the system start to oscillate. To avoid this phenomenon the gain has to be smaller than 1 (or 0dB) at the frequency where the phase is shifted by 180°. The frequency at which the gain is unity is called bandwidth and the phase stability margin measures how far the phase is from 180° when the gain drops below 0dB.

After this considerations, it is clear that the loop must be kept stable (gain below unity when phase is shifted 180°) while made as large as possible. Furthermore, the bandwidth should be much larger than the frequencies at which most of the noise occur, which because of vibrations is at hundreds of Hz. The Bode magnitude plot should have a negative slope with higher slope for lower frequencies.

3.4 Pound-Drever-Hall frequency lock

In this scheme [75, 76], laser light is sent into a Fabry-Pérot cavity and, the reflected light from it, is used to measure the laser's frequency. The reflectivity drop at a cavity resonance allows the implementation of the Pound-Drever-Hall lock. The reflected field is the sum of both the prompt and the leakage fields, being the prompt field the one immediately reflected from the first mirror of the cavity (without ever entering it) and the leakage field, the part that leaks from the cavity's standing wave through the first mirror. As, at resonance, these fields have the same amplitude and are completely out of phase, their sum is zero (see figure 3.8). However, since the slope at the resonance is zero, a small change in frequency produces no intensity changes. It is now worth mentioning that the line shape intensity derivative (in frequency) has a finite slope around the resonance which can be used to lock the laser, furthermore, it is zero at resonance, meaning that it is not affected by laser power or other variables. If the laser frequency is slightly dithered and the phase variation of the reflected light with respect to the incident one is observed, it is possible to know the side of the resonance in which the laser's frequency is (as it changes from -180° to 180° by crossing the resonance - see figure 3.8) and make the necessary adjustments to make it resonant once again.

To modulate the frequency of the laser, an electro-optic modulator (EOM -

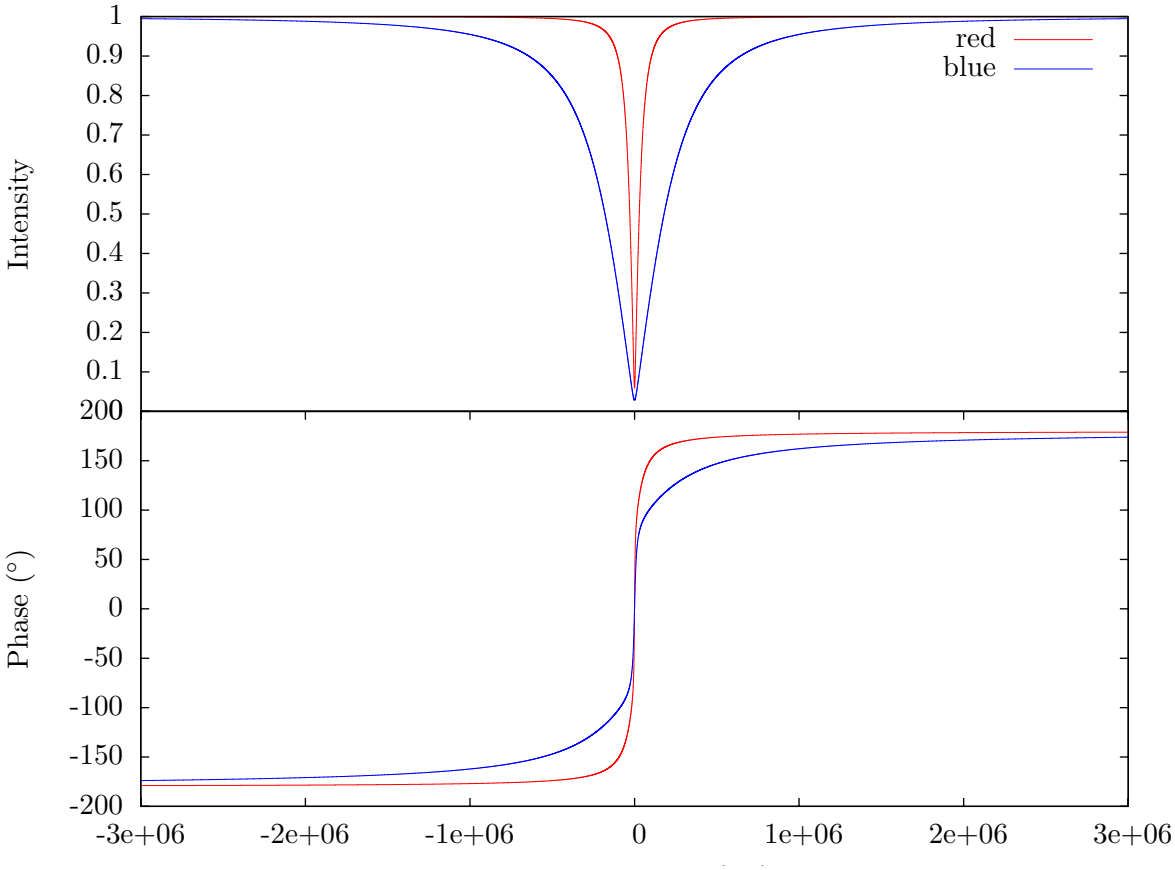

Figure 3.8: Reflection intensity and phase with respect to the incident field at a resonance of the optical resonator - it is possible to observe the drop to zero of the reflectance and the discontinuity of the phase - for the red laser the finesse is 188000 and for the blue 30000 with a $FSR = 3$ GHz.

see appendix 5) driven by a signal generator is used. This modulates the phase:

$$E_{inc} = E_0 e^{i[\omega t + \beta \sin(\alpha t)]} \tag{3.4}$$

where ω is the frequency of the laser light, β is the modulation depth and α is the modulation frequency. This phase modulation is expressed as a frequency modulation: $\omega' = \omega + \beta\alpha\cos(\alpha t)$.

By expanding (3.4) using Bessel functions and assuming a small β it is straightforward to reach an expression for the incident field:

$$E_{inc} = E_0 \left[J_0(\beta) e^{i\omega t} + J_1(\beta) e^{i(\omega+\alpha)t} - J_1(\beta) e^{i(\omega-\alpha)t} \right] \tag{3.5}$$

where it is clear that three frequencies are sent into the cavity: the carrier at the laser frequency (with power $|E_0|^2 J_0^2(\beta) = P_0 J_0^2(\beta)$) and two sidebands which

have frequencies $\omega \pm \alpha$ (each with a power of $P_0 J_1^2(\beta)$).

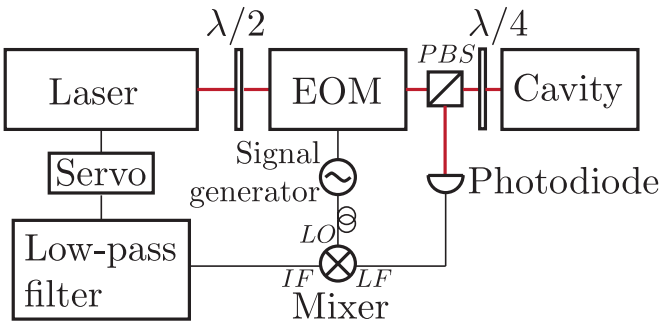

Figure 3.9: Scheme of the Pound-Drever-Hall lock: the laser light (with frequency ω) gets rotated by the half-wave plate ($\lambda/2$) and, by passing through the EOM driven by a signal generator, two sidebands with frequencies $\omega \pm \alpha$ are created. The light goes to the cavity where part is promptly reflected and the other builds a field inside the cavity if its frequency is correspondent to one of the cavity's resonances. The resultant reflected light is a superposition of the promptly reflected beams and the part that leaks out of the cavity. After being separated from the incident beams by a quarter-wave plate ($\lambda/4$) and a polarizing beamsplitter (PBS), an electronic signal is created when it is focused into the photodiode. This signal is demodulated by a mixer with respect to the frequency of the sidebands by phase-shifting the signal that comes from the signal generator to assure the same phase delay in both paths. The resultant IF signal is low-pass filtered and the DC signal kept is the error signal that is used by the servo to feedback to the laser and hold it on resonance with the cavity.

A photodiode is used to measure the reflected light intensity, making desirable to know its power dependance with the modulation frequency. After some calculations, the following expression is reached:

$$\begin{aligned} P_{ref} = P_0 \Big\{ & J_0^2(\beta)|F(\omega)|^2 + J_1^2(\beta)\left[|F(\omega+\alpha)|^2 + |F(\omega-\alpha)|^2\right] \\ & + 2J_0(\beta)J_1(\beta)\{\Re\left[F(\omega)F^*(\omega+\alpha) - F^*(\omega)F(\omega-\alpha)\right]\cos\alpha t \\ & + \Im\left[F(\omega)F^*(\omega+\alpha) - F^*(\omega)F(\omega-\alpha)\right]\sin\alpha t\}\Big\} \qquad (3.6) \\ & + (2\alpha \text{ terms}) \qquad (3.7) \end{aligned}$$

where $F(\omega)$ corresponds to the reflection coefficient given by the ratio between the reflected and the incident fields for a symmetric cavity with no losses:

$$F(\omega) = \frac{r\left[\exp\left(i\frac{\omega}{FSR}\right) - 1\right]}{1 - r^2\exp\left(i\frac{\omega}{FSR}\right)} \qquad (3.8)$$

with r being the magnitude of the reflection coefficient of the mirrors.

To the photodiode arrives a signal with a mean frequency value of ω in an envelope that has frequency α. The $\sin \alpha t$ and $\cos \alpha t$ terms correspond to the interference between the reflected carrier (which is the sum of the prompt and leakage fields) and the sidebands that are phase-locked to the prompt field and therefore, these interference terms are the ones that contain the phase information on the laser and that should be kept for the error signal. If the modulation is slow enough, only the cosine term exists, since $F(\omega)F^*(\omega+\alpha) - F^*(\omega)F(\omega-\alpha)$ is real. If the sidebands are sufficiently far from the resonance frequency, they get completely reflected $F(\omega \pm \alpha) = -1$ and that term is entirely imaginary, making the sine the only component of the interference.

In our case we modulate the EOM with fast frequency (α) and to keep only the sine term, the signal must be demodulated by using a mixer. This multiplies the signals from the photodiode (α') and from the signal generator that drives the EOM (α): $\sin \alpha t . \sin \alpha' t = \frac{\cos(\alpha-\alpha')t - \cos(\alpha+\alpha')t}{2}$, followed by a low-pass filter to keep only the dc signal $\cos(\alpha - \alpha')t$. A phase shifter between the signal generator and the mixer assures that both paths have the same phase delay, since otherwise the signals may have a phase shift of 180° which results in a vanishing dc signal: $\cos \alpha t . \sin \alpha' t = \frac{\sin(\alpha'-\alpha)t - \sin(\alpha'+\alpha)t}{2}$, where only $\sin(\alpha' - \alpha)t = 0$ exists after filtering, as $\alpha = \alpha'$.

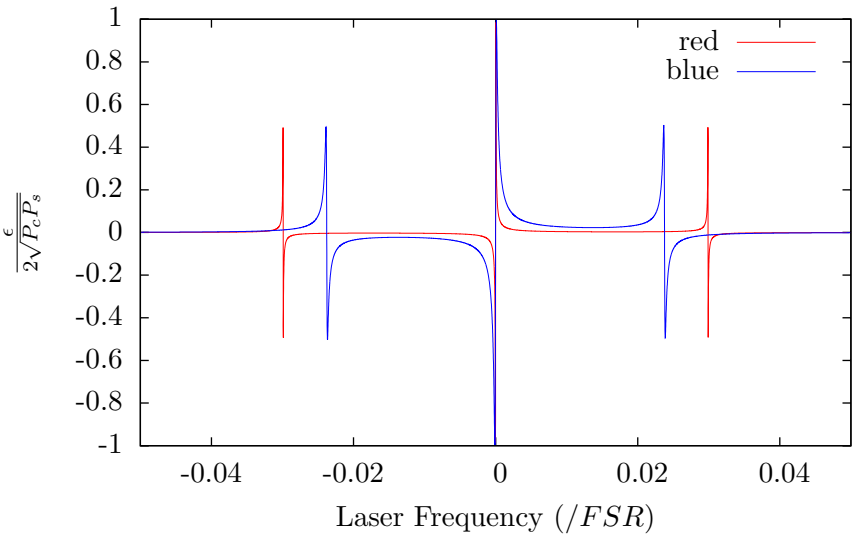

Figure 3.10: Error signal for the blue and red frequencies as a function of the frequency of the lasers with respect to FSR, assuming a finesse for the blue laser of 30000 and for the red 188000 and a modulation frequency around 800 and 6000 times the cavity's resonance line width, respectively.

As in our case, the modulation frequency α is much larger than the cavity line width the voltage error signal is given by (see figure 3.10):

$$\epsilon_v = 2RP_0J_0(\beta)J_1(\beta)\Im\left[F(\omega)F^*(\omega+\alpha) - F^*(\omega)F(\omega-\alpha)\right] \tag{3.9}$$

where R is the responsivity of the photodiode.

The reflection coefficient in function of the laser frequency, in the case the finesse is very high and assuming $|r| \approx 1$, can be written as [77]:

$$F(\omega) = -\frac{2i(\omega-\omega_0)/\delta_{cav}}{1+2i(\omega-\omega_0)/\delta_{cav}} \tag{3.10}$$

where ω_0 is the cavity resonance.

By substituting (3.10) into (3.9) and assuming a frequency of the laser similar to the resonant one ($\omega - \omega_0 \leq \delta_{cav}$), the following expression for the error is reached:

$$\epsilon_v = \frac{8RP_0J_0(\beta)J_1(\beta)}{\delta_{cav}} \frac{\omega-\omega_0}{1+4\left(\frac{\omega-\omega_0}{\delta_{cav}}\right)^2}. \tag{3.11}$$

This has a slope that can be calculated by its derivate with respect to the resonance frequency ω_0:

$$\frac{\partial\epsilon_v}{\partial\omega_0} = -\frac{8RP_0J_0(\beta)J_1(\beta)}{\delta_{cav}}. \tag{3.12}$$

It is possible to observe that for small deviations (noise) the error signal is proportional to the frequency difference between the laser and the resonance of the cavity. This slope is shown [76] to be maximum when $J_0(\beta)J_1(\beta) = 1.08$ which corresponds to a ratio between the power of the sidebands and the carrier of 0.42.

However, when the noise sidebands have a frequency which is far enough from the carrier, they (that are phase locked to the carrier prompt field and therefore to the laser field) will make a beat signal with the carrier reflected field which has a component of the leakage field (that could not follow the rapid phase fluctuations of the laser). And unlike the previously seen frequency discriminator, the lock will act as an optical phase detector.

Assuming that the noise corresponds to a sinusoidal phase variation of the laser electric field $\phi(t) = \phi_0 + \chi\sin(\omega_N t)$, this field is modulated twice, with

large sidebands created by the EOM and narrower ones created by the noise:

$$E_{inc} = E_0 \left[J_0(\beta) e^{i\omega t} + \frac{J_0(\beta)\chi}{2} \left(e^{i(\omega+\omega_N)t} - e^{i(\omega-\omega_N)t} \right) + J_1(\beta) \left(e^{i(\omega+\alpha)t} - e^{i(\omega-\alpha)t} \right) \right] \tag{3.13}$$

which was calculated as previously and where the terms $\alpha \pm \omega_N$ were not considered, as they are not important to the sign with α (which is what gives the error signal).

The reflected field was calculated by assigning the correspondent reflection coefficient to each sideband, by assuming that the laser is on resonance ($F(\omega) = 0$ which makes $F(\omega + \omega_N) = F^*(\omega - \omega_N)$) and that α is large enough to consider $F(\omega \pm \alpha) = -1$:

$$E_r = iE_0 J_0(\beta)\chi e^{i\omega t} \Im \left\{ e^{i\omega_N t} F(\omega + \omega_N) \right\} - 2iE_0 e^{i\omega t} J_1(\beta) \sin(\alpha t) \tag{3.14}$$

To get the voltage error signal, the field is squared to get the power, and only the terms that vary with $\sin(\alpha t)$ are kept, due to the combined action of the mixer and the low-pass filter:

$$\epsilon_v \propto \frac{2\omega_N/\delta_{cav}}{\sqrt{1 + 4(\omega_N/\delta_{cav})^2}} \chi \cos(\omega_N t + \phi) \tag{3.15}$$

$$\text{where [78]: } \phi = -\operatorname{atan} \left\{ \frac{\Re\{F(\omega+\omega_N)\}}{\Im\{F(\omega+\omega_N)\}} \right\} = -\operatorname{atan} \frac{2\omega_N}{\delta_{cav}} \tag{3.16}$$

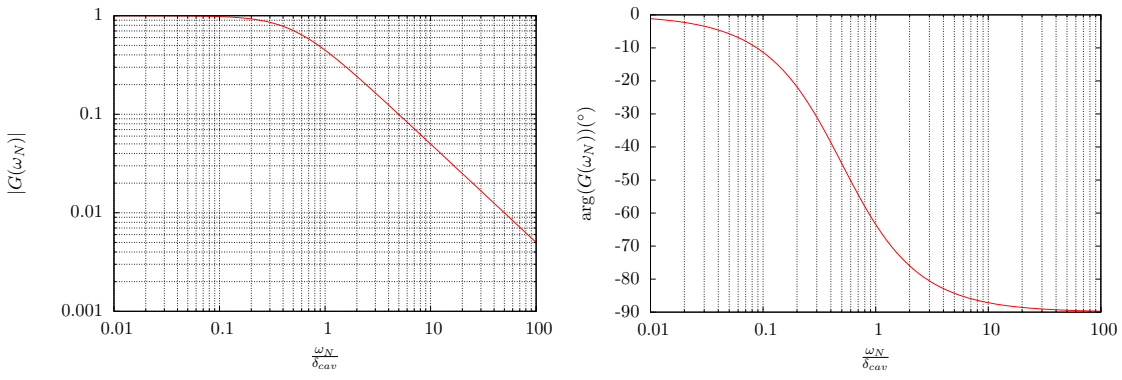

(a) (b)

Figure 3.11: Amplitude (a) and phase (b) of the transfer function of the PDH lock.

Therefore, the transfer function of this lock (that acts as a discriminator) is $G(\omega_N) = \frac{1}{1+2i\omega_N/\delta_{cav}}$, which is similar to a low-pass filter (see figure 3.11) with a

cut-off frequency of $\omega_{cut} = \frac{\delta_{cav}}{2}$.

With noise frequencies that are below the corner frequency, the error signal ϵ_v is proportional to ω_N, but above it there is a phase lag of 90° and a gain roll-off of 10dB/decade, which means that in the error signal the sensitivity is reduced as 1/f.

The final electronic error signal is therefore measured in volts per hertz of the frequency of the laser, up to the cut-off frequency.

The capture range of the lock is given by $\omega \pm \alpha$ and therefore, in principle, the larger the frequency modulation the larger the range in which the lock can keep the laser on resonance. However, as it can be seen in figure 3.10 the error signal between the fringes on the sides and the central part diminishes with an increase in the modulation frequency, noise in that region may cause zero crossings that will turn the laser out of lock. In practice, the capture range is only approximately a couple of line widths of the cavity.

3.5 Optical Setup

The optical setup for the implementation of STIRAP is constituted by two parts: the Pound-Drever-Hall locking scheme, where both *master* lasers are frequency-locked to a cavity's resonance (represented in figure 3.15), and the locking of the *slave* laser to the frequency-stabilized *master* (represented in figure 3.13).

For ECDLs, there is an optimal range of optical feedback: if the feedback is too small, it is possible that the gain in only one frequency is not enough for the "lasing" to happen; if the feedback is too large, the diode may get destroyed. Typically that optimal range is between 20% and 30 %. To increase the resolution of the grating (in order to feedback only one frequency), it is desirable that the number of lines in which the beam strikes is maximized, and therefore the beams should be horizontal (it is worth reminding - section 3.1 - that, as laser diodes are used, the beam shapes are elliptic). However, in the case of the blue lasers, the optical feedback of the grating (2400lines/mm - GH13-24U, *Thorlabs*) for the vertical polarization that a horizontal beam has, is too low (around 6-7%). That made necessary the placement of a half-wave plate between the collimation lens and the grating, which increased the optical feedback to 30%, making the "lasing" in a single mode possible. These half-wave plates had to be placed with a tilt to avoid the formation of another Fabry-Pérot. For the red laser diodes, the optical feedback given by the grating (1800l/mm - GH13-18V, *Thorlabs*), when the diode is adjusted for the beam to be horizontal, is enough without a have

plate (around 25%).

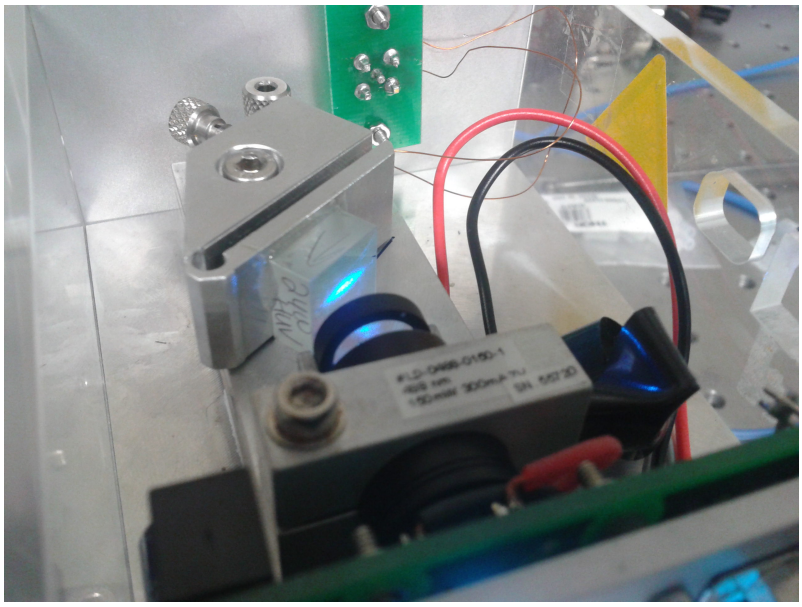

Figure 3.12: Photograph of an external cavity diode laser in a Littrow configuration.

When the PZT's angle is readjusted the beam's angle also changes, and to avoid the realignment of the whole setup every time that happens, mirrors (all the mirrors in the setup are 1" broadband dielectric mirrors - BB1-E02, *Thorlabs*) placed in kinematic mirror mounts were placed at the end of every acrylic box that contains the ECDL. In this way, the alignment problem was solved, since all it takes is to adjust that mirror.

It is possible to observe in the figure 3.12 that the laser beam created by these kind of lasers has an elliptical form. For the fiber coupling to have a maximum efficiency the beams should be round, therefore anamorphic prism pairs, that magnify or diminish the beam in one direction (2.3 times for the wavelength 487nm and 5 times for the 652nm, *Altechna*) while maintaining its dimension in the other direction, were also needed after the laser box.

As all optic components can cause back reflections and the laser diodes are very sensitive to these, a good optical isolation is needed. It is known that the polarizing beamsplitters are much more efficient in the transmission (in which there is only $10^{-3} - 10^{-4}$ of the wrong polarization) than in the reflection (where the wrong polarization rises to $1 - 2\%$). Typically, as fibers have to be well aligned with the optical path for the coupling to be efficient, they create back reflections. To minimize that effect, the connectors for the fibers (P3-488PM-FC-5, *Thorlabs*) used were angle-polished connectors (APC), which are polished

at an angle of 8° with the normal of the optical axis. However, to be sure the back reflections were suppressed, the lasers that may couple with the fibers through the reflection from a polarizing beamsplitter, which are the slave lasers (see figure 3.15), have a double stage optical isolator . The *master* laser with wavelength 487nm has an optical isolation of 39,5dB (IO-3-488-HP, *Thorlabs*) and the one for 652nm is a double stage isolator with isolation of 52,6dB (IOT-3-650-LP, *Thorlabs*). For the *slave* lasers, as it was already mentioned, both isolators are double stage: for the 487nm laser the isolation is of 56,5dB (IOT-3-488-LP, *Thorlabs*) and for 652nm it is above 60dB (84501002000, *Qioptiq*). These isolation is enough to suppress the undesired optical feedback.

As shown in the figure 3.15, after the optical isolator, the beam coming from the *master* laser is split by the combination of a half-wave plate and a polarizing beamsplitter, which allows to control the power ratio between both resultant beams. Around 100μW are sent into the Pound-Drever-Hall setup. There are several reasons for the separation of this locking scheme. As the PDH scheme is extremely susceptible to alignment, in this way, the PDH becomes insensitive to changes in the path if, for example, the PZT angle is adjusted. Also, the cavity should be kept in a breadboard that damps the vibrations, minimizing the coupling of the cavity to the environment. For the lasers, although they should also be placed in a breadboard with some kind of damping (such as a vibration damping rubber placed underneath the breadboard) the requirements are not so strict. Therefore, the PDH setup is on top of a single-honeycomb breadboard (PBH51502, *Thorlabs*), whereas the lasers were placed on aluminum breadboards (MB3045/M, *Thorlabs*). Furthermore, as the spatial matching of the laser beam with the optical resonator's TEM_{00} mode is crucial for the coupling to the cavity, and as the fiber couples more efficiently the TEM_{00} mode, the beam that comes out of it is cleaner and in the desired mode, favoring the coupling with the cavity. All this justifies the separation between the PDH setup and the other where the lasers are.

The electro-optic modulators (appendix 5) are made of a birefringent material and therefore, are very sensitive to the polarization. If the beams polarizations are not perfectly aligned with the principal axis of the modulator (in this case horizontally), the modulation will not only be in frequency but also in amplitude, as there are half-wave plates placed after each EOM that will convert the variation of the polarization created by the EOM in amplitude modulation. This will deteriorate our Pound-Drever-Hall lock causing the lock point to be shifted from the cavity resonance. To make sure the right polarization is sent into the

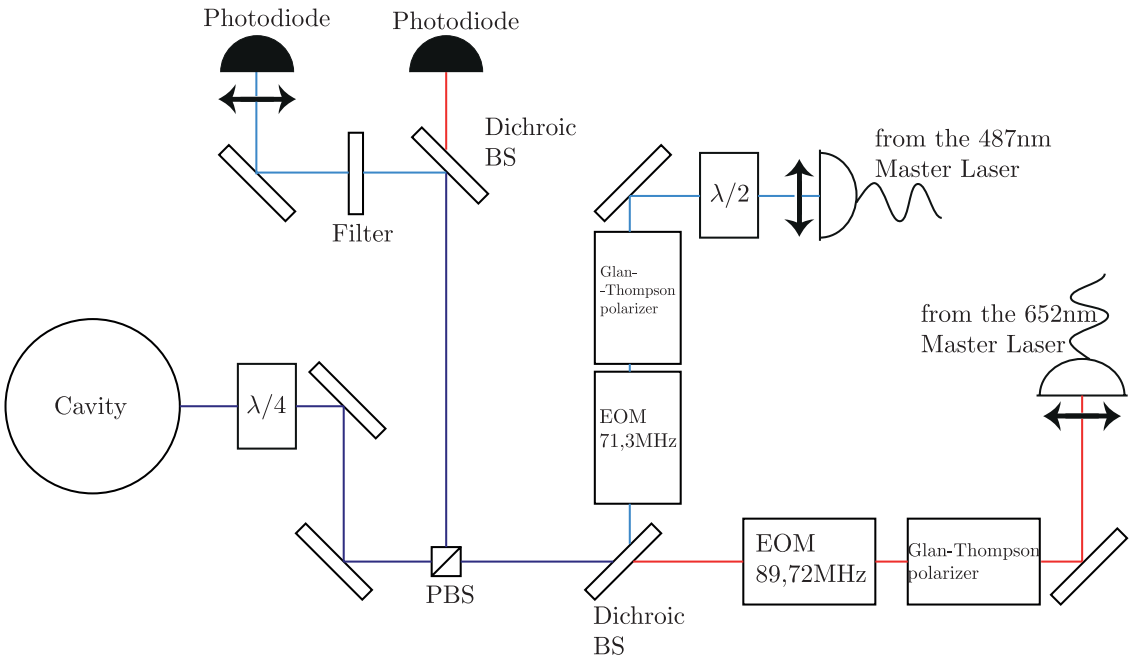

(a) Scheme

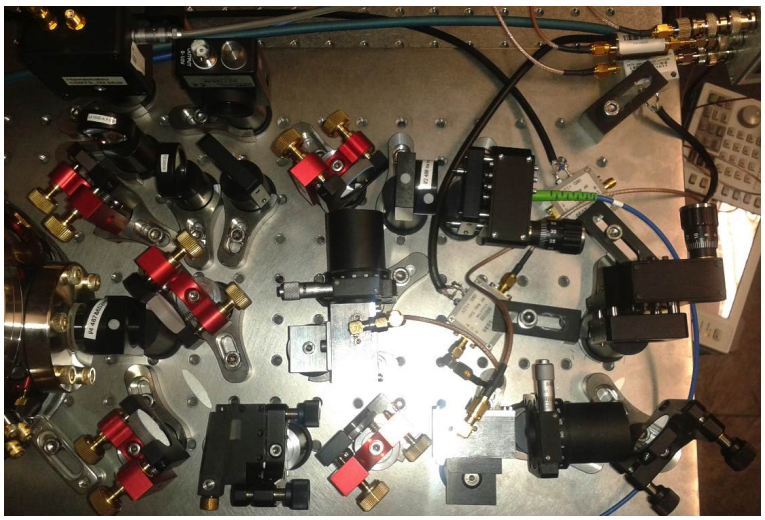

(b) Real setup

Figure 3.13: Overview of the optical setup that corresponds to the Pound-Drever-Hall lock of the *master* lasers of both frequencies to a cavity's resonance.

EOM, a half wave plate followed by a Glan-Thompson polarizer is placed before each. Another factor that can lead to amplitude modulation is the change of the polarization at the end of the fiber caused by bending of the fiber or by thermal effects, since there is a half-wave plate after it. To avoid it, Panda fibers were used. These fibers are polarization-maintaining due to their birefringence caused by the existence of stress rods. If the laser light is sent into the fiber with

a polarization aligned with the polarization axis of the fiber, it will go out at a definite polarization and no amplitude modulation occurs after the half-wave plate.

For a good mode-match with the cavity mode TEM_{00}, and since its Rayleigh length is so large (15cm), the collimation lenses (A414TM-A, *Thorlabs*) after the fiber were chosen to assure that the size of the laser beam matches the cavity mode's one.

After the frequency modulation by the EOMs driven by a signal generator (SG386, *Stanford Research Systems*) at their respective resonance frequencies (71,3MHz for the blue laser and 89,7 for the red), the beams with the two frequencies are superimposed in a dichroic beamsplitter (DMLP567, *Thorlabs*) that transmits the red light and reflects the blue one. As the light has horizontal polarization, it is transmitted through the PBS (BPS0101, *Casix*) that is coated for both wavelengths.

For a good alignment, which is necessary for the mode-matching, it is desirable to have two mirrors, prior to the cavity, which can be adjusted since they are placed on kinematic mounts. When the alignment is complete, the reflection of the beam that goes into the cavity hits the mirrors in the same point as the incident laser beam. To help to find the right mode, a photodiode (DET10A/M, *Thorlabs*) was placed after the cavity to look at the transmission which will have maxima whenever the laser is resonant with the cavity's resonances. To be able to see them, the laser frequency is swept slowly through the PZT with a triangular signal (see figure 3.14). To be sure that the right mode was found (TEM_{00}) it is convenient to look directly at the shape of the transmission, and see if it corresponds to a single maximum gaussian. Furthermore, another characteristic of this cavity, is that due to its high symmetry, when the cavity resonance is scanned by the laser frequency through the PZT, the first order modes disappear while the incident beam is even when aligned to the cavity, as they correspond to anti-symmetric modes. A way to have a better mode-matching is to adjust focus and to maximize the 0-order mode transmission peak while minimizing the higher order modes by adjusting the mirrors in front of the cavity.

The light that is reflected from the cavity or that leaks out through the first mirror passes through the quarter wave plate, becoming vertically polarized. Afterwards, it will be picked out by the PBS, split by another dichroic mirror and sent into each photodetector that only have to be as fast as the created sidebands (for the red laser the photodiode used is DET10A/M, *Thorlabs* and for the blue is S5973-02, *Hamamatsu*). These signals after amplified are mixed with

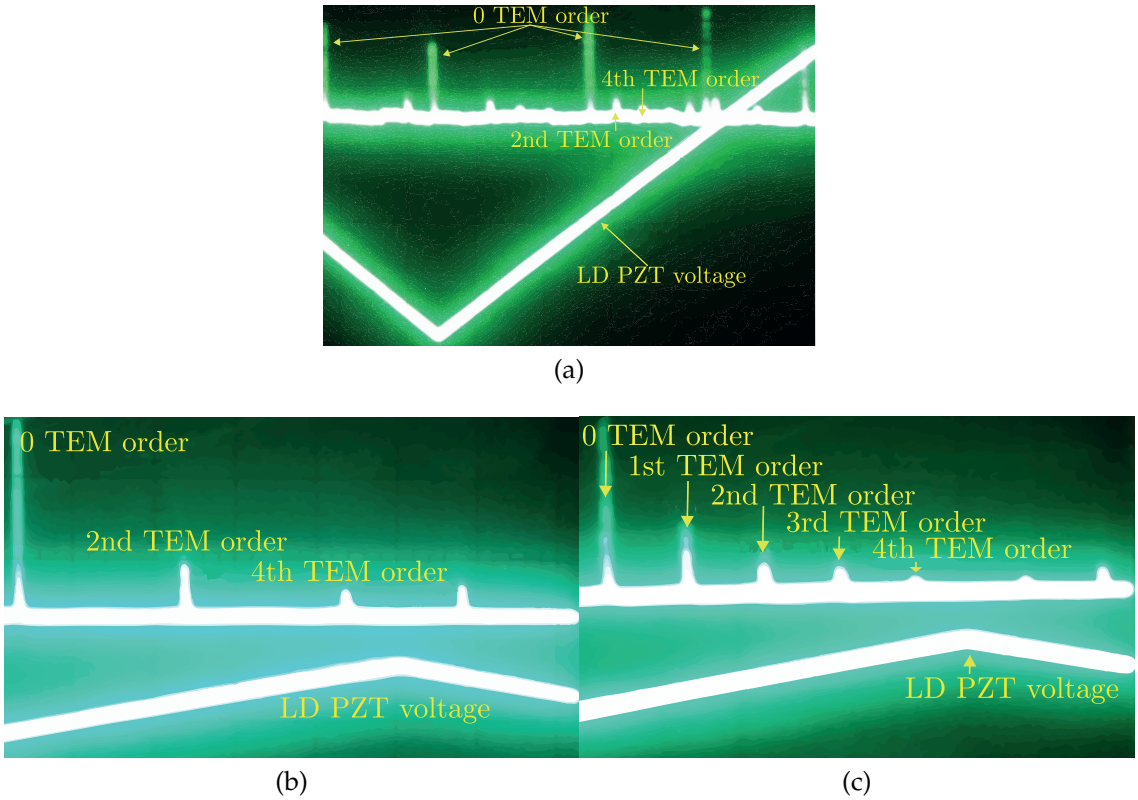

Figure 3.14: Transmitted resonant peaks and PZT voltage as a function of time when the scan is: a) more than 2×FSR and the beam is aligned which suppresses the odd orders of TEM modes b) around the TEM_{00} with the aligned beam c) around the TEM_{00} mode and the beam is misaligned, which enables the visualization of the odd order TEM modes .

the output of the signal generator with the right phase, which is adjusted with the length of the cables, and after low-pass filtered the resultant error signal is sent into the servo, that will control the current of the laser and the PZT voltage to hold the laser on resonance with the cavity's mode.

The slave laser is the one that will send the light into the experiment by adjusting a half wave plate combined with a PBS placed after the optical isolator. But for its frequency to be very stable (which, as discussed earlier, is a requirement for STIRAP) and tunnable, the beating between the *master* and the *slave* lasers has to be locked to a reference, which will be controlled via computer.

The optical setup for this beat signal scheme is shown in figure 3.15. After part of the light of the *master* laser being sent into the PDH setup and part of the *slave*'s light into the experiment, the two beams, which are mode-matched by the anamorphic prism pairs, are superimposed in a PBS. As they have orthogonal polarizations, the polarizations have to be mixed for the interference to happen and the beat signal seen. A quarter wave plate combined with a PBS allow a

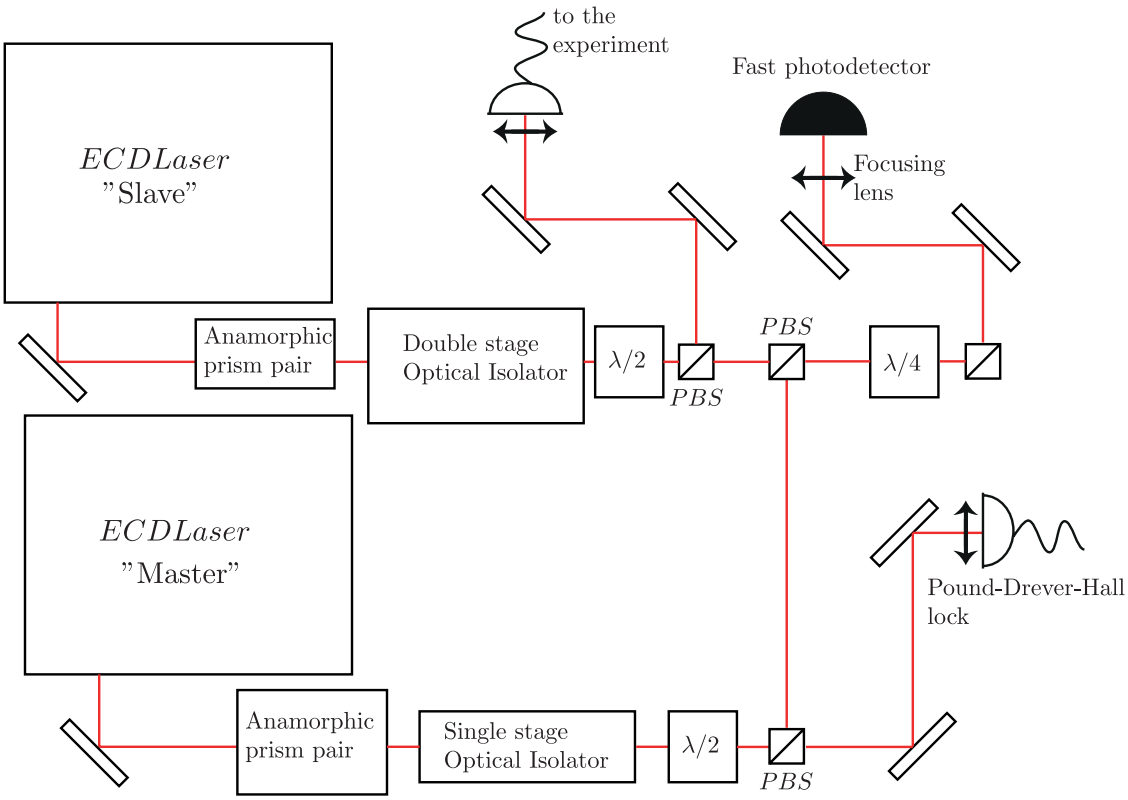

(a) Scheme

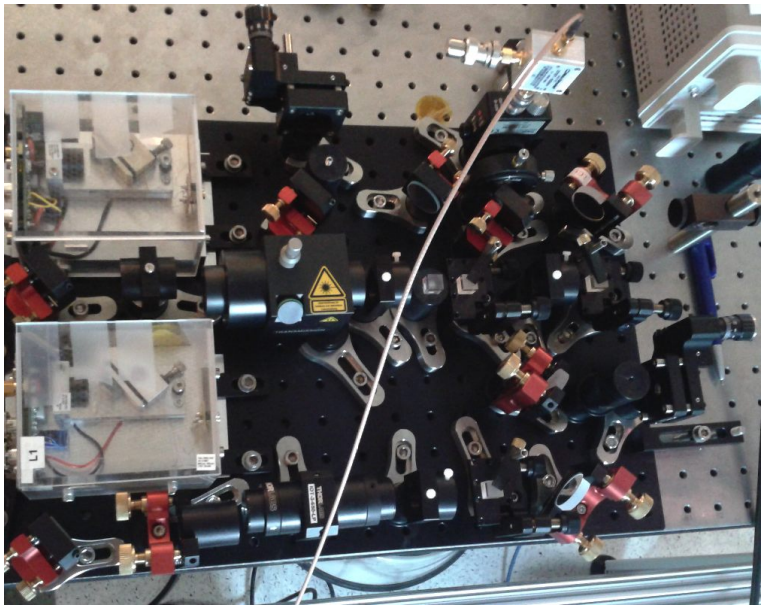

(b) Real setup

Figure 3.15: Overview of the optical setup of the beating between the laser beams coming from the *master* and the *slave* lasers for one of the laser frequencies.

maximization of that interference and, subsequently, of the signal.

In this part of the setup, the photodetectors (818-BB-45, *Newport*) are required

to have a large bandwidth, since the *slave* laser frequency may have to be scanned through more than one FSR of the cavity for the desired detuning to be achieved (it can't be a scan of only one FSR, since there is a chance that the desired frequency is at the frequency of the cavity mode, which would correspond to a DC signal, that is hard to detect). These photodiodes have a very small area, which makes necessary to the alignment two angle-adjustable mirrors, as well as a focusing lens in a translating mount.

The beat signal (with frequency Δf - see figure 3.16) is later on sent into a mixer to which is also sent the signal from the computer-controlled reference (f_x). These signals are kept at a difference of 50MHz, since in the digital phase lock (DPL) the output of the mixer is compared to a local signal with 50MHz created by a voltage-controlled oscillator. In the DPL the phases of these signals are compared, and an appropriate error signal as a function of the phase differences is created, which is zero in case they have the same phase. Furthermore, the error signal saturates for high values of phase difference. This signal is then sent into the servo (similar to the one used for the PDH lock).

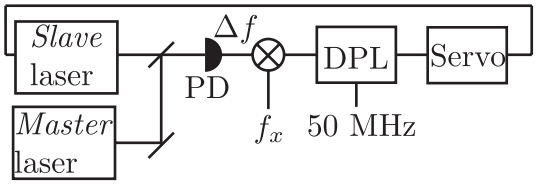

Figure 3.16: Overview of the electronic setup used to lock and control the slave laser: the Δf is the frequency difference between the *master* and *slave* lasers' frequencies and f_x comes from a signal generator that is controlled via computer.

4 Experimental Results

4.1 Characterization of the lasers

A complete characterization of the external cavity diode lasers, which were discussed in section 3.1, is extremely important. Only by knowing how the laser output reacts to changes in the PZT and the current, can we control the light that goes into the experiment by adjusting these parameters.

As it was analyzed in section 2.3.9, to reach the desired Rabi frequencies the laser light that is sent into the experiment should have around 10mW. Like that, it is necessary to know which is the current intensity that the diode must be fed with to reach that output power. In figure 4.1 it is possible to observe that dependence, which is roughly linear.

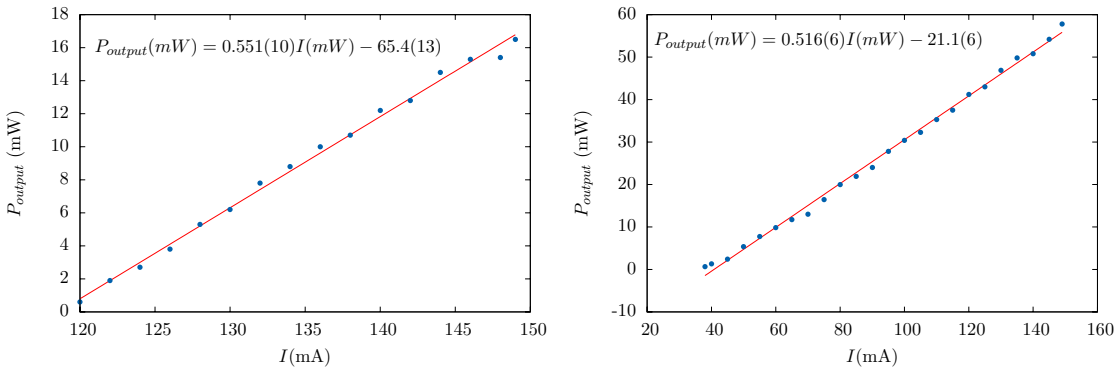

(a) Red lasers

(b) Blue lasers

Figure 4.1: Output power for the red a) and blue b) lasers as a function of the current's intensity.

In addition, keeping the intensity constant, the power varies with the wavelength, which can be adjusted through the refractive grating angle. The figure 4.2 shows that dependance for the red light.

The mode-hop-free tuning range for the blue lasers is around 20GHz and for the red lasers is approximately 12GHz, which is enough for our purpose

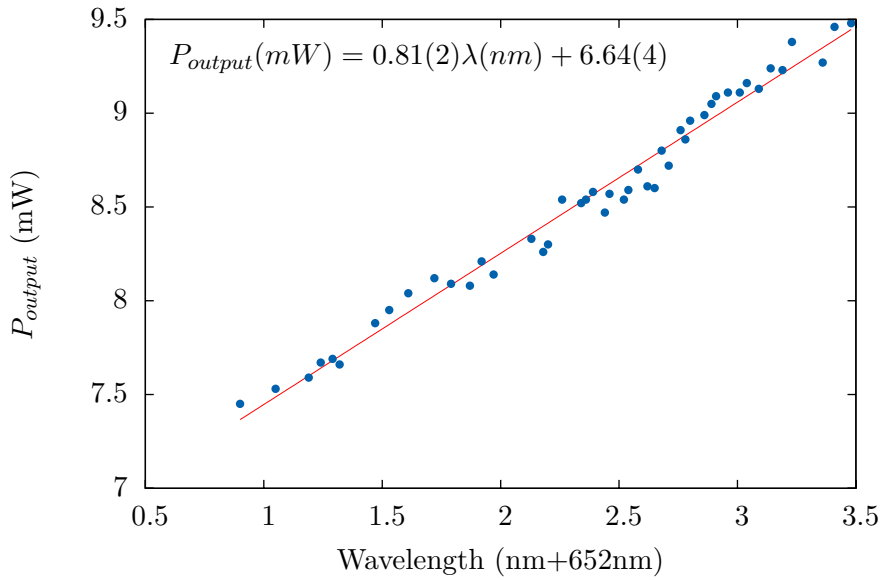

Figure 4.2: Output power of the red laser as a function of the wavelength maintaining the current intensity constant.

(as already discussed in chapter 3). Furthermore, by changing the angle of the grating manually with the fine-thread screw, it is possible to scan over 1THz with each laser, which is more than the needed few hundreds of GHz.

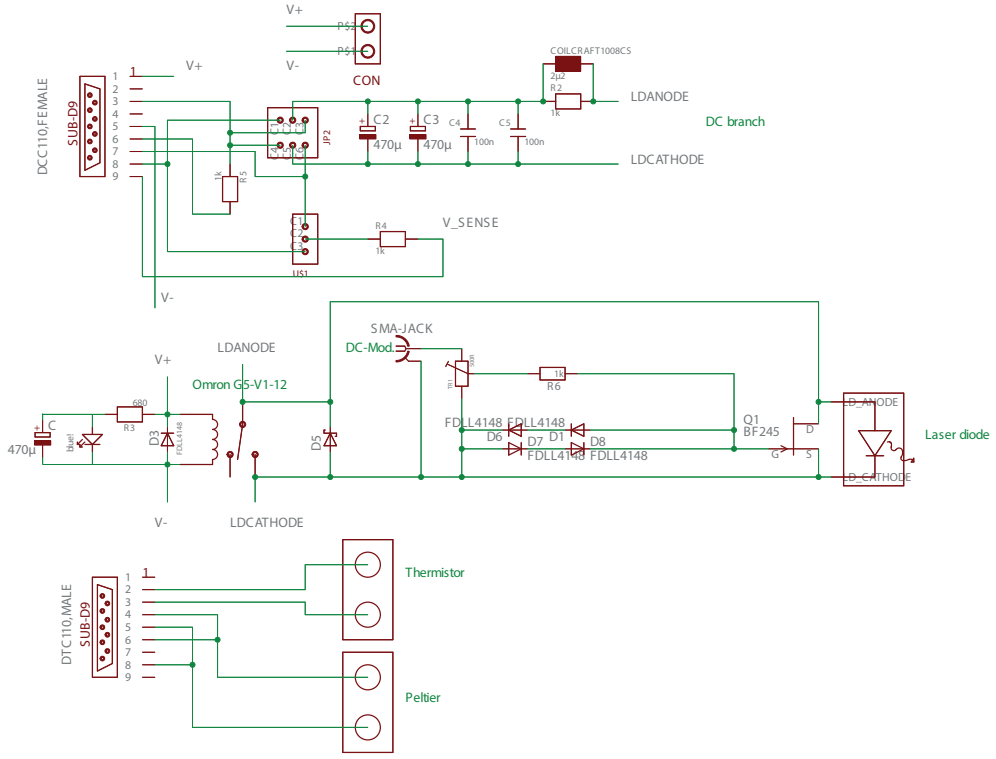

Figure 4.3: DC modulation and protection circuit used for the ECDLasers.

In figure 4.3, it is represented the circuit designed to protect the laser diode against voltage peaks - which may destroy them - and to enable DC-modulation (to do the scanning necessary to find the right intermediate state and the detuning that allows larger transfer efficiency).

It is possible to observe that in the DC-branch there is a low-pass filter constituted by a capacitor and a coil. The DC-modulation is made through a FET (field-effect-transistor) with which the current that passes through the diode is regulated by the voltage that exists between the gate and the source of the FET. There is also a protective part of the circuit, composed of several diodes that don't allow the voltage between the laser diode's anode and cathode to be higher that a certain value. A relay short-circuits the anode with the cathode when the circuit is turned off to avoid electrostatic discharges. If the relay bounces instead of immediately shorting, voltage peaks exist due to the filter coils in the DC-branch which can destroy the laser diode. To prevent that, a capacitor was placed in parallel with the relay.

This circuit together with the frequency response of the diodes to variations of their own current intensity, result in the transfer functions that are represented in figure 4.4. These plots show how much the laser frequency changes per volt of the applied voltage as a function of the frequency of the sinusoidal oscillations that modulate the laser through the DC-modulation input.

As the voltage output of the photodiode is proportional to the light power and not to its frequency, it was necessary to build an electronic setup similar to an asymmetric RF-Mach-Zender interferometer to get these transfer functions. The beat signal between the *master* and *slave* lasers was sent into a photodiode, the voltage signal that went out of the photodiode was split and while part was sent to the spectrum analyzer, the other was sent into a mixer which multiplied the signal with itself after passing through a 5m cable (delay of 25ns). The resultant signal was afterwards low pass filtered. The output result of the Mach-Zehnder is a voltage that depends sinusoidally on the frequency of the beating. By checking with an oscilloscope the maximum amplitude of this voltage and at the same time observing in the spectrum analyzer to which frequency difference that oscillations corresponded, it was possible to determine the slope at the mean value of the oscillation, which allowed to convert the voltage recorded by the network analyzer into frequency, which was the property we wanted to measure.

It is possible to conclude that for the blue laser the frequency at which there is 180° phase shift is approximately 4MHz whereas for the red laser it is 1MHz. The gain for the blue laser is practically flat until 2MHz increasing 5dB before it

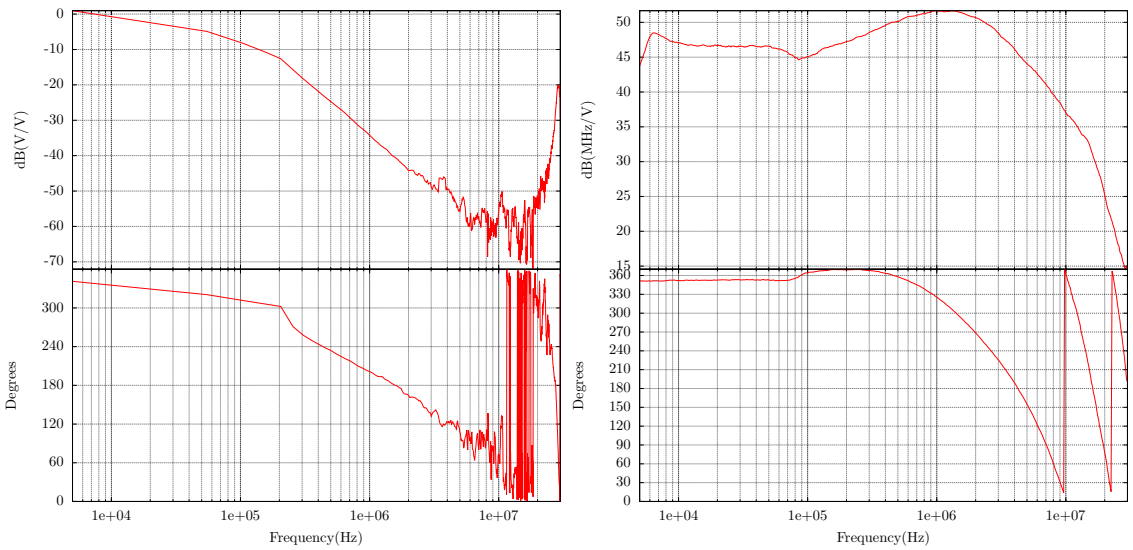

(a) Red laser (b) Blue laser

Figure 4.4: Transfer function of the red and blue lasers, where in the y-axis it is represented the variation of the laser frequency by volt applied to the DC-branch and the x-axis represents the frequency of the oscillations that were applied in that branch.

starts to roll off with 20dB/decade. Its phase is constant until 1MHz, after which it starts to roll off. In the red laser transfer function, the gain doesn't suffer many variations until 200kHz, where a roll off of 30dB/decade occurs. At that same frequency it is possible to observe a kink in the phase after which the phase roll off is more evident. The units of the gain for the red laser are dB(V/V) because no calibration was made.

4.2 Electronic circuits of the Pound-Drever-Hall lock

The reflected light of the cavity is sent into photodiodes (S5973-02, *Hamamatsu* for the 487nm and DET10A/M, *Thorlabs* for 652nm) that are 50Ω terminated. The signal is afterwards amplified by two low-noise amplifiers (ZFL500-LN *Minicircuits*) and multiplied in a mixer (ZRPD-1+, *Minicircuits*) with the signal from the signal generator (SG386, *Stanford Research Systems*). The output of the mixer is low-pass filtered (SLP-15+, *Minicircuits*) and sent into the phase lock circuit.

For the modulation of the EOMs, the signal coming of the signal generator is split (ZX10-2-12-S+, *Minicircuits*) and while part is sent into the previously

discussed mixer, the other part is attenuated by two attenuators (VAT-10+ and VAT-6+, *Minicircuits*), amplified (LNA-1030, *Minicircuits*) and sent into the EOM. The reason for using attenuators is that, while the signal has to be strong enough to activate the mixer, it has to have the right intensity for the sidebands to have a power ratio in relation to the carrier that maximizes the slope of the error signal (as discussed in section 3.4).

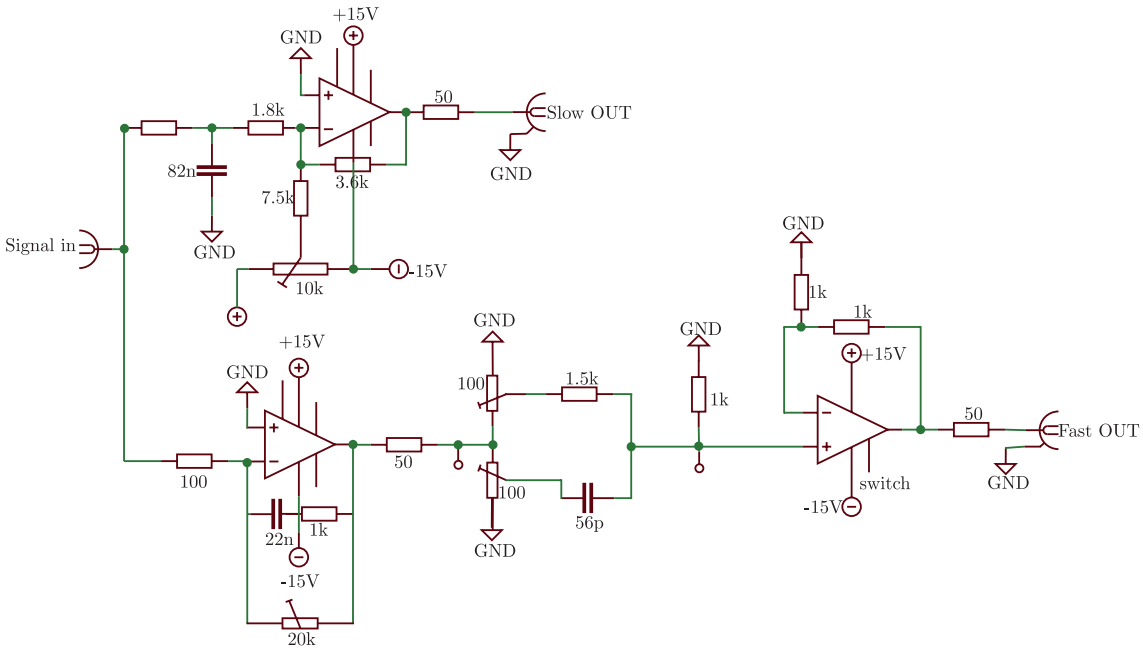

Figure 4.5: Lock box circuit where there are two branches: for fast deviations through the laser injection current and for slow through the PZT voltage.

The lock circuit is shown in figure 4.5. It has two branches: the upper which controls the PZT voltage and lower part that is sent into the DC-modulation branch of the laser.

In the PZT part there is a low-pass filter with a cut-off frequency of around 4kHz, this signal is amplified and sent into the piezo circuit, which will be discussed later. In the lower part the input signal passes through an operational amplifier in the inverting amplifier configuration, with a tunable gain for low frequencies. Afterwards, the signal is separated in two branches and by adjusting two knobs the proportional and the differentiating part of the circuit can be regulated, in order to have a stable lock performance.

As it was discussed in section 3.3, to suppress completely the noise, the gain would have to be infinite, especially at low frequencies where most of the vibration noise frequencies lie. In this way, integrators are required. Nevertheless, each of these introduces a 90° phase shift which summed with the delays due to

the length of the cables gives rapidly rise to a frequency where the phase shift is 180° (negative feedback), which limits the bandwidth of the loop. The implementation of a derivative part extends that bandwidth, as it introduces a phase advance of 90°. After the proportional-derivative part the signal is amplified in a non-inverting amplifier with gain 2 that can be switched on and off, activating or deactivating the fast DC-modulation branch.

The PZT is only used to keep the laser on lock with slow drifts or other very low frequency effects. The PZT circuit to which the signal is sent to, after being amplified and low-pass filtered in the lock box, is represented in figure 4.6. Mainly this signal has a large gain at low frequencies made though the action of the integrators. In this branch the bandwidth is not so important because, after a certain frequency of deviations, the gain of the injection current takes over (the cutoff frequency is adjusted in the last integrator represented).

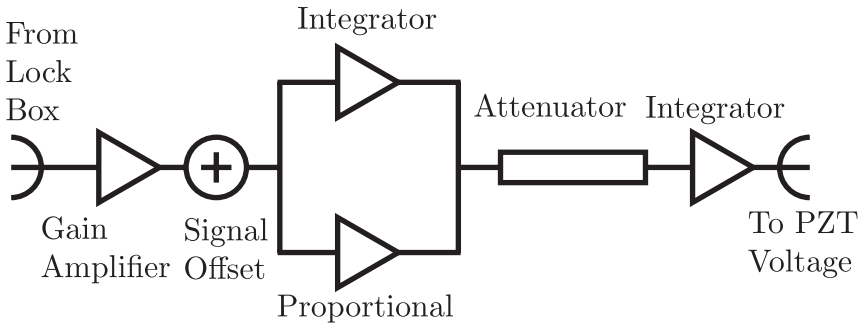

Figure 4.6: Part of the electronic circuit that constitutes the PZT branch of the servo.

The transfer functions of the lock boxes for red laser and the blue one are represented in the figure 4.7. The gain is fairly flat up to 3kHz where it starts to decrease with 20dB/decade. At 0.2MHz the differentiating part takes over, however, the differentiating gain of the red laser which increases the gain in 15dB is substantially larger than of the blue one, for which is almost flat. This was done because the blue laser response, represented in figure 4.4, already has the desired shape for the differentiating part.

For a power incident in the cavity of 50μW, the signal amplitude in the oscilloscope has a value of 30mV. Using equation (3.9) and the measured amplitude of the signal, it was possible to determine the slope of the error signal to determine the conversion from volts to hertz.

This enables to get the overall gain of the feedback loop. To calculate it, the gain of the lasers, of the lock and of the low-pass response of the cavity were

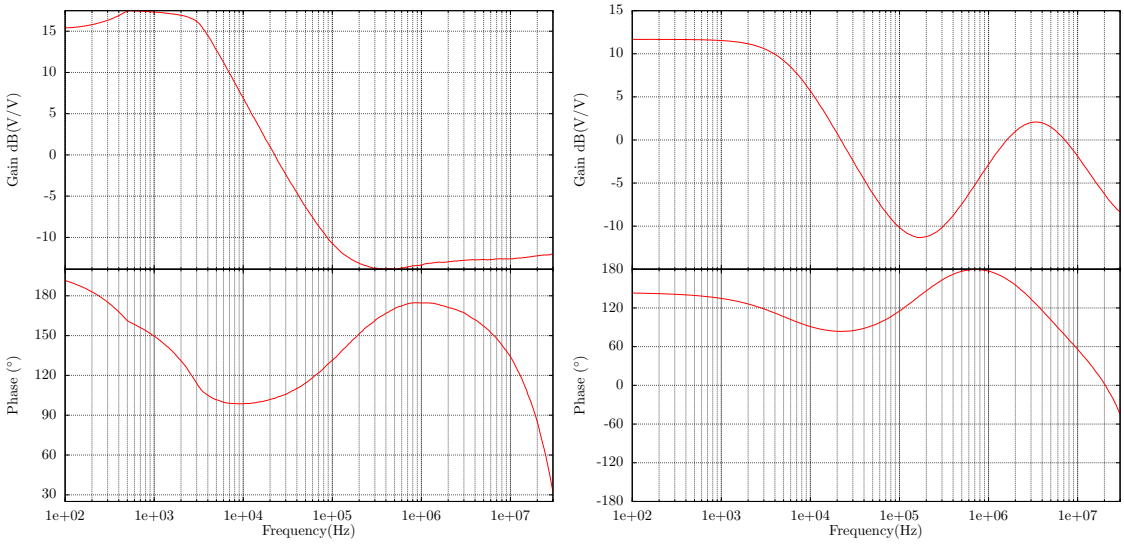

(a) Blue laser (b) Red laser

Figure 4.7: Transfer function of the lock boxes used in the Pound-Drever-Hall technique for the blue and red lasers.

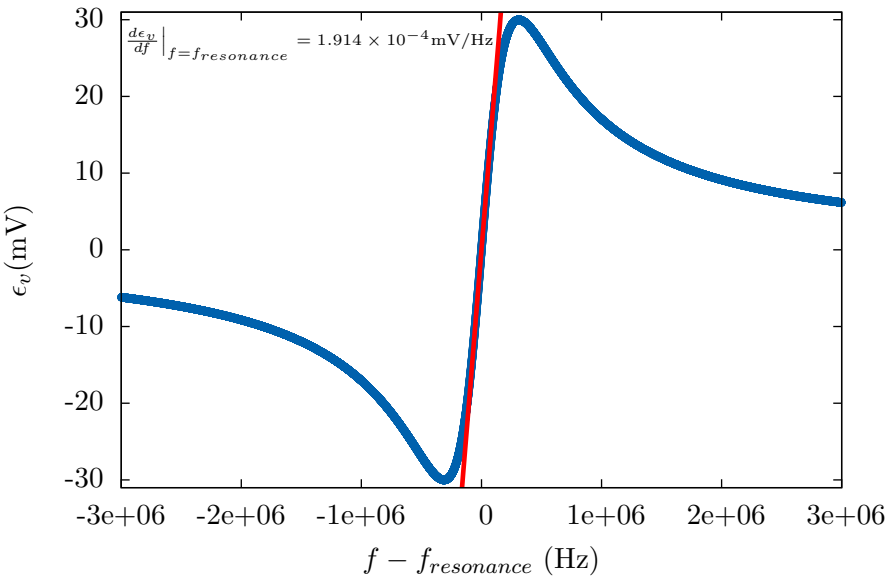

Figure 4.8: Error signal near the resonant frequency and determination of its slope.

considered, as well as the conversion factor calculated through the error signal.

For both lasers, the gain as a function of frequency is the desired one, with a slope of 20dB/decade. It is possible to see that the bandwidth of the blue laser is 1.5MHz and the phase stability margin is 120°. Despite not being possible to know which is the bandwidth of the red laser since the calibration was not

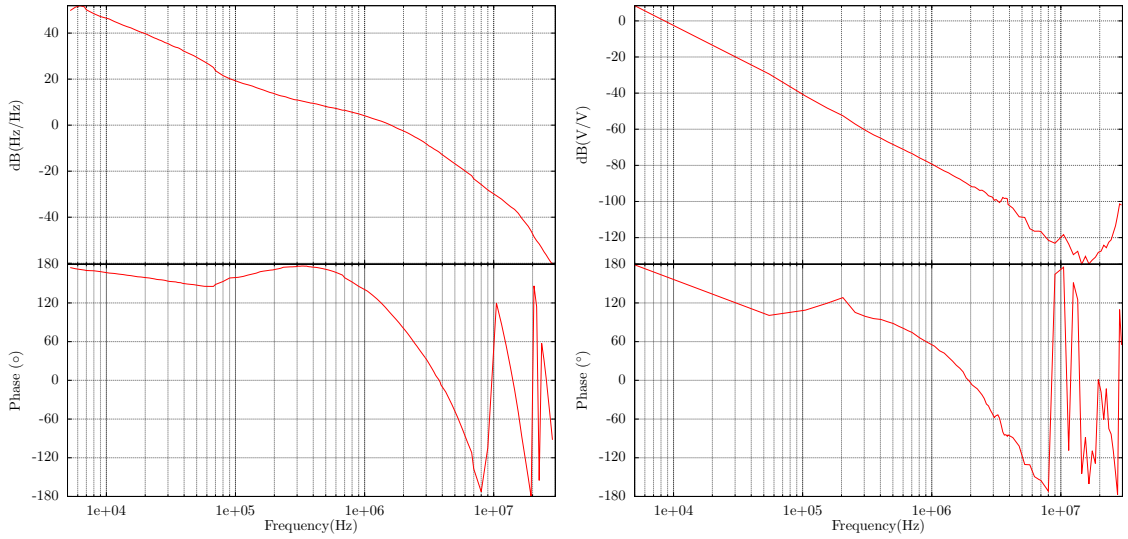

(a) Blue laser (b) Red laser

Figure 4.9: Gain and phase shift of the feedback loop for the blue and red frequencies.

made, it is still possible to conclude that it is less than 2MHz, as at this frequency the phase is shifted by 180°.

4.3 Finesse of the cavity

Assuming that the steady-state intensity inside the cavity is $I_{cav}(0)$, if the input laser field is rapidly turned off this intensity will decay as $I_{cav}(t) = I_{cav}(0)e^{-\frac{t}{\tau_{cav}}}$ where τ_{cav} is the photon lifetime inside the cavity. The variation in the intensity of the field inside the cavity (ΔI) during one round trip is given by:

$$\frac{\Delta I}{\tau_{round}} = \frac{I_{cav}.2.(R-1)}{2L/c} \text{ where R is the reflectivity } R = r^2 \tag{4.1}$$

$$\frac{dI_{cav}}{dt} \approx -\frac{I_{cav}2\pi FSR}{\mathcal{F}} \text{ where for high finesse cavity's: } \mathcal{F} = \frac{\pi}{1-R} \tag{4.2}$$

which allows to conclude that $\tau_{cav} = \frac{\mathcal{F}}{2\pi FSR} = \frac{1}{2\pi\delta_{FWHM}}$. The mean number of round trips of a photon in a Fabry-Pérot cavity ($\langle n \rangle$) is given by:

$$\langle n \rangle = \frac{\tau_{cav}}{\tau_{round}} = \frac{\tau_{cav}}{2L/c} = \tau_{cav}.FSR = \tau_{cav}.\mathcal{F}.\delta_{FWHM} = \frac{\mathcal{F}}{2\pi} \tag{4.3}$$

$$\mathcal{F} = \frac{c\pi\tau_{cav}}{L} \tag{4.4}$$

A cavity ring-down measurement was made for each laser frequency, allowing to know the cavity's decay time and therefore the finesse.

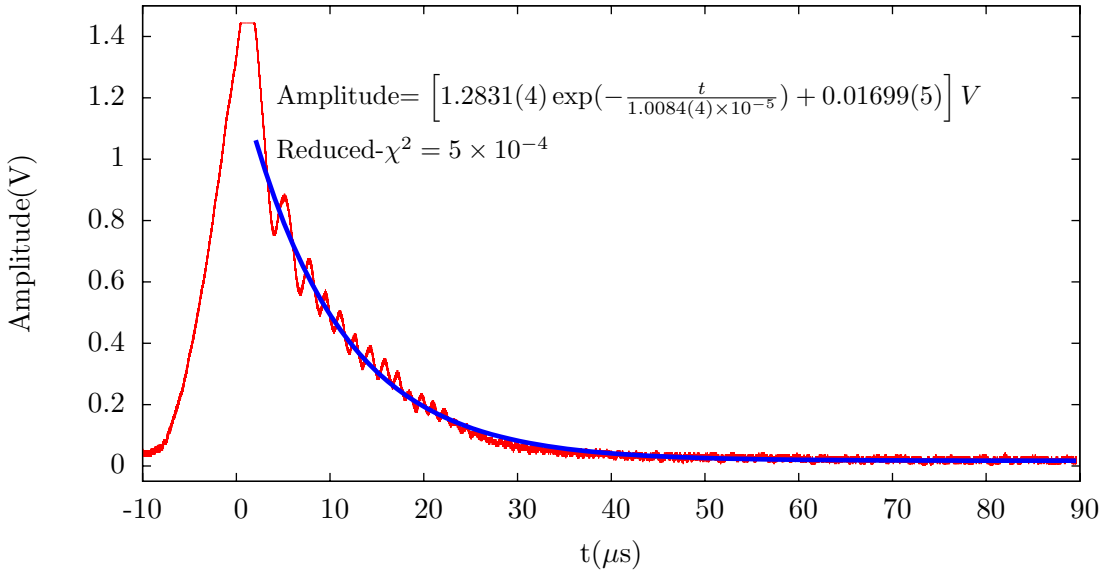

(a) λ=652nm

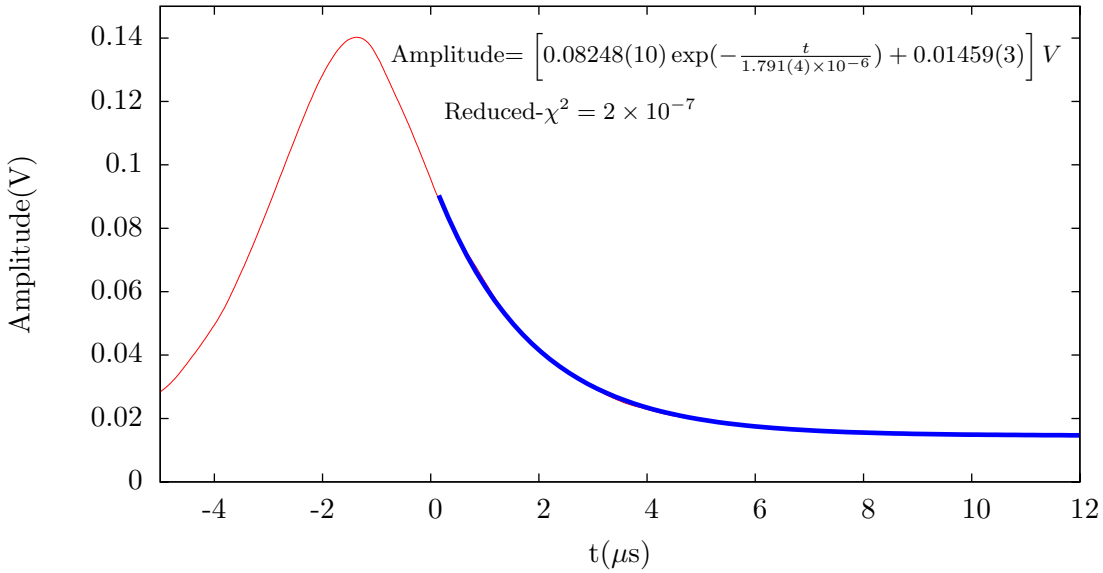

(b) λ=487nm

Figure 4.10: Cavity ring-down measurement to determine the cavity decay time where the blue line corresponds to the fit of the exponential decay of the data represented by the red line. In the a) measurement the signal was amplified with a low noise voltage amplifier (SR560, *Stanford Research Systems*) prior to its recording by the oscilloscope. In the b) measurement the data shows the averaging of 64 triggers.

This method consists of driving with a laser source the optical resonator at

the TEM_{00} longitudinal mode frequency, which will build a field inside the cavity. If the input field (laser) that drives this build up is shut off shorter than the cavity decay time (for example by using an AOM [79] which validates the consideration that this field can be regarded as a step-function) and the decay of the cavity field is recorded in time through the transmission, the cavity decay time (τ_{cav}) can be determined by fitting an exponential to the data. However, it was shown [80], that if the frequency of the laser is scanned across the longitudinal mode frequency of the cavity, the laser light is resonant with that center frequency only by a short time, which is equivalent to the AOM setup. The scan speed regulates the intensity of the field that is build up inside the cavity and it can be adjusted for the transmission to be large enough to enable the data recording, but it has also to be fast enough to still mimic the step-function characteristic. With this kind of external cavity diode laser it is simple to scan across a frequency: through the PZT voltage the grating angle can be periodically changed by using a function generator.

The function generator was run at a frequency of 100Hz with an amplitude of 80mV. The transmitted signal was detected with a photodiode (DET10A, *Thorlabs*) 500Ω terminated, recorded using an oscilloscope (DSO7000, *Agilent*) with a bandwidth of 20MHz, in the high resolution mode (which averages a couple of samples) and triggered on the rising edged of the transmitted signal.

The finesses determined by fitting the data with exponentials (see figure 4.10) are 189950 ± 80 for the wavelength 652nm and 33740 ± 80 for λ =487nm, which results in $(1 - R)$ equal to 17ppm and to 93ppm, respectively. The line width of the cavity is for the red laser 15kHz and for the blue one 89kHz. The oscillations in amplitude occur due to the interference between the intracavity field and the driving laser field.

For $\lambda = 652nm$, the relative powers of the different modes were determined: 68% in the 0-order mode, 20% in the 2nd order mode, 7% in the 4th order mode and the other modes have 5%. It was also determined using the oscilloscope that the modulation sidebands carry a power of 40% (which is the ratio correspondent to the maximum slope of the error signal). For $\lambda = 487nm$ the 0-order mode also carries about 65% of the power distributed by the several modes. The mode-matching can still be improved if lenses with a slightly larger focal length are used after the fibers.

For $\lambda = 487nm$, for a coupled power of 10% of the incident (observed by looking at the dip of the reflected power), 1% of the incident power is transmitted. From the already calculated $(1 - R) = 93ppm$, it is possible to conclude

that the transmission is 9ppm (which is in accordance to the specifications given - see figure) and the losses are 84ppm.

4.4 Laser line width

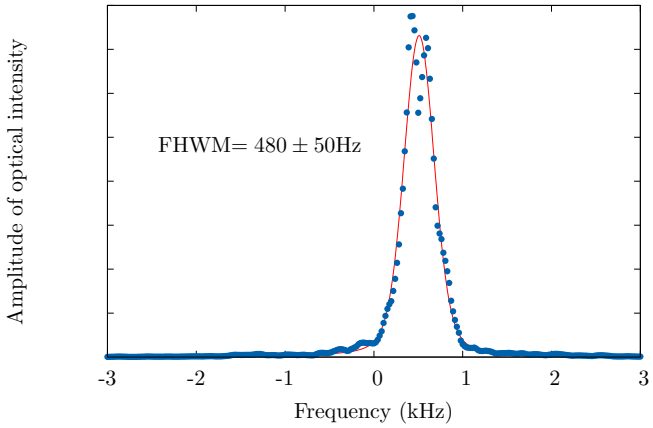

(a) linear y-axis, resolution: 100Hz, sweep: 0.101s

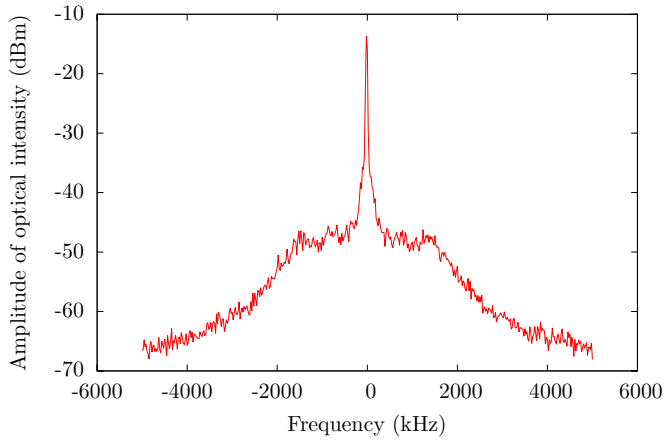

(b) logarithmic y-axis, 10 times averaged , span: 10MHz, resolution; 30kHz, sweep: 0.123s

Figure 4.11: Line shape of the blue laser: it was possible to determine a sub-KHz line width of $480 \pm 50Hz$.

In the hydrogen experiment, which is located in the same building where our setup is, a laser was built with a line width of 1Hz and with a frequency similar to our blue laser. This allowed to use part of the light of that laser to make a beat signal with our laser. The output was sent into a photodiode (DET10A, *Thorlabs*) and was observed in a spectrum analyzer. The line width recorded with a spectrum analyzer can be considered all coming from our blue laser, as

the other line width is much smaller. The blue laser line width is smaller than 1kHz - see figure 4.11. The line shape pedestal is about 4MHz wide which is similar to the bandwidth of the lock. The root-mean square fluctuations of the laser in a 10 seconds measurement is 200Hz. The power incident on the cavity during the measurements of the line width was 50μW and for this power the signal-to-noise ratio is 1.2 (measured with a bandwidth of 1GHz).

4.5 Stabilization of the cavity

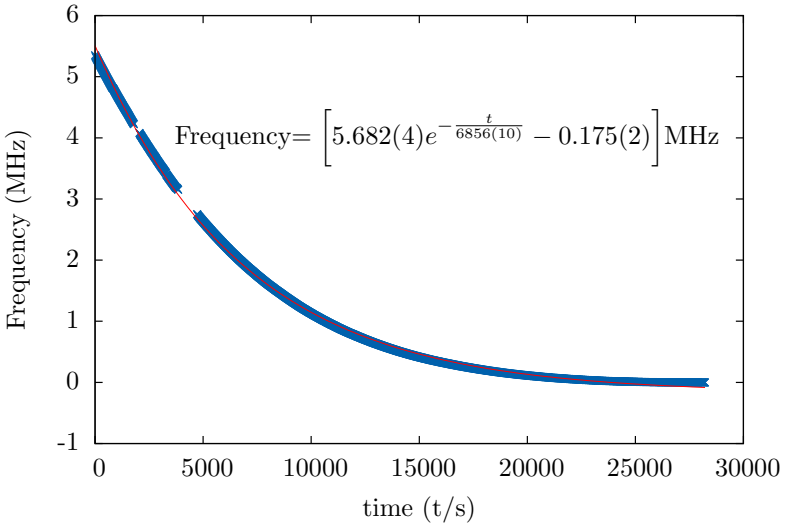

Figure 4.12: Thermalization of the cavity.

The beat signal frequency was recorded after a change in temperature [1] to determine the thermalization time by fitting an exponential to the frequency in function of time (see figure 4.12). The thermalization time found after measurements being made for several temperatures was (6400 ± 450)s, which means that after twelve hours the thermalization can be considered complete (around 1mK to the asymptote).

As it was discussed in section 3.2, it is necessary to keep the cavity at the zero-crossing temperature to minimize the drift due to temperature. To determine that temperature, the beat signal frequency was recorded for several temperatures around a minimum of the beat signal frequency and a parabola was fitted to these data. This minimum in the beat signal frequency corresponds to

[1] Both the cavity temperature and the current intensity and temperature of the lasers are controlled through a modular platform PRO8000, *Thorlabs* - the module used to control the cavity's temperature is TED8000 and the ones to control the laser diodes are LDC8000.

a maximum in the frequency of the laser since the 1Hz line width laser was at a higher frequency than of our blue laser's one, which means that at the zero-crossing temperature the spacer dimensions are minimized.

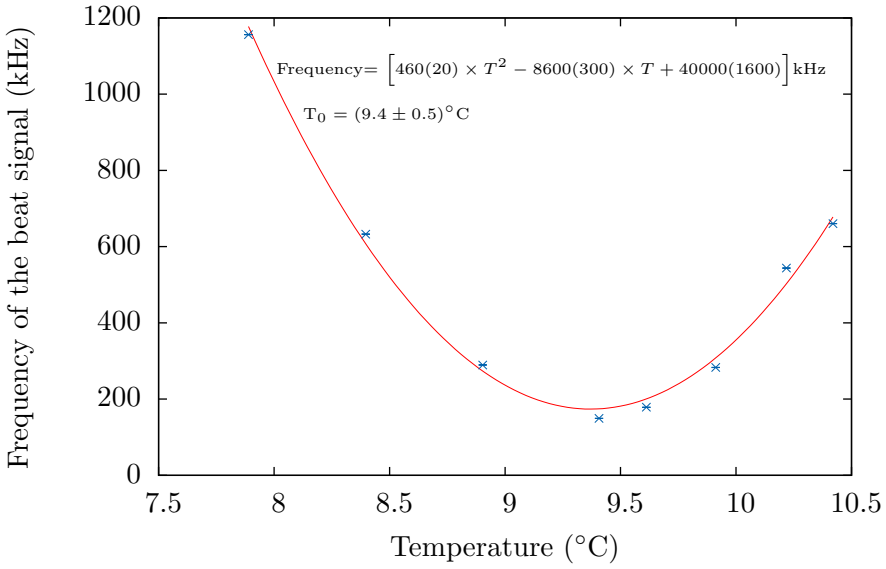

Figure 4.13: Determination of the zero crossing temperature by changing the temperature through the temperature controller and recording the frequency after 12 hours.

A four-days measurement keeping the temperature constant was taken to observe how the frequency changes in time.

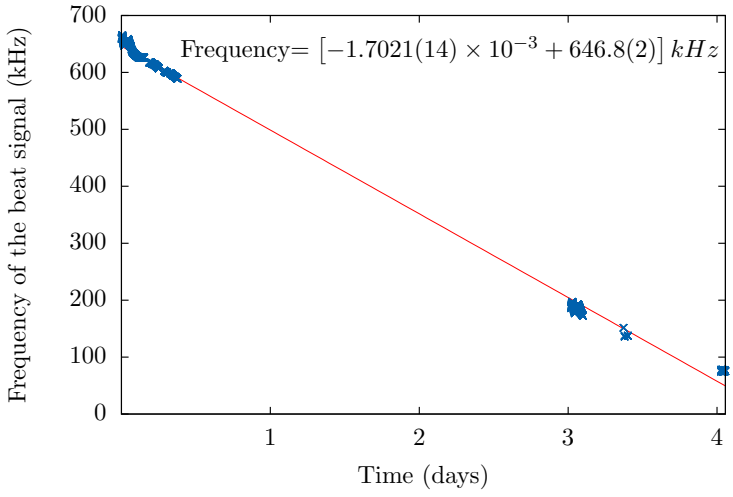

Figure 4.14: Frequency of the beat signal recorded during four days. The solid line is a fit to the data which shows there is a constant drift at the fixed temperature: 9.257°C (within the range of the zero-crossing temperature)

It is clear by looking at the four-days recording of the frequency beat signal (although not during the whole time - figure 4.14), that there is a drift fairly constant for a determined temperature. The drift rate was afterwards recorded for several temperatures - see figure 4.15.

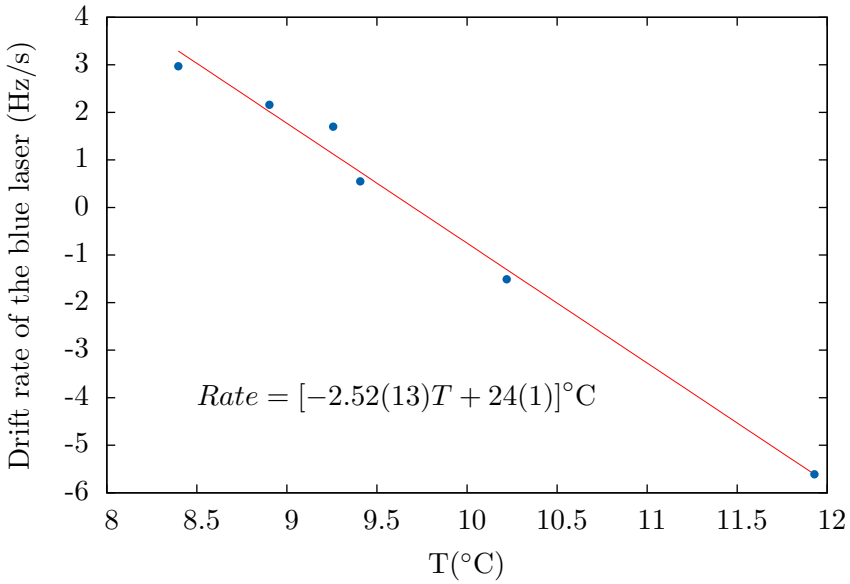

Figure 4.15: Drift rate of the laser frequency as a function of the temperature of the cavity.

The drift is minimized (rate 0Hz/s) for a temperature of $(9.5 \pm 0.6°\text{C})$, which is within the range of the previously determined zero crossing temperature. The fact that there is a drift which has a rate that varies with the temperature of the cavity (see figure 4.15) didn't allow to determine the zero-crossing temperature more precisely. To check wether there is a correlation between room temperature and cavity resonance frequency, the temperature and humidity were recorded at the same time of the beat frequency, for several days.

As it is possible to observe in figure 4.16, there are frequency oscillations with an amplitude 1kHz and a period of around 1000s. At the temperature T=9.207°C there is no visible drift apart from the oscillations. After the temperature has changed to T=9.309°C, a drift of 0.7 Hz/s is observed as well as the same oscillations. The drift in the following day is approximately the same, but between the measurements the beat signal frequency dropped, which means that in the meanwhile a drift with opposite signal must have occurred (if there were no discontinuities). In addition, the oscillations amplitude decreased slightly to roughly 0,5kHz. The parameter humidity during the measurements suffered some oscillations, but with a different period from the frequency ones. The tem-

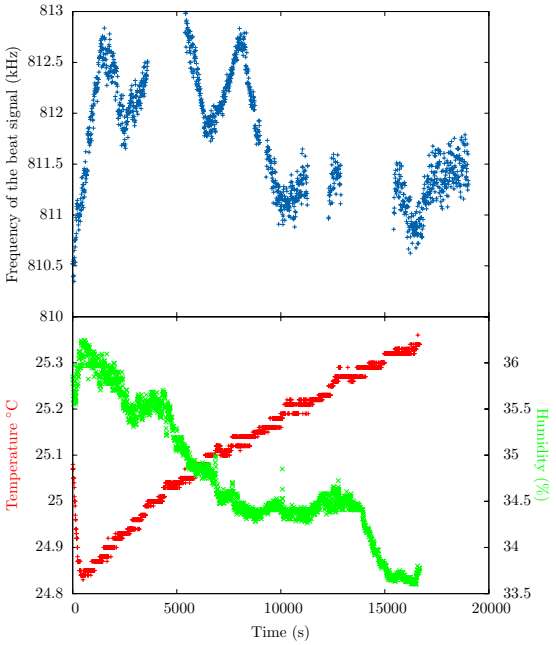

(a) day 1: T=9.207°C

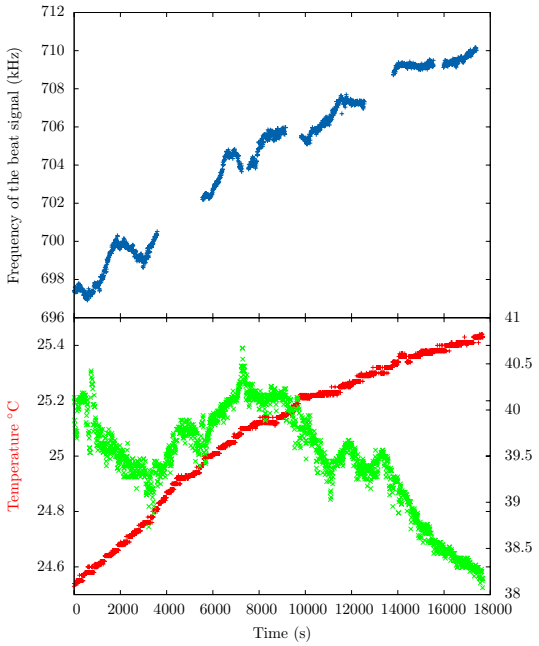

(b) day 3:T=9.309°C

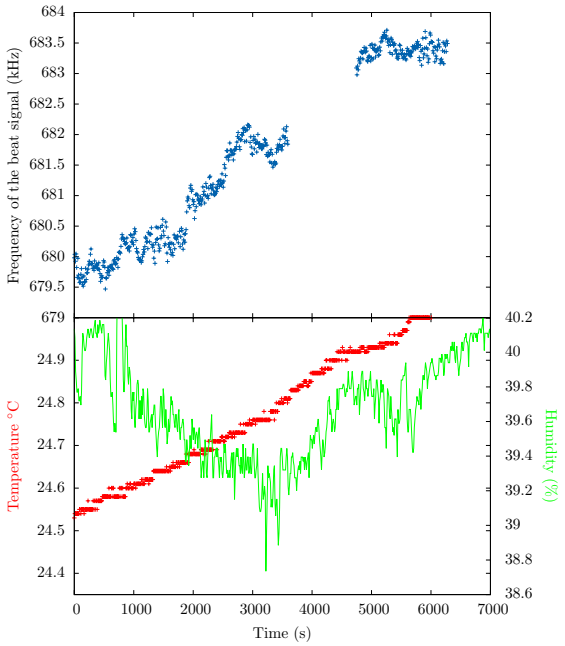

(c) day 4: T=9.309°C

Figure 4.16: Recordings of the beat signal frequency, room temperature and humidity for an incident power of 50μW in three different days: a) was recorded three days before b), and c) one day after it, the cavity's temperature was changed after day 1 from T=9.207°C to T=9.309°C.

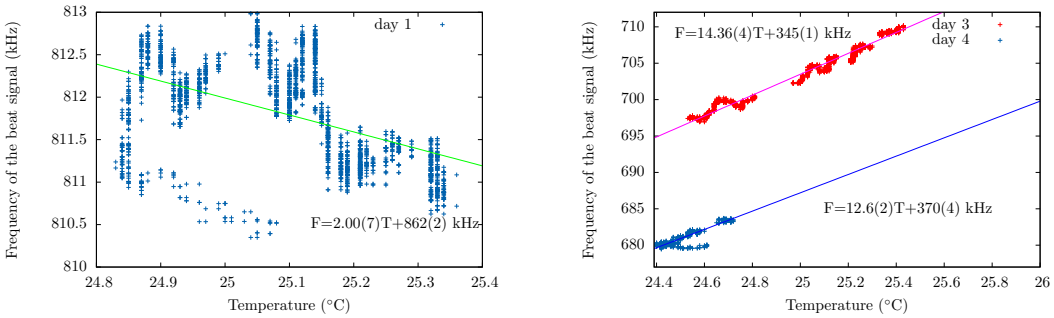

(a) day 1:T=9.207°C (b) day 3 and 4:T=9.309°C

Figure 4.17: Beat signal frequency as function of room temperature, for two different temperatures of the cavity: 9.207°C and 9.309°C.

perature during a day-time measurement always increase, which may lead to the drift that is seen. As it is possible to see in figure 4.16, from b) to c) the temperature dropped 0,9°, which is accompanied by the already discussed drop in the frequency of 30kHz (similar to the predicted by looking at the derivative of the parabola 4.13 at T=9.309°C - which would be 39kHz for this change in temperature).

In the figure 4.17, the beat signal frequency was shown as a function of temperature, with which it is possible to conclude that for a change in the room temperature, a change in the frequency of the laser occurs accordingly for the fixed temperature of T=9.309°C, as the slopes of the two linear fits are very similar. For T=9.309°C, the frequency is fairly constant with the variation of the room temperaure, which suggests that this is the zero-crossing temperature. It is clear that the cavity temperature is not completely uncoupled from the exterior one, which means that the lock parameters of the temperature controller have to be improved. In addition, most likely the temperature of 9.207°C is closer to the zeeo-crossing one, as the drift is practically zero even with an increasing room temperature.

When the EOM was heated, the beat signal frequency oscillated with a period of 300s and an amplitude of 1kHz, which means that the EOM can be cause of the oscillations. If so is confirmed, its temperature should be stabilized.

When the incident power on the cavity was changed from 20μW to 10μW, the frequency of the beat signal changed 1KHz, and when the change was made from 200μW to 100μW the change was of 8kHz. Which means that, in this case, there is no obvious advantage on decreasing the power significantly.

The half wave plate in front of the fiber optic that sends light into the Pound-

Drever-Hall setup was adjusted to minimize the power variation by looking at the reflected power from the cavity while heating the fiber, but still 9% of power fluctuation was observed. With 50μW, which is the power that was sent into the cavity during the measurements shown in figure 4.16, this power fluctuation corresponds to a frequency fluctuation of 450Hz, which is similar to the amplitude of the fluctuations observed, and may be the origin of the oscillations. This suggests that the lesser the power it is sent into the cavity, the lesser will the oscillations amplitude be. Power stabilization may be a solution if this conjecture is proved.

4.6 Noise

While the blue laser was locked to the cavity, a trace of the error signal ($u(t)$) was recorded with the oscilloscope during 0.1s with sample intervals of 25ns. Afterwards, the signal was fast Fourier transformed, squared and divided by a bandwidth around each frequency f: $\frac{|\langle\hat{u}(\omega)\rangle|^2}{f}$. With this trace a frequency resolution of 10Hz for a span of 40MHz was achieved.

The effect of the cavity response as a low pass filter ($G(\omega)$) was subtracted and the slope of the error signal (D) allowed to convert the voltage of the error signal in the difference between the laser frequency and the cavity's resonance frequency: $\frac{|\langle\hat{u}(\omega)\rangle|^2}{D^2|G(\omega)|^2 f} = \frac{|\langle\hat{\phi}\rangle|^2}{f}$. This gives the spectral density of the time derivative of the phase which corresponds to the difference between the laser frequency and the cavity resonance. It is needed to find a relation between the power and this time derivative, as we want to know the power spectrum of the laser which is given by the square of the electric field per bandwidth around f.

The electric field of the laser is given by $E(t) = e^{i\omega_0 t + i\phi(t)}$ where $\phi(t)$ is the phase, which varies in time, and ω_0 is the cavity resonance frequency. Assuming $\phi(t) \ll 1$, the electric field can be written as $E(\omega) = e^{i\omega t} + i\phi(t)e^{i\omega t}$ which after Fourier transformed has the following expression $\hat{E}(\omega) = (\delta(\omega - \omega_0) * \hat{\phi})(\omega) + \delta(\omega - \omega_0)$. Therefore the power of the error signal is given by

$$|\langle\hat{\phi}\rangle|^2 = \frac{|\langle\hat{\dot{\phi}}\rangle|^2}{\omega^2} \tag{4.5}$$

in which the derivative of a Fourier transformation was applied.

The noise of the power spectrum represented in figure 4.18 was averaged after a frequency of 10kHz. It is possible to see in the spectrum that a significant part of the power is below 100Hz. After that frequency the power is significantly

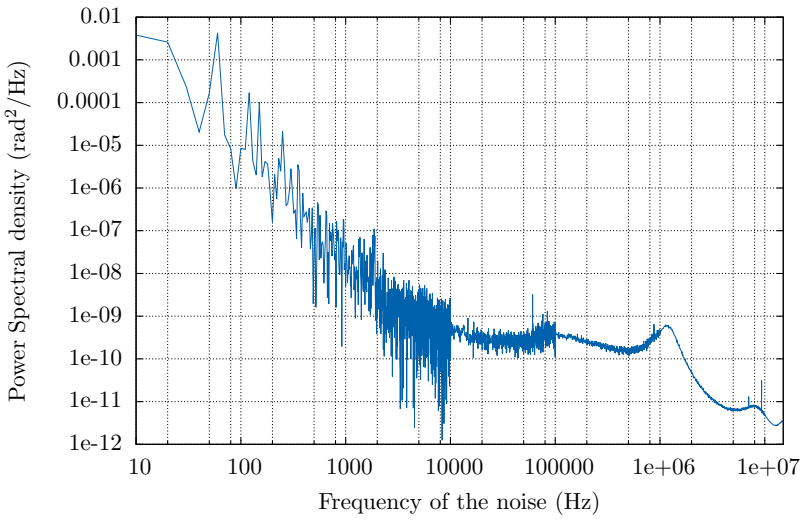

Figure 4.18: Power spectrum of the laser calculated through the noise in the error signal

reduced. Also it is noticeable the servo bump at approximately 1MHz, which was also possible to observe in the power spectrum recorded with the spectrum analyzer.

After integrating the resultant power spectrum (figure 4.18) in the noise frequency, it is possible to conclude that the assumption $\phi(t) \ll 1$ is correct, since $|\langle\hat{\phi}\rangle|^2 = 0.097$.

A lorentzian was fitted to the spectrum and the calculated line width is 34.8Hz which is much less than the expected 480Hz. However, it is needed to have in mind that this power spectrum is calculated exclusively through the error signal, which means that if there is thermal noise in the cavity, it won't be seen in this spectrum. Still, as the value is so much smaller than the recorded with the spectrum analyzer, it is possible that the line width from the laser with which we are beating the blue laser is increased by fiber noise, as the fiber used to get the light to our experiment has 10m, and that our laser line width is effectively smaller.

5 Conclusion and outlook

During the development of the project of this thesis an optical setup was assembled for the implementation of a scheme called stimulated Raman adiabatic passage. This setup will later be integrated into an experiment which is currently being built and aims to create ultracold polar molecules NaK. The STIRAP scheme is the last step towards the formation of those molecules: it will transfer the molecules from a weakly bound state to the rovibrational ground state where the dipole moment is large, allowing long-range interactions which can be tuned in the presence of electric fields.

This transfer has very specific stability requirements since the two-photon detuning must be zero during the whole transfer for the process to be adiabatic. Effects like the existence of several intermediate states, the decaying of these and noise were taken into account. The laser line width should be narrower than 1kHz and its peak should be stable within a few kHz for the transfer to be efficient.

To achieve the desired characteristics, two external cavity diode lasers in the Littrow configuration were built for each wavelength: 652,654nm and 486,995nm. One laser for each wavelength is locked using the Pound-Drever-Hall technique to a transfer cavity to achieve the desired stability. The cavity spacer is made of an ultra low expansion glass and the fused silica mirrors are coated for both wavelengths. For the red laser the finesse was determined to be 189950 and for the blue one 33740. Furthermore, the spacer of the cavity has a geometry that makes its length insensitive to vibrations and it is placed inside a vacuum housing with a pressure lower than 10^{-8}mBar, which has a temperature controlled thermal shield. The temperature of the cavity is set to its zero-crossing temperature which was determined to be 9.4 ± 0.5°C. The beams from other two lasers, one per wavelength, are partly sent into the experiment, while the other part is superimposed with the frequency stabilized laser beams, creating a beat signal that is locked to a reference that can be controlled through a computer. The maximum frequency offset of these lasers with respect to the frequency of the

stabilized ones is 6GHz which is equivalent to two free-spectral ranges of the cavity.

The whole optical setup was built, and the lasers, as well as the reference optical cavity, were characterized. The lasers were locked to the cavity and a line width of approximately 0.5kHz was reached for the blue laser. The line width for the red laser was not measured as there was no stable reference with which its light could be interfered. However, as the finesse of the cavity for the red wavelength is roughly six times larger than for the blue and the overall gain of the feedback loop has the same shape as of the blue laser, a sub-kHz line width is expected as well. The error signal of the blue laser when locked was recorded in time. This allowed to calculate a line width of 35Hz, which suggest that this width may be smaller than the one recorded in the spectrum analyzer.

The root mean squared fluctuations of the laser frequency when recorded during 10 seconds were measured to be 200Hz. Oscillations in the peak frequency were observed with an amplitude of 1kHz and a period of approximately 1000s, which may be related to changes in power after the fiber or in the polarization of the EOM. If the former is the cause of the oscillations, power stabilization of the laser can be implemented if the power of the reflected light is measured and an acousto-optic modulator used. If the cause is the latter, the temperature of the EOM can be stabilized. Furthermore, a drift was observed with a rate which has a signal that depends on the room temperature and which has a magnitude that depends on the cavity's temperature, which suggests that the lock parameters of the temperature controller should be optimized. The 1kHz-amplitude oscillations are within the required width of 313kHz of the two-photon detuning to get high transfer efficiencies. The present drift requires that every couple of hours the zero two-photon detuning and the intermediate level have to be found again. The lock between the two lasers with the same frequency still has to be implemented.

To integrate this setup in the polar molecules experiment, acousto-optic modulators will be placed before the optical fibers that will send the m=1 diffracted light beam into the experiment. In this way, the appropriate time sequence can transfer efficiently the molecules into the rovibrational ground state, without ever populating lossy intermediate states.

Bibliography

[1] A. Ashkin. *Acceleration and trapping of particles by radiation pressure*. Physical review letters **24**, 156–159 (1970). (Cited on page 1.)

[2] P. Metcalf, H. J., van der Straten. *Laser Cooling and Trapping*. Springer-Verlag, New York (1999). (Cited on page 1.)

[3] M. H. Anderson, J. R. Ensher, M. R. Matthews, C. E. Wieman, and E. a. Cornell. *Observation of bose-einstein condensation in a dilute atomic vapor.* Science (New York, N.Y.) **269**, 198–201 (1995). (Cited on page 1.)

[4] K. Davis, M. Mewes, and M. Andrews. *Bose-Einstein condensation in a gas of sodium atoms*. Physical Review Letters **75** (1995). (Cited on page 1.)

[5] A. Einstein. *Quantentheorie des einatomigen idealen Gases*. Sitzungsberichte der Preussischen Akademie der Wissenschaften **1**, 3–10 (1925). (Cited on page 1.)

[6] S. Bose. *Plancks Gesetz und Lichtquantenhypothese*. Z. phys pages 178–181 (1924). (Cited on page 1.)

[7] M. R. Andrews. *Observation of Interference Between Two Bose Condensates*. Science **275**, 637–641 (1997). (Cited on page 1.)

[8] M.-O. Mewes, M. R. Andrews, D. M. Kurn, D. S. Durfee, C. G. Townsend, and W. Ketterle. *Output Coupler for Bose-Einstein Condensed Atoms*. Physical Review Letters **78**, 582–585 (1997). (Cited on page 1.)

[9] B. DeMarco. *Onset of Fermi Degeneracy in a Trapped Atomic Gas*. Science **285**, 1703–1706 (1999). (Cited on page 1.)

[10] I. Bloch, T. Hansch, and T. Esslinger. *Measurement of the spatial coherence of a trapped Bose gas at the phase transition*. Nature **403**, 166–70 (2000). (Cited on page 1.)

[11] M. Matthews, B. Anderson, P. Haljan, D. Hall, C. Wieman, and E. Cornell. *Vortices in a Bose-Einstein Condensate*. Physical Review Letters **83**, 2498–2501 (1999). (Cited on page 1.)

[12] S. Jochim, M. Bartenstein, a. Altmeyer, G. Hendl, S. Riedl, C. Chin, J. Hecker Denschlag, and R. Grimm. *Bose-Einstein condensation of molecules.* Science (New York, N.Y.) **302**, 2101–3 (2003). (Cited on page 1.)

[13] M. Greiner, C. a. Regal, and D. S. Jin. *Emergence of a molecular Bose-Einstein condensate from a Fermi gas.* Nature **426**, 537–40 (2003). (Cited on page 1.)

[14] M. Zwierlein, C. Stan, C. Schunck, S. Raupach, S. Gupta, Z. Hadzibabic, and W. Ketterle. *Observation of Bose-Einstein Condensation of Molecules*. Physical Review Letters **91**, 250401 (2003). (Cited on page 1.)

[15] C. A. Regal, M. Greiner, and D. S. Jin. *Observation of Resonance Condensation of Fermionic Atom Pairs*. Physical Review Letters **92**, 040403 (2004). (Cited on page 1.)

[16] M. W. Zwierlein, J. R. Abo-Shaeer, a. Schirotzek, C. H. Schunck, and W. Ketterle. *Vortices and superfluidity in a strongly interacting Fermi gas.* Nature **435**, 1047–51 (2005). (Cited on page 1.)

[17] J. Hubbard. *Electron correlations in narrow energy bands*. Proceedings of the Royal Society of . . . **276**, 238–257 (1963). (Cited on page 2.)

[18] M. P. A. Fisher, P. B. Weichman, J. Watson, and D. S. Fisher. *Boson localization and the superfluid-insulator transition*. Physical Review B **40** (1989). (Cited on page 2.)

[19] D. Jaksch, C. Bruder, J. Cirac, C. Gardiner, and P. Zoller. *Cold Bosonic Atoms in Optical Lattices*. Physical Review Letters **81**, 3108–3111 (1998). (Cited on page 2.)

[20] M. Greiner, O. Mandel, T. Esslinger, T. Hänsch, and I. Bloch. *Quantum phase transition from a superfluid to a Mott insulator in a gas of ultracold atoms*. Nature pages 39–44 (2002). (Cited on page 2.)

[21] M. Takamoto, F.-L. Hong, R. Higashi, and H. Katori. *An optical lattice clock.* Nature **435**, 321–4 (2005). (Cited on page 2.)

[22] T. Lahaye, C. Menotti, L. Santos, M. Lewenstein, and T. Pfau. *The physics of dipolar bosonic quantum gases*. Reports on Progress in Physics **72**, 126401 (2009). (Cited on page 3.)

[23] D. DeMille. *Quantum Computation with Trapped Polar Molecules*. Physical Review Letters **88**, 067901 (2002). (Cited on page 3.)

[24] K. Góral, L. Santos, and M. Lewenstein. *Quantum Phases of Dipolar Bosons in Optical Lattices*. Physical Review Letters **88**, 170406 (2002). (Cited on page 3.)

[25] A. Micheli, G. K. Brennen, and P. Zoller. *A toolbox for lattice-spin models with polar molecules*. Nature Physics **2**, 341–347 (2006). (Cited on page 3.)

[26] H. P. Büchler, E. Demler, M. Lukin, a. Micheli, N. ProkofâĂŹev, G. Pupillo, and P. Zoller. *Strongly Correlated 2D Quantum Phases with Cold Polar Molecules: Controlling the Shape of the Interaction Potential*. Physical Review Letters **98**, 060404 (2007). (Cited on page 3.)

[27] G. Pupillo, a. Griessner, a. Micheli, M. Ortner, D.-W. Wang, and P. Zoller. *Cold Atoms and Molecules in Self-Assembled Dipolar Lattices*. Physical Review Letters **100**, 050402 (2008). (Cited on page 3.)

[28] B. Capogrosso-Sansone, C. Trefzger, M. Lewenstein, P. Zoller, and G. Pupillo. *Quantum Phases of Cold Polar Molecules in 2D Optical Lattices*. Physical Review Letters **104**, 125301 (2010). (Cited on page 3.)

[29] E. S. Shuman, J. F. Barry, and D. Demille. *Laser cooling of a diatomic molecule.* Nature **467**, 820–3 (2010). (Cited on page 3.)

[30] M. T. Hummon, M. Yeo, B. K. Stuhl, A. L. Collopy, Y. Xia, and J. Ye. *2D Magneto-Optical Trapping of Diatomic Molecules*. Physical Review Letters **110**, 143001 (2013). (Cited on page 3.)

[31] M. S. Elioff, J. J. Valentini, and D. W. Chandler. *Subkelvin cooling NO molecules via "billiard-like" collisions with argon.* Science (New York, N.Y.) **302**, 1940–3 (2003). (Cited on page 3.)

[32] H. Bethlem, G. Berden, and G. Meijer. *Decelerating Neutral Dipolar Molecules*. Physical Review Letters **83**, 1558–1561 (1999). (Cited on page 3.)

[33] M. Zeppenfeld, M. Motsch, P. Pinkse, and G. Rempe. *Optoelectrical cooling of polar molecules*. Physical Review A **80**, 041401 (2009). (Cited on page 3.)

[34] L. D. Carr, D. DeMille, R. V. Krems, and J. Ye. *Cold and ultracold molecules: science, technology and applications*. New Journal of Physics **11**, 055049 (2009). (Cited on page 4.)

[35] H. Thorsheim, J. Weiner, and P. Julienne. *Laser-Induced Photoassociation of Ultracold Sodium Atoms*. Physical review letters **58**, 2420–2423 (1987). (Cited on page 4.)

[36] A. Fioretti, D. Comparat, and A. Crubellier. *Formation of Cold Cs_2 Molecules through Photoassociation*. Physical Review Letters **80**, 4402–4405 (1998). (Cited on page 4.)

[37] R. Wynar. *Molecules in a Bose-Einstein Condensate*. Science **287**, 1016–1019 (2000). (Cited on page 4.)

[38] S. Inouye, M. Andrews, and J. Stenger. *Observation of Feshbach resonances in a Bose-Einstein condensate*. Nature pages 8–11 (1998). (Cited on page 4.)

[39] F. H. Mies, E. Tiesinga, and P. S. Julienne. *Manipulation of Feshbach resonances in ultracold atomic collisions using time-dependent magnetic fields*. Physical Review A **61**, 022721 (2000). (Cited on page 4.)

[40] C. Regal, C. Ticknor, J. Bohn, and D. Jin. *Creation of ultracold molecules from a Fermi gas of atoms*. Nature pages 47–50 (2003). (Cited on page 4.)

[41] K. Bergmann, H. Theuer, and B. Shore. *Coherent population transfer among quantum states of atoms and molecules*. Reviews of Modern Physics **70**, 1003–1025 (1998). (Cited on pages 5, 20, and 21.)

[42] K.-K. Ni, S. Ospelkaus, M. H. G. de Miranda, A. Pe'er, B. Neyenhuis, J. J. Zirbel, S. Kotochigova, P. S. Julienne, D. S. Jin, and J. Ye. *A high phase-space-density gas of polar molecules.* Science (New York, N.Y.) **322**, 231–5 (2008). (Cited on pages 5 and 20.)

[43] M. Aymar and O. Dulieu. *Calculation of accurate permanent dipole moments of the lowest 1,3Sigma+ states of heteronuclear alkali dimers using extended basis sets.* The Journal of chemical physics **122**, 204302 (2005). (Cited on page 5.)

[44] P. S. Zuchowski and J. M. Hutson. *Reactions of ultracold alkali-metal dimers*. Physical Review A **81**, 060703 (2010). (Cited on page 5.)

[45] M. Born and R. Oppenheimer. *Zur Quantentheorie der Molekeln*. Annalen der Physik **389**, 457–484 (1927). (Cited on page 8.)

[46] G. Herzberg. *Molecular spectra and molecular structure. Vol. 1: Spectra of diatomic molecules*. New York: Van Nostrand Reinhold, 1950, 2nd ed. (1950). (Cited on pages 14 and 15.)

[47] E. Condon. *Nuclear motions associated with electron transitions in diatomic molecules*. Physical Review **3** (1928). (Cited on page 15.)

[48] T. Köhler, K. Góral, and P. Julienne. *Production of cold molecules via magnetically tunable Feshbach resonances*. Reviews of Modern Physics **78**, 1311–1361 (2006). (Cited on page 17.)

[49] C. Chin, R. Grimm, P. Julienne, and E. Tiesinga. *Feshbach resonances in ultracold gases*. Reviews of Modern Physics **82**, 1225–1286 (2010). (Cited on page 17.)

[50] R. Ferlaino, F., Knoop, S., Grimm. *Ultracold Feshbach molecules*. In R. Krems, B. Friedrich, and W. Stwalley, editors, *Cold Molecules: Theory, Experiment, Applications*, chapter Ultracold. CRC Press, Boca Raton (2009). (Cited on page 17.)

[51] K. Huang. *Statistical mechanics*. John Wiley & Sons, 2nd edition (1987). (Cited on page 17.)

[52] E. Hodby, S. Thompson, C. Regal, M. Greiner, a. Wilson, D. Jin, E. Cornell, and C. Wieman. *Production Efficiency of Ultracold Feshbach Molecules in Bosonic and Fermionic Systems*. Physical Review Letters **94**, 120402 (2005). (Cited on page 19.)

[53] U. Gaubatz, P. Rudecki, M. Becker, S. Schiemann, M. Külz, and K. Bergmann. *Population switching between vibrational levels in molecular beams*. Chemical physics . . . **149**, 463–468 (1988). (Cited on page 20.)

[54] U. Gaubatz, P. Rudecki, S. Schiemann, and K. Bergmann. *Population transfer between molecular vibrational levels by stimulated Raman scattering with partially overlapping laser fields. A new concept and experimental results*. The Journal of Chemical Physics **92**, 5363 (1990). (Cited on page 24.)

[55] N. V. Vitanov and S. Stenholm. *Properties of stimulated Raman with intermediate level adiabatic detuning passage*. Optics communications **135**, 394–405 (1997). (Cited on page 24.)

[56] V. Romanenko and L. Yatsenko. *Adiabatic population transfer in the three-level Λ-system: two-photon lineshape*. Optics communications **140**, 231–236 (1997). (Cited on pages 24 and 25.)

[57] M. Danileiko, V. Romanenko, and L. Yatsenko. *Landau-Zener transitions and population transfer in a three-level system driven by two delayed laser pulses*. Optics communications **109**, 462–466 (1994). (Cited on page 25.)

[58] N. V. Vitanov, T. Halfmann, B. W. Shore, and K. Bergmann. *Laser-induced population transfer by adiabatic passage techniques.* Annual review of physical chemistry **52**, 763–809 (2001). (Cited on page 25.)

[59] N. Vitanov and S. Stenholm. *Population transfer via a decaying state*. Physical Review A **56**, 1463–1471 (1997). (Cited on page 25.)

[60] N. Vitanov and S. Stenholm. *Adiabatic population transfer via multiple intermediate states*. Physical Review A **60**, 3820–3832 (1999). (Cited on pages 26, 28, and 29.)

[61] L. Yatsenko, V. Romanenko, B. Shore, and K. Bergmann. *Stimulated Raman adiabatic passage with partially coherent laser fields*. Physical Review A **65**, 043409 (2002). (Cited on pages 29 and 30.)

[62] C.-H. Wu, J. W. Park, P. Ahmadi, S. Will, and M. W. Zwierlein. *Ultracold Fermionic Feshbach Molecules of $^{23}Na^{40}K$*. Physical Review Letters **109**, 085301 (2012). (Cited on page 31.)

[63] A. Gerdes, M. Hobein, H. Knöckel, and E. Tiemann. *Ground state potentials of the NaK molecule*. The European Physical Journal D **49**, 67–73 (2008). (Cited on page 31.)

[64] M. Aymar and O. Dulieu. *Calculations of transition and permanent dipole moments of heteronuclear alkali dimers NaK, NaRb and NaCs*. Molecular Physics **105**, 1733–1742 (2007). (Cited on page 31.)

[65] R. Fox, C. Oates, and L. Hollberg. *Stabilizing diode lasers to high-finesse cavities*. Experimental methods in the physical sciences **40**, 1–46 (2003). (Cited on page 36.)

[66] M. Fleming and A. Mooradian. *Spectral Characteristics of External-Cavity Controlled Semiconductor Lasers*. Quantum Electronics, IEEE Journal ... **17**, 44–59 (1981). (Cited on page 37.)

[67] B. E. A. Saleh and M. C. Teich. *Fundamentals of Photonics*. John Wiley & Sons, Hoboken, New Jersey, 2nd edition (2007). (Cited on page 37.)

[68] L. Ricci, M. Weidemüller, T. Esslinger, A. Hemmerich, C. Zimmermann, V. Vuletic, W. König, and T. W. Hänsch. *A compact grating-stabilized diode laser system for atomic physics*. Optics communications **117**, 541–549 (1995). (Cited on page 38.)

[69] K. Numata, A. Kemery, and J. Camp. *Thermal-Noise Limit in the Frequency Stabilization of Lasers with Rigid Cavities*. Physical Review Letters **93**, 250602 (2004). (Cited on page 39.)

[70] J. Millo, D. Magalhães, C. Mandache, Y. Le Coq, E. English, P. Westergaard, J. Lodewyck, S. Bize, P. Lemonde, and G. Santarelli. *Ultrastable lasers based on vibration insensitive cavities*. Physical Review A **79**, 053829 (2009). (Cited on page 39.)

[71] T. Legero, T. Kessler, and U. Sterr. *Tuning the thermal expansion properties of optical reference cavities with fused silica mirrors*. Journal of the Optical Society of America B **27**, 914 (2010). (Cited on page 39.)

[72] D. R. Leibrandt, M. J. Thorpe, M. Notcutt, R. E. Drullinger, T. Rosenband, and J. C. Bergquist. *Spherical reference cavities for frequency stabilization of lasers in non-laboratory environments.* Optics express **19**, 3471–82 (2011). (Cited on page 40.)

[73] A. E. Siegman. *Lasers*. University Science Books, Mill Valley, California, 1st edition (1986). (Cited on pages 41 and 87.)

[74] J. Hall, M. S. Taubman, and J. Ye. *Laser Stabilization*. In M. Bass, J. M. Enoch, E. W. V. Stryland, and W. L. Wolfe, editors, *Handbook of Optics: Fiber Optics and Nonlinear Optics*, volume 4, chapter 27, pages 1–34. McGraw-Hill, New York (2001). (Cited on page 44.)

[75] R. W. P. Drever, J. L. Hall, F. V. Kowalski, J. Hough, G. M. Ford, a. J. Munley, and H. Ward. *Laser phase and frequency stabilization using an optical resonator*. Applied Physics B Photophysics and Laser Chemistry **31**, 97–105 (1983). (Cited on page 45.)

[76] E. D. Black. *An introduction to Pound-Drever-Hall laser frequency stabilization*. American Journal of Physics **69**, 79 (2001). (Cited on pages 45 and 49.)

[77] W. Nagourney. *Quantum electronics for atomic physics*. Oxford University Press, 1st edition (2010). (Cited on page 49.)

[78] T. Day, E. Gustafson, and R. Byer. *Sub-hertz relative frequency stabilization of two-diode laser-pumped Nd: YAG lasers locked to a Fabry-Perot interferometer*. Quantum Electronics, IEEE ... **28**, 1106–1117 (1992). (Cited on page 50.)

[79] G. Rempe, R. J. Thompson, H. J. Kimble, and R. Lalezari. *Measurement of ultralow losses in an optical interferometer.* Optics letters **17**, 363–5 (1992). (Cited on page 68.)

[80] K. An, C. Yang, R. R. Dasari, and M. S. Feld. *Cavity ring-down technique and its application to the measurement of ultraslow velocities.* Optics letters **20**, 1068 (1995). (Cited on page 68.)

Electro-optic modulator

Some crystals have the property of changing their index of refraction proportionally to the amplitude of an external electric field to them applied - this is called electro-optic effect. Assuming an x-polarized light, the variation of the refractive index is given by [73]: $\Delta n_x = \frac{n_{0x}^3 rE}{2}$, where n_{0x} is the unperturbed refraction index in the x direction and r is the electro-optic coefficient. In this experiment, the crystals chosen for the EOM's were lithium niobate ($LiNbO_3$) since they have a high electro-optic coefficient.

The change in the index of refraction leads to a change of the optical path, and therefore of the phase of the light that goes through the crystal. In the transversal electro-optic modulator (figure 1), a pair of parallel electrodes on the top and bottom of the crystal, separated by a distance d between which the voltage is V, creates an electric field with an amplitude given by $E = V/\epsilon_r d$ where ϵ_r is the dielectric constant of the crystal. This causes a refractive index change along the polarization direction, which is chosen to be parallel to the field, since for this case the refractive index change is larger. The change in phase that the light experiences is given by the following expression: $\Delta_\phi = \frac{\pi n_0^3 rVL}{\lambda \epsilon_r d}$.

This EOM can be modulated like a capacitor. For a sinusoidal voltage $V = V_m \sin(\alpha t)$, the phase varies as $\phi = \frac{2\pi}{\lambda}\left[n_0 - \frac{n_0^3 r V_m d \sin(\alpha t)}{2}\right] L$. Which results in an output electric field given by

$$E = E_0 \left[J_0(\frac{n^3 r E_m}{2}) e^{i\omega t} + J_1(\frac{n^3 r E_m}{2}) e^{i(\omega+\alpha)t} - J_1(\frac{n^3 r E_m}{2}) e^{i(\omega-\alpha)t} \right] \quad (1)$$

when applied the Jacobi-Anger expansion and truncated in the first order.

As the electro-optic coefficients are small, high electric fields are required for the phase shift to be significative. As in our case, the modulation is supposed to be at a particular fixed frequency, a resonant circuit was built. The EOM crystal together with the electrodes form a capacitor, which in series with

an inductor (coil) with low losses form a LC resonant circuit. This allows the existence of a large electric field between then electrodes with a small applied voltage, since the energy is stored in the circuit by going back and forth from the capacitor to the inductor, only having some resistance due to the losses of the circuit (especially of the inductor). The SMA connector used to establish the driving voltage was impedance matched to the circuit (which maximizes the transfer of power to the circuit) with the help of a network analyzer (E5061B, *Agilent*) by looking at the reflected divided by the injected signal amplitude as a function of the modulation frequency. In practice, we changed the position of where the wire coming from the SMA connector was touching the coil, until a dip in the reflected amplitude was observed in the network analyzer at a particular frequency (the resonant frequency of the circuit). At this point the match-impedance is achieved, which means that most of the power sent into the circuit is there dissipated.

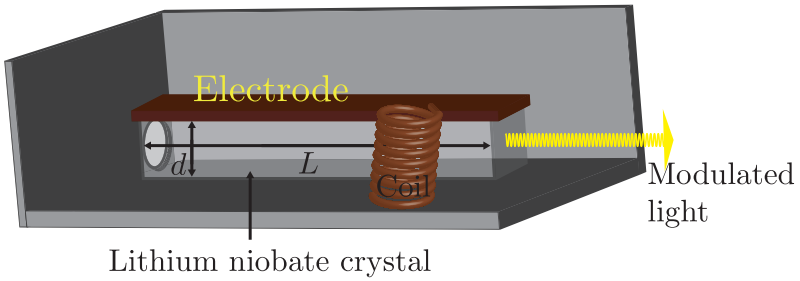

Figure 1: Scheme of a transversal electro-optic modulator, similar to the ones used in the experiment. The light enters the box through a hole and travels through the crystal with a length L in which there is en electric field perpendicular to the direction of propagation caused by a voltage difference between the electrodes that are on top and bottom of the crystal separated by d (the bottom electrode is in this case the box where this crystal is in). A coil is connected in series with the electrodes, constituting a resonant circuit. The SMA connector (not represented), through which the voltage signal is applied to the circuit, is soldered to a point in the coil while impedance matching ($Z_{circuit} = Z^*_{source}$) is assured.

The resonant frequencies (f_r) of the EOM's built are 71,3MHz for the blue light and 89,7MHz for the red one, with resonant lines that have full-width-half-maximum values (Δf) of 0,8MHz and 1,3MHz, respectively (read through the network analyzer). The quality factor ($Q = 2\pi \frac{\text{Energy stored}}{\text{Energy dissipated in one cycle}}$), which for high values of Q has the following expression: $Q = \frac{f_r}{\Delta f}$, is 89 for the $f_r = 71,3$MHz and 69 for $f_r = 89,7$MHz.

Acknowledgements

I would like to express my gratitude to all those who helped me through the moments of hard work, sometimes by sharing moments of relaxation, and without whom the completion of this master thesis would not be possible. Especially I would like to thank:

- Prof. Dr. Immanuel Bloch for giving me the possibility to work in a group with so many interesting people, and in which it is possible to learn even during lunch or in a beer garden;
- Dr. Christoph Gohle for everything he taught me and for having had the patience and the talent to explain me the concepts in several different ways until I fully understood them;
- the polar molecules team: Nikolaus Buchheim, Christoph Gohle, Zhenkai Lu, Tobias Schneider and Yannick Seis for all their help and for the enjoyable and relaxed atmosphere;
- the non-polar teams' members: Dr. Takeshi Fukuhara, Dr. Christian Groß, Martin Boll, Sebastian Hild, Timon Hilker, Alexander Keesling, Ahmed Omran, Thomas Reimann, Peter Schauß, Konrad Viebahn and Johannes Zeiher for the interesting and sometimes passionate conversations and for the time spent with some in the basement making sure it was clean;
- Marianne Kargl for her help with bureaucracy, Anton Mayer for teaching me, among other things, how to use properly a drilling machine; Karsten Förster and Oliver Mödl for their help in electronics;
- all my teachers and Professors who, throughout the years, taught me how to use and develop my competences;
- my friends which, either they were in Munich, Portugal or some other place in the world, never stopped cheering me up and meeting me when that was possible;
- Michael Lohse for spending time having coffee with me;
- my family, particularly my parents that have always supported me and had to adapt from my weekly visits to quarterly ones.